AFGL-TR-80-022{

LEVEL II

⑫

ERROR MODELS FOR GRAVITY GRADIOMETERS IN AIRBORNE SURVEYS

James V. White

The Analytic Sciences Corporation
One Jacob Way
Reading, Massachusetts 01867

Scientific Report No. 3

January 1980

DTIC
ELE
APR 1 5 1981

A

Approved for public release; distribution unlimited

Prepared For:
AIR FORCE GEOPHYSICS LABORATORY
AIR FORCE SYSTEMS COMMAND
United States Air Force
Hanscom AFB, Massachusetts 01731

81 4 14 .30

REPORT DOCUMENTATION PAGE	READ INSTRUCTIONS BEFORE COMPLETING FORM

1. REPORT NUMBER	2. GOVT ACCESSION NO.	3. RECIPIENT'S CATALOG NUMBER
AFGL-TR-80-0220	AD-A097745	

4. TITLE *(and Subtitle)*	5. TYPE OF REPORT & PERIOD COVERED
ERROR MODELS FOR GRAVITY GRADIOMETERS IN AIRBORNE SURVEYS	Scientific Report No. 3
	6. PERFORMING ORG. REPORT NUMBER

7. AUTHOR(s)	8. CONTRACT OR GRANT NUMBER(s)
James V. White	F19628-77-C-0152

9. PERFORMING ORGANIZATION NAME AND ADDRESS	10. PROGRAM ELEMENT, PROJECT, TASK AREA & WORK UNIT NUMBERS
The Analytic Sciences Corporation One Jacob Way Reading, Massachusetts 01867	320432AA 32

11. CONTROLLING OFFICE NAME AND ADDRESS	12. REPORT DATE
Air Force Geophysics Laboratory Hanscom AFB, Massachusetts 01731 Monitor/LT.Col.Norman H. Mason/LWG	Jan 80
	13. NUMBER OF PAGES
	167

14. MONITORING AGENCY NAME & ADDRESS *(if different from Controlling Office)*	15. SECURITY CLASS. *(of this report)*
SCIENTIFIC - 3	Unclassified
	15a. DECLASSIFICATION/DOWNGRADING SCHEDULE

16. DISTRIBUTION STATEMENT *(of this Report)*

Approved for public release; distribution unlimited.

17. DISTRIBUTION STATEMENT *(of the abstract entered in Block 20, if different from Report)*

This research was sponsored by the Defense Mapping Agency, (DMA), Washington, D.C.

18. SUPPLEMENTARY NOTES

19. KEY WORDS *(Continue on reverse side if necessary and identify by block number)*

Gravity, Gravity Gradiometer, Gravity Survey, Error Model, Self Noise, Vibration, Sensitivity

20. ABSTRACT *(Continue on reverse side if necessary and identify by block number)*

This report describes error models for gravity gradiometers in survey applications. The major emphasis is on the baseline Gravity Gradiometer Instrument No. 1 developed by the Bell Aerospace Division of Textron, Inc., for which comprehensive test data were available. Preliminary results are included for Bell's Ball-Bearing Gradiometer and the Floated Gradiometer Instrument developed by the Charles Stark Draper Laboratory.

DD , FORM, 1473 EDITION OF 1 NOV 65 IS OBSOLETE

1

20. ABSTRACT (Cont.)

Models for the vibration environment of an airborne gradiometer system are also described; these are based on extrapolations of available aircraft flight test data. The report concludes with examples of gradiometric survey simulations based on these error models.

FOREWORD

This report describes error models for gravity gradiometers in survey applications. The major emphasis is on the baseline Gravity Gradiometer Instrument No. 1 developed by the Bell Aerospace Division of Textron, Inc., for which comprehensive test data were available. Preliminary results are included for Bell's Ball-Bearing Gradiometer and the Floated Gradiometer Instrument developed by the Charles Stark Draper Laboratory.

Models for the vibration environment of an airborne gradiometer system are also described; these are based on extrapolations of available aircraft flight test data. The report concludes with examples of gradiometric survey simulations based on these error models.

TABLE OF CONTENTS

TABLE OF CONTENTS (Continued)

LIST OF FIGURES

LIST OF FIGURES (Continued)

8

LIST OF TABLES

1. INTRODUCTION

1.1 AIRBORNE GRADIOMETRIC GRAVITY SURVEYS

The potential future use of gravity gradiometers in airborne surveys, as presented in Fig. 1.1-1, may significantly augment present-day survey techniques. Two key advantages to be gained by using airborne gradiometers are

- More accurate measurements of the short-wavelength features in the earth's gravity field

- Denser surveys for areas where conventional survey methods are relatively slow and costly.

R—51324
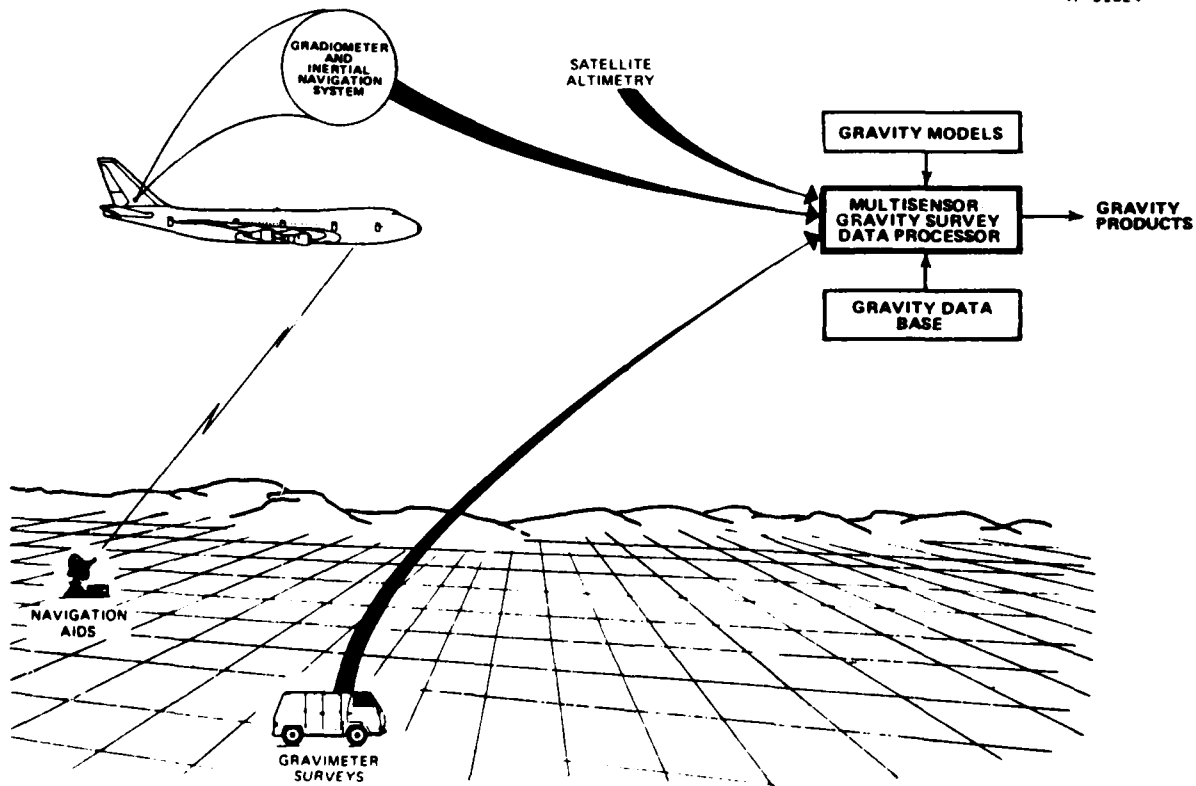
Figure 1.1-1   Airborne Gradiometric Gravity Survey

11

Gradiometric data, when combined with long-wavelength data obtained from other sources such as satellite altimetry and satellite tracking, can potentially provide more accurate estimates of gravity over larger areas than is practical with current survey methods. This report describes error models for gravity gradiometers, which in combination with the TASC Multisensor Survey Simulation software, provide estimates of survey accuracy improvements to be expected with the inclusion of airborne gradiometry.

1.2   MAJOR GRADIOMETER ERROR SOURCES

Gradient measurement errors are caused by

- Self noise originating inside the gradiometer

- Environmental disturbances to which the gradiometer is sensitive

- Systematic errors.

The self noise depends only on the gradiometer and sets a fundamental limit on the ultimate accuracy of its measurements, independently of the operating environment. In contrast, the errors due to environmental disturbances depend on both the gradiometer and the severity of the thermal, magnetic, mechanical, and gravitational disturbances acting on it.

There are standard methods for isolating the gradiometer from environmental disturbances during moving-base operations. Control of the thermal environment requires the use of thermal barriers and temperature control systems. Magnetic shields are built into the gradiometer to attentuate both external magnetic fields and those induced by current-carrying elements in the gradiometer itself. The gradiometer

12

can be partially isolated from linear and angular mechanical vibrations by the combined use of a passive vibration isolation system and an inertial platform.

The gradiometer is also naturally susceptible to the time-varying gravity gradient fields caused by relative motions of nearby masses such as gimbals in the inertial platform. Corrections can be applied to the gradiometer output signals to compensate for the gradient fields caused by disturbing masses whose positions can be monitored.

1.3   AVAILABLE TEST DATA

Prototype gravity gradiometers have been developed for moving-base applications at both the Charles Stark Draper Laboratory (Draper) and the Bell Aerospace Division of Textron, Inc. (Bell). The comprehensive body of formal test data on Bell's baseline Gravity Gradiometer Instrument (GGI No. 1) was the primary data base used for developing the error models described in this report. These data were supplemented by recently available data on a modified version of the Bell instrument known as the Ball-Bearing GGI. Recent data for the Draper gradiometer were also analyzed. Error models for the Draper gradiometer have not been as fully developed as those for the Bell instrument, but preliminary results are related to survey performance.

Bell is currently building and testing smaller versions of their baseline gradiometer that employ ball bearings for the rotating assembly. The design of the ball-bearing gradiometers is similar to the baseline GGI, and the error models described in this report are therefore applicable to these newer instruments. Only preliminary test data on the

ball-bearing prototype are currently available. Error model refinements associated with additional test data from the new instruments are likely to consist of parameter adjustments.

The dominant instrument errors during an airborne survey are expected to be caused by the self noise and the mechanical vibration environment of the gradiometer. Ample test data on the Bell GGI No. 1 were available for modeling these error sources (Refs. 1-11). Temperature sensitivity data (Refs. 3, 11, 12) indicated that thermally-induced errors should be small enough to ignore compared to other types of errors under survey conditions. This conclusion is based on Bell's measured thermal sensitivity coefficients, which are less than, or equal to, 49 eötvös per degree celsius change in the temperature of the gradiometer's instrument block.

1.4   ERROR MODELS FOR SURVEY SIMULATIONS

The accuracy with which gravimetric quantities, such as anomalies and vertical deflections, can be recovered from gradiometric survey data depends on the characteristics of the gravity field, the geometry of the survey, the data available from other sensors, and the errors in the gradiometer measurements. The TASC Multisensor Survey Simulation software uses models for the gravity fields, survey geometries, and available sensors to estimate the rms errors inherent in a statistically optimal recovery of gravity products through multidimensional Wiener filtering. These calculations are carried out in the frequency domain. Therefore, the gradiometer error models described in this report are represented by power spectral densities. These densities provide an easily understandable characterization of the random errors due to gradiometer self noise and aircraft vibrations.

14

1.5   OVERVIEW OF REPORT

Models for the self noise of the Bell and Draper gradi-
ometers are described in Chapter 2; these models were derived
from test data by using two different methods of spectral esti-
mation.   Chapter 3 describes models for vibration-induced errors
in the Bell baseline instrument.   Also in Chapter 3, models
for the vibration environment of an airborne gradiometer are
developed from aircraft flight test data. This chapter ends
with an error model for a complete survey system consisting of
three gradiometer instruments mounted on one inertial plat-
form.   Examples of gradiometer survey simulation results ob-
tained with the survey-system error model are described in
Chapter 4.   Chapter 5 describes the status of ongoing gradi-
ometer development and discusses key issues for future air-
borne gradiometer test plans.   The report ends with conclu-
sions and recommendations in Chapter 6.

2.   GRADIOMETER SELF NOISE

2.1   INTRODUCTION

This chapter describes techniques for deriving gradi-
ometer self-noise models from test data. The analysis of data
for the Bell baseline Gravity Gradiometer Instrument (GGI) is
described in detail. Recently obtained self-noise spectra for
the Bell ball-bearing and Draper floated gradiometers are also
presented.

A series of experiments (Refs. 1, 3, 4, 10, 11) were
performed at Bell to measure the self noise of their baseline
GGI. These were conducted in accordance with the test procedure
TP1 (Ref. 4). The data sets discussed in this report were
obtained in two experiments: one with the gradiometer spin
axis vertical (SAV) and the other with the spin axis hori-
zontal (SAH). These experiments spanned 13 days for the SAH
orientation and almost 11 days for SAV. An overview of these
data is shown in Figs. 2.1-1 and 2.1-2. Each figure shows
both the inline and cross-channel outputs[*] of the GGI as a
function of time. The time histories in Fig. 2.1-2 clearly
show start-up transients, while the plots in Fig. 2.1-1 are
free of start-up transients because the GGI had been running
several days before these data were taken.

---

[*]This terminology reflects the fact that the Bell gradiometer
simultaneously measures "inline" and "cross" elements of the
gravity gradient tensor. A description of these measurements
is given in Appendix B.

16
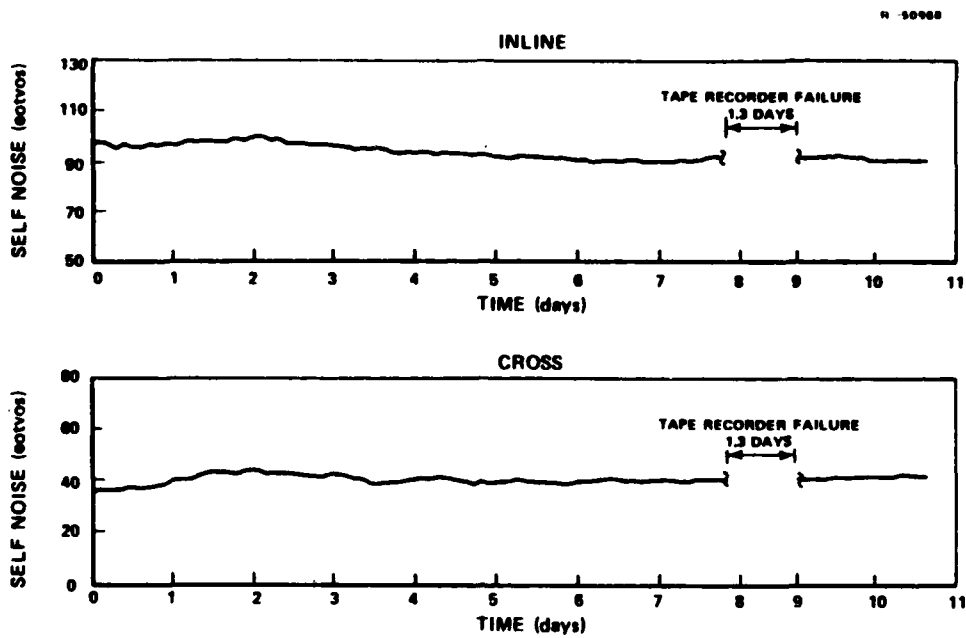
Figure 2.1-1   Bell GGI No. 1 Self-Noise Data
(SAV, April Data, Ref. 24)
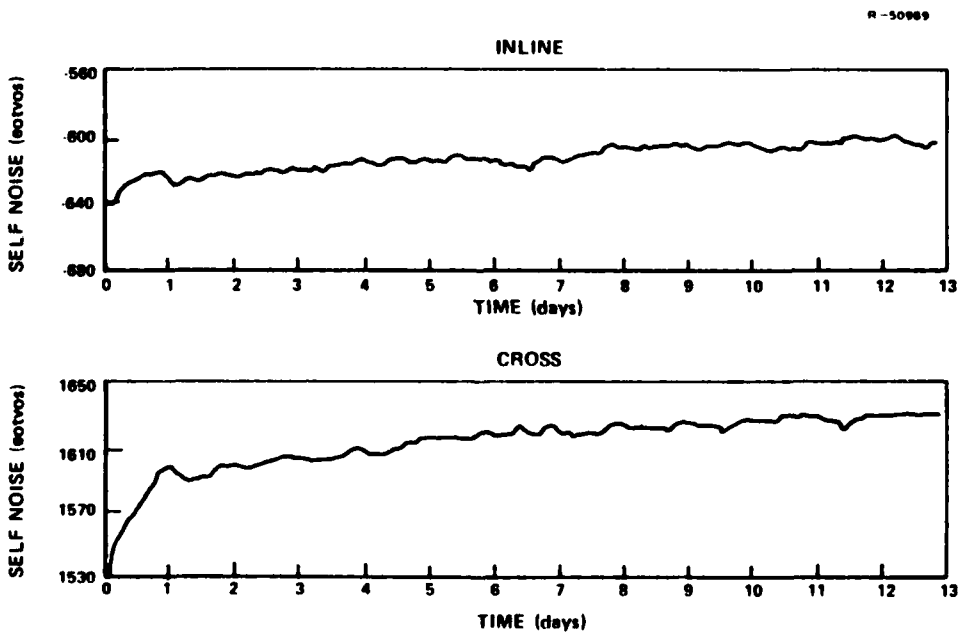
Figure 2.1-2   Bell GGI No. 1 Self-Noise Data
(SAH, March Data, Ref. 11)

17

2.2   PREPROCESSING OF DATA

The gradiometer noise data were analyzed in three
stages. The first stage, termed preprocessing, is described
in this section. The laboratory data are sample values of the
outputs of the cross and inline channels of the gradiometer.
The sampling rate for each channel was 0.5 samples per second,
and the data were scaled to read directly in eötvös (E). The
self noise consisted of small fluctuations about relatively
large mean values once the initial start-up transients died
out. These mean values were arbitrary offsets and were there-
fore subtracted from the data before the power spectral den-
sities of the noise were estimated. This removal of the means
reduced low-frequency bias in the spectral estimates.

To facilitate low-frequency analysis, the data were
lowpass filtered and resampled at 1/64 the original sampling
rate. This "decimation" was implemented in two steps with a
finite-impulse-response (FIR) digital filter. The first step
was to filter contiguous blocks of laboratory data. Each of
these blocks contained 8192 sample pairs (cross and inline
data), which at the output of the FIR filter produced 1024
sample pairs with a sampling rate of 0.0625 samples per sec-
ond. The second step was to form contiguous blocks from these
filtered samples and pass them again through the FIR filter to
produce samples having the final desired rate. In this way
seven blocks of decimated data, each containing 1024 sample
pairs, were generated for the SAH orientation, and five blocks
were obtained for SAV. The FIR filter was designed by using a
Kaiser windowing technique, and the proper operation of the
filter was verified through the use of sinusoidal test signals.

The two data tapes were dated March 9 and April 25,
1978. Plots of these data were previously shown in Figs. 2.1-1

and 2.1-2. During the preprocessing of the April 25 data, the
gap due to tape recorder failure was avoided since it would
otherwise have introduced bias into the spectral estimates.
The first day of data in the March 9 tape was also avoided
because of the start-up transient.

2.3   SPECTRAL ESTIMATION METHODS EMPLOYED

The analysis of the gradiometer noise data was con-
ducted so as to balance the conflicting goals of obtaining
spectral estimates that were both precise and unbiased. There
was also the need to verify that the data were consistent with
a stationary random model for the self noise. Without evidence
of stationarity the entire procedure of modeling the self noise
with a power spectrum could be misleading.

The preprocessed data were analyzed in blocks con-
taining 1024 sample pairs (inline and cross-channel data).
These blocks, in the case of decimated data, each spanned about
1.5 days, which was long enough to provide spectral estimates
down to the lowest frequencies of interest in gravity survey
simulations. On the other hand, the blocks were short enough
to test for nonstationary behavior over the durations of the
data sets. The block length also provided spectral estimates
from the raw and decimated data that overlapped each other for
a frequency range of four octaves. This overlap provided a
consistancy check for the estimates.

As a further consistancy check, two methods of spec-
tral estimation were used: smoothed fast Fourier transforms
(FFT) of Kaiser-windowed data, and least-squares autoregressive
(AR) models. Both methods were used to estimate autospectra,
cross-spectra, and squared coherencies for the two channels of
gradiometer noise.

These spectral quantities are defined in terms of the correlation functions $(R_{II}(\tau), R_{CC}(\tau), R_{IC}(\tau))$ of the inline and cross-channel noise signals, which are respectively denoted $\Gamma_I(t)$ and $\Gamma_C(t)$. The correlation functions are

$$R_{II}(\tau) = E\left[\Gamma_I(t+\tau)\, \Gamma_I(t)\right]$$

$$R_{CC}(\tau) = E\left[\Gamma_C(t+\tau)\, \Gamma_C(t)\right] \qquad (2.3-1)$$

$$R_{IC}(\tau) = E\left[\Gamma_I(t+\tau)\, \Gamma_C(t)\right]$$

where "E" denotes the expected value, t is time, and τ is the time shift.

The autospectra of the inline and cross-channel noises are the Fourier transforms of their respective correlation functions

$$S_{II}(f) = \int_{-\infty}^{\infty} R_{II}(\tau)e^{-i2\pi f\tau}d\tau$$

$$(2.3-2)$$

$$S_{CC}(f) = \int_{-\infty}^{\infty} R_{CC}(\tau)e^{-i2\pi f\tau}d\tau$$

and the cross-spectrum is

$$S_{IC}(f) = \int_{-\infty}^{\infty} R_{IC}(\tau)e^{-i2\pi f\tau}d\tau \qquad (2.3-3)$$

where f is the frequency, $-\infty < f < \infty$. These power spectra are "two-sided," which means that the mean-square value of each noise signal is computed by integrating its spectrum over both positive and negative value of frequency, e.g.

$$E\left[\Gamma_I^2\right] = \int_{-\infty}^{\infty} S_{II}(f)dt \qquad (2.3-4)$$

The squared coherency between the inline and cross-channel noises is

$$C(f) = \frac{|S_{IC}(f)|^2}{S_{II}(f)\ S_{CC}(f)} \qquad (2.3-5)$$

This function is useful in analyzing gradiometer data because it indicates whether correlations between the noise signals $\Gamma_I(t)$ and $\Gamma_C(t)$ need to be included in gradiometer error models for survey simulations. The values of $C(f)$ fall in the range from 0 to 1 and indicate the fraction of power that is common to $\Gamma_I(t)$ and $\Gamma_C(t)$ as a function of frequency. If the inline and cross-channel noises are uncorrelated, then $C(f) = 0$, while $C(f) = 1$ indicates that the two noises are deterministically related to each other by a linear transformation. If $C(f) \ll 1$, then the cross and inline-channel noises can be modeled as uncorrelated processes.

2.3.1 Fast Fourier Transform (FFT)

The FFT method of spectral estimation consists in multiplying the data time series by a data window and then fast Fourier transforming the result. The Kaiser window was used; it has the values (Ref. 14)

$$W_k = I_0\left(\alpha\sqrt{1-\left(\frac{2k-n-1}{n-1}\right)^2}\right)\Big/ I_0(\alpha) \qquad (2.3-4)$$

where

$k = 1, 2, \ldots, n$

$W(k)$ = window value at the kth sample

I_o = modified Bessel function of order zero

n = number of samples in the time series block being analyzed (1024 for this study)

α = resolution parameter (7 for this study).

The value of the resolution parameter was chosen to provide large side-lobe attenuation in the frequency domain (72 dB) while preserving adequate frequency resolution with a major-lobe width of nine frequency bins (one frequency bin is equal to the sampling frequency divided by n).

For each block of windowed data an unsmoothed spectral estimate was obtained by fast Fourier transforming the block and then computing the periodogram, which for windowed data is the squared modulus of the spectrum divided by the sum of the squares of the window values. This periodogram is an unbiased estimate of spectral density when the original data are a sample of stationary white noise.

The unsmoothed spectral estimate has low precision (large variance). Smoothing was performed on the decimated data by computing unsmoothed estimates from as many blocks as were available and then averaging them together at each frequency in the FFT. Five of these data blocks were available for SAV and seven were available for SAH. Five to seven block averages were also used to smooth the high-frequency estimates from raw data.

The resulting spectral estimates, when plotted with respect to logarithmic scales, showed that additional smoothing was warranted at mid and high frequencies. This was implemented

22

by performing a running mean on the spectral estimates. The number of frequency bins in this mean was adjusted so that each average was performed over an interval of frequencies having a width equal to 30% of its center frequency. This "constant percentage bandwidth" running mean provided final spectral estimates having a nearly constant frequency resolution when plotted against a logarithmic frequency axis. The center frequencies were chosen to avoid overlap of adjacent means.

The resulting estimates for autospectra and magnitudes of cross-spectra are shown in Figs. 2.3-1 to 2.3-6, where the dotted lines show the sample standard errors (one sigmas) of the estimates. The highest frequency in these estimates is 24 millihertz (mHz), which is the cut-off frequency of the lowpass filter in the Bell gradiometer. Above this frequency the self-noise spectra fall sharply due to the filter cut-off rate of 24 decibels (dB) per octave. The lowest frequency in the estimates is the reciprical of the block length of the decimated data (1.5 days).

Although the cross-spectral estimates are statistically significant at most frequencies, their magnitudes are small compared to the corresponding autospectra for the two output channels of the gradiometer. This implies that the inline and cross-channel noises can be modeled as uncorrelated for the purposes of estimating gravity gradients from gradiometer measurements.

2.3.2 Autoregressive Model Fitting

The second method of spectral estimation that was used in this study is called least-squares autoregressive (AR) model fitting (Ref. 15-20). The AR method has the merit of yielding spectral estimates with greater accuracy than the FFT technique when the data can be modeled by an autoregressive

23
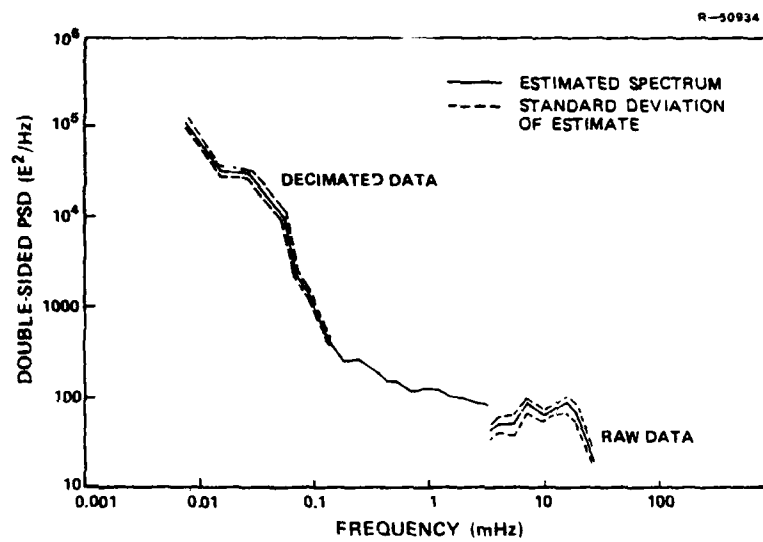
Figure 2.3-1   Self-Noise Autospectrum (Inline Channel, SAH, 9 March Data, FFT Estimates)
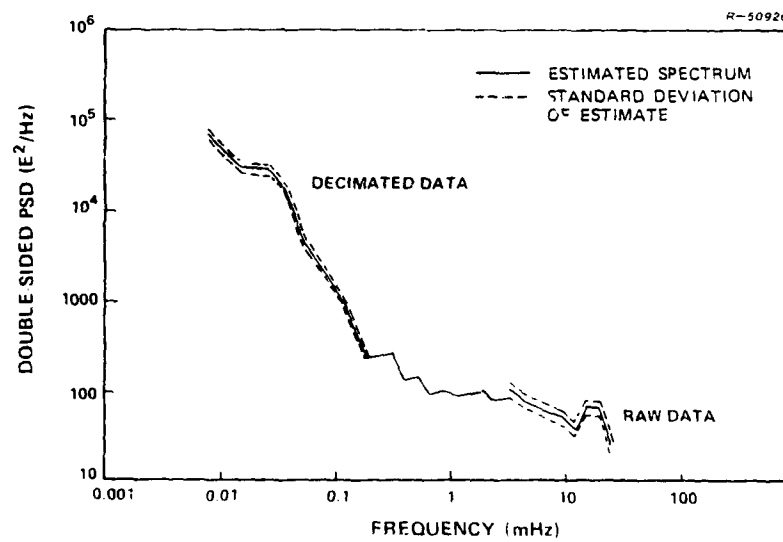
Figure 2.3-2   Self-Noise Autospectrum (Cross Channel, SAH, 9 March Data, FFT Estimates)

24
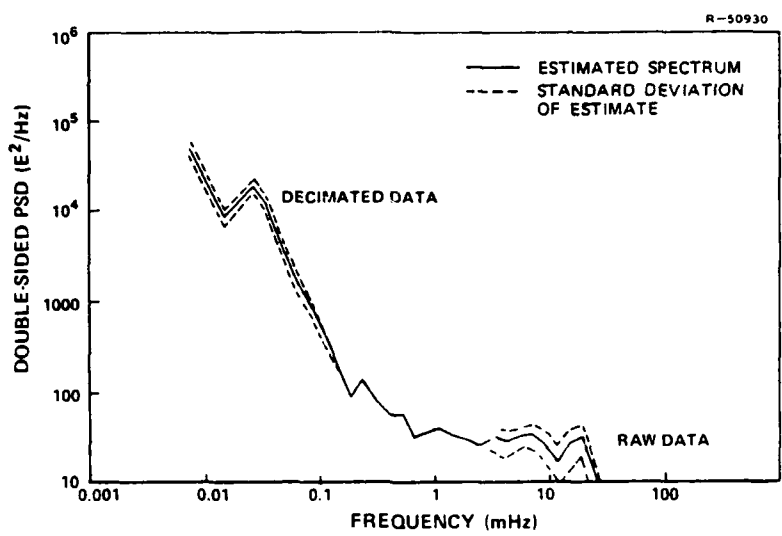
Figure 2.3-3   Self-Noise Cross-Spectrum (Inline and
                  Cross Channels, SAH, 9 March Data,
                  FFT Estimates)
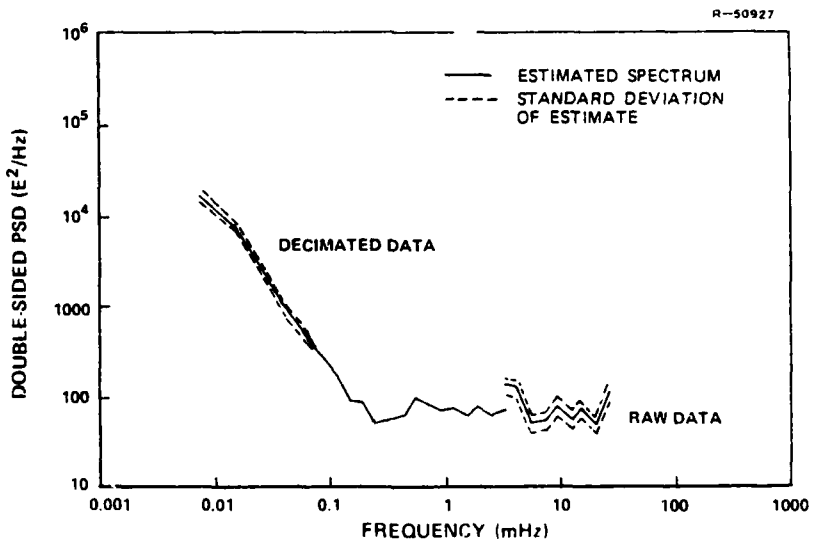
Figure 2.3-4   Self-Noise Autospectrum (Inline Channel,
                  SAV, 25 April Data, FFT Estimates)
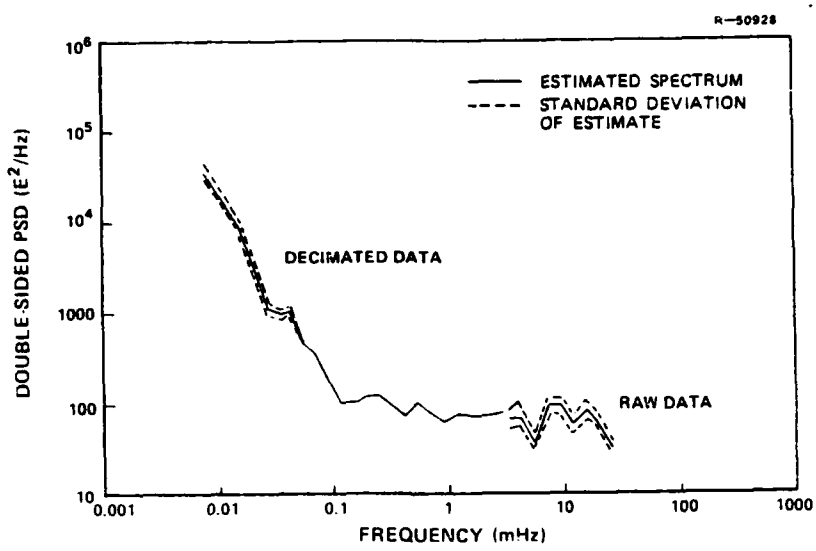
Figure 2.3-5   Self-Noise Autospectrum (Cross Channel, SAV, 25 April Data, FFT Estimates)
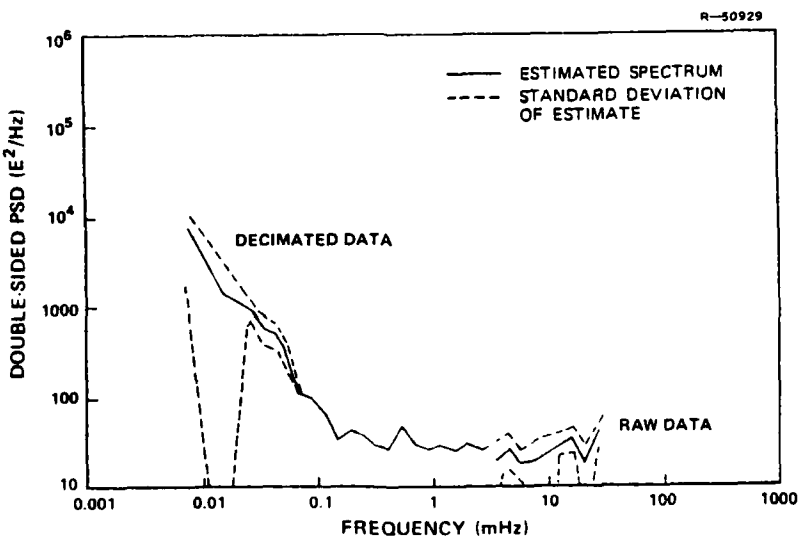
Figure 2.3-6   Self-Noise Cross-Spectrum (Inline and Cross Channels, SAV, 25 April Data, FFT Estimates)

model of sufficiently low order. Other names associated with this approach to spectral estimation are "maximum entropy," "linear prediction," and "all-pole modeling."

The AR method used in this study is explained in the following. Suppose the vector $\underline{x}(k)$ is the kth sample of a vector time series of data, where $k = 1,2,\ldots,n$. (In analyzing gradiometer self-noise data for this report, $n = 1024$ and $\underline{x}(k)$ was two-dimensional because the cross and inline-channel outputs were simultaneously measured.) Suppose further that $\hat{\underline{x}}(k)$ is an estimate of $\underline{x}(k)$. The error of this estimate is then defined as $\underline{e}(k) = \underline{x}(k) - \hat{\underline{x}}(k)$. Therefore

$$\underline{x}(k) = \hat{\underline{x}}(k) + \underline{e}(k) \qquad (2.3\text{-}5)$$

The AR method is based on the assumption that the errors $\underline{e}(k)$, $k=1,2,\ldots,n$, are a sample of zero-mean stationary white noise when each estimate $\hat{\underline{x}}(k)$ is chosen to be the best linear one-step-ahead prediction.

$$\hat{\underline{x}}(k) = A_1\underline{x}(k-1) + A_2\underline{x}(k-2) + \ldots + A_p\underline{x}(k-p),$$
$$k = p+1, p+2,\ldots,n \qquad (2.3\text{-}6)$$

In this equation the positive number p is called the order of the predictor, while the square matrices A_1, $A_2,\ldots A_p$, which contain real numbers, are called parameter arrays. Using (2.3-6) in (2.3-5) yields the following AR model for $\underline{x}(k)$

$$\underline{x}(k) = A_1\underline{x}(k-1) + A_2\underline{x}(k-2) + \ldots + A_p\underline{x}(k-p) + \underline{e}_f(p,k),$$
$$k = p+1,\ldots,n \qquad (2.3\text{-}7)$$

where the one-step-ahead or forward prediction error is $\underline{e}_f(p,k)$.

The data time series $\underline{x}(k)$, $k=1,2,\ldots,n$, is modeled as a sample from a stationary random process. Therefore, it also makes sense to define a one-step-back predictor

$$\hat{\underline{x}}(k) = B_1\underline{x}(k+1) + B_2\underline{x}(k+2) + \ldots + B_p\underline{x}(k+p)$$
$$k = 1,2,\ldots,n-p \qquad\qquad (2.3-8)$$

Using Eq. 2.3.-8 in Eq. 2.3-5 yields a second AR model for $\underline{x}(k)$

$$\underline{x}(k) = B_1\underline{x}(k+1) + B_2\underline{x}(k+2) + \ldots + B_p\underline{x}(k+p) + \underline{e}_b(p,k),$$
$$k = 1,2,\ldots n-p \qquad\qquad (2.3-9)$$

where the one-step-back or backward prediction error is $\underline{e}_b(p,k)$. The AR method is based on the assumption that this backward prediction error sequence is also a sample of zero-mean stationary white noise when the parameter arrays B_1, $B_2,\ldots B_p$ are optimally chosen.

By specifying the order p, the parameter arrays, and the covariance matrix of the prediction errors for an AR model, one determines an estimate of the power spectrum of the process generating the time series. The forward AR model yields the estimated spectral matrix

$$S_F(F) = A^{-1}(F)C_F A^*(F), \quad |F| < 1/2$$
$$F = f/f_{sa} = \text{frequency/sampling frequency}$$
$$A^* = \text{complex conjugate transpose of A}$$
$$A(F) = I - \sum_{k=p+1}^{n} A_k \exp(i2\pi kF) \qquad\qquad (2.3-10)$$
$$I = \text{identity matrix}$$
$$C_F = \text{covariance matrix of } \underline{e}_f(p,k)$$

28

The matrix $f_{sa}^{-1}S_F(f/f_{sa})$, where f_{sa} = sampling frequency of the data series, contains estimates of autospectra along its diagonal and estimates of cross-spectra in its off-diagonal locations.

A similar formula yields the spectral estimates produced by backward predictors

$$S_B(F) = B^{-1}(F)C_B B^*(F), \quad |F| < 1/2 \qquad (2.3.-11)$$

Several methods for optimally fitting AR models to vector time series have been discussed in the literature. The method used in the present study satisfies the following requirements, which are appropriate for the purposes of spectral estimation: For specified order p, sample size n, and time series $\underline{x}(k)$, the sum of the squared forward and backward prediction errors, SE(p), is minimized subject to the requirement that the forward and backward estimates of the spectrum must be identical. In other words, the parameter matrices A_i, B_i, $i=1,2,\ldots,p$, and covariance matrices C_F and C_B are chosen to minimize

$$SE(p) = \sum_{k=p+1}^{n} |\underline{e}_f(p,k)|^2 + \sum_{k=1}^{n-p} |\underline{e}_b(p,k)|^2 \qquad (2.3-12)$$

$$|\underline{e}_{f,b}(p,k)|^2 = \underline{e}_{f,b}^*(p,k)\underline{e}_{f,b}(p,k) = \text{inner product}$$

subject to the constraints that Eqs. 2.3.2-3 to 2.3.2-7 are satisfied and the two spectral estimates are equal:

$$S_F(F) = S_B(F), \quad |F| < 1/2 \qquad (2.3-13)$$

The algorithm used for computing the solution to this problem recursively was presented in Ref. 15.

The AR spectral estimate obtained for a particular time series depends on the order p of the model. In this study the Akaike information criterion (AIC statistic) was used to select the value of p for each time series analyzed (Refs. 18 through 20). AR models were fitted for p = 1,2,...20, and the value of AIC was computed in each case. The value of p that yielded the minimum value of AIC was then used to compute the spectral estimate. This method of order selection was employed because it can be derived from basic information-theoretic principles and has been found to be suitable for a wide variety of estimation problems (Refs. 18-20).

Standard errors (standard deviations) were computed for selected AR spectra to assess their precisions. The parameter covariance routines in PARAIDE^{TM} were used for this purpose. These routines compute the inverse Fisher information matrix corresponding to the particular AR model under study. This information matrix equals the covariance matrix of the parameters in the parameter arrays of the AR model when the one-step prediction errors of the model are Gaussian and the sample size is large.

Small perturbations in the AR parameter values produce small perturbations in the AR spectra of the gradiometer data because the spectra are free of lightly damped resonances in the frequency range of interest. These perturbations are related to each other through sensitivity functions that can be computed from the AR model. Therefore, one can estimate the standard deviations of the spectrum estimates due to the sampling variability of the AR parameters by computing these

---

PARAIDE, a trademark of The Analytic Sciences Corporation, refers to a set of computer routines for parameter identification and stochastic modeling.

30

sensitivity functions together with the covariance matrix of
the AR parameters (inverse Fisher information matrix).

Gradiometer self-noise data were analyzed in blocks
containing 1024 pairs of measurements of the inline and cross-
channel outputs. The resulting AR spectral estimates were
then plotted at 512 frequencies, which correspond to the fre-
quency bins of a 1024 sample FFT. Typical examples of the
results obtained in this way for the SAH orientation are shown
in Figs. 2.3-7 to 2.3-11, where the dotted lines are the com-
puted standard errors (one sigmas) for the estimates. Similar
results were obtained for the SAV orientation except that the
low-frequency rise in the auto and cross-spectra occured at a
lower frequency.

A few comments on the interpretation of AR spectral
estimates are useful at this point. In Figs. 2.3-7 through
2.3-9, the estimates from decimated data have ripples above
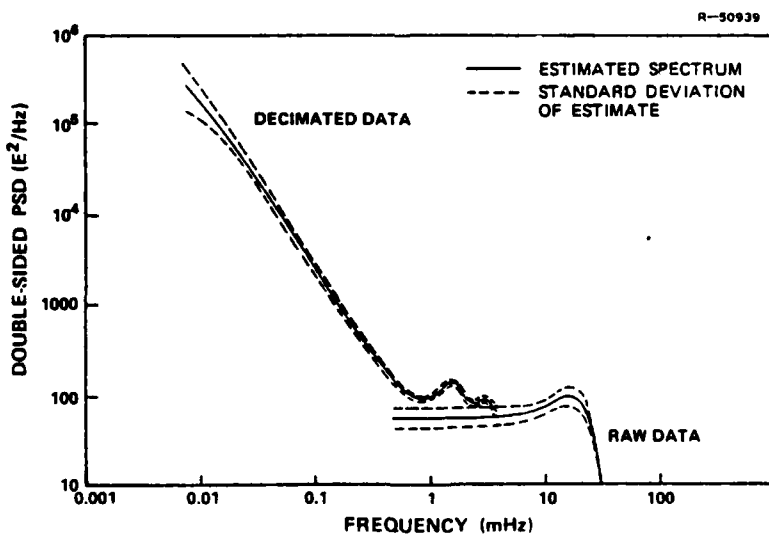
Figure 2.3-7   Self-Noise Autospectrum (Inline Channel,
                SAH, 9 March Data, AR Estimates)

31
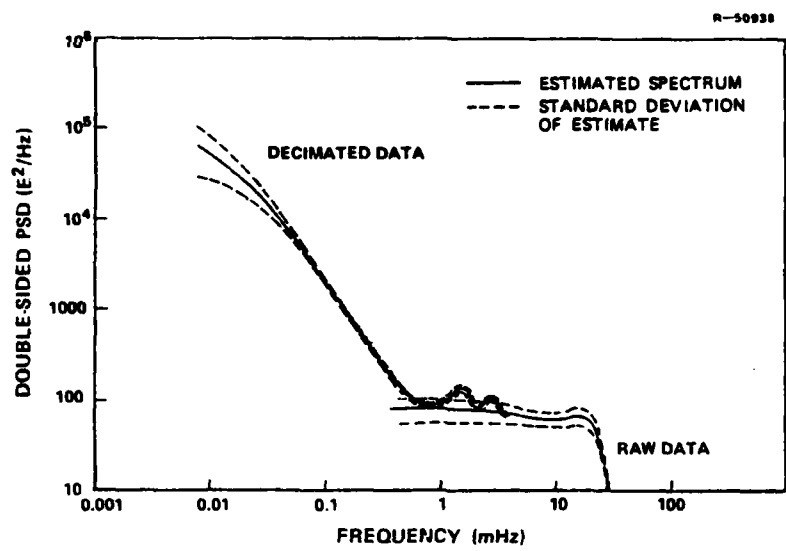
Figure 2.3-8   Self-Noise Autospectrum (Cross Channel,
   SAH, 9 March Data, AR Estimates)
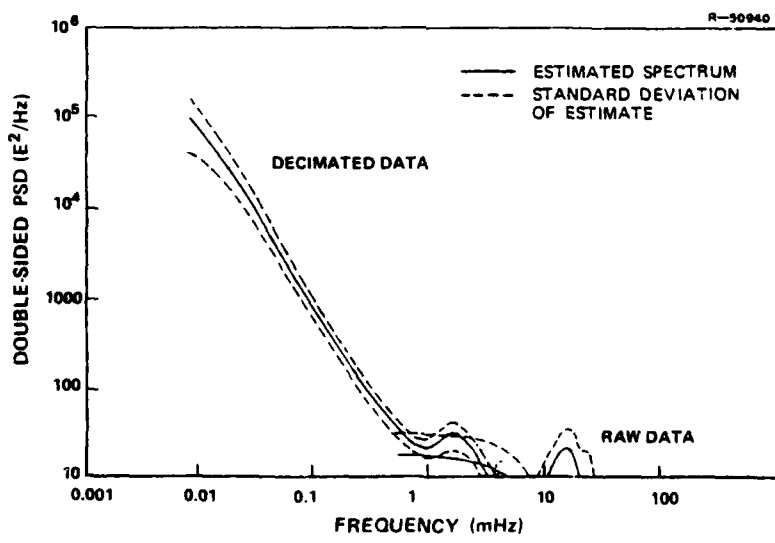
Figure 2.3-9   Self-Noise Cross-Spectrum (Inline and
   Cross Channels, SAH, 9 March Data,
                AR Estimates)

32
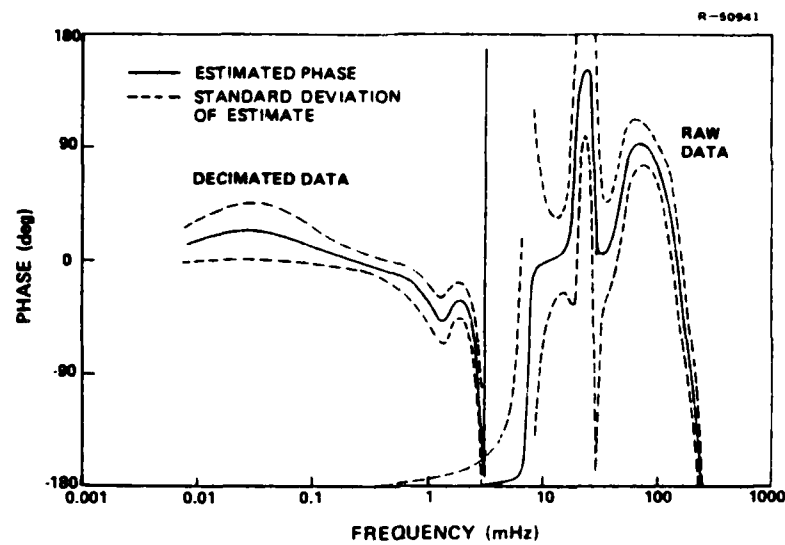
Figure 2.3-10   Self-Noise Cross-Spectral Phase (Inline
and Cross Channels, SAH, 9 March Data,
AR Estimates)
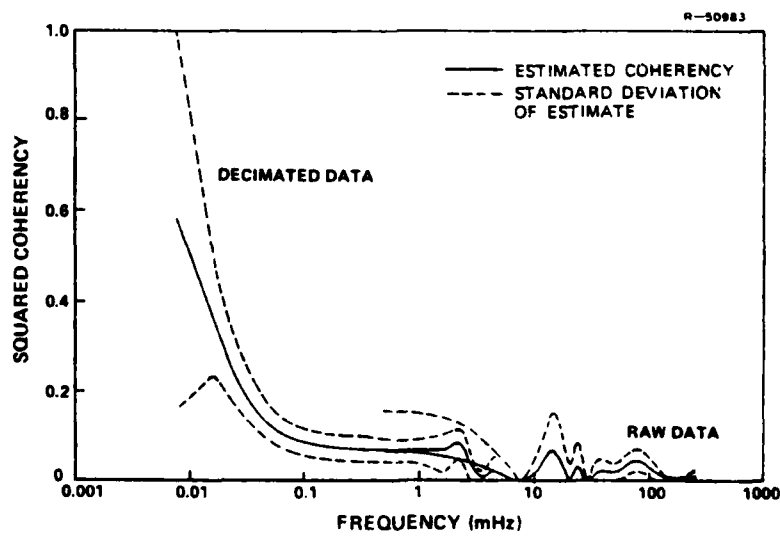
Figure 2.3-11   Self-Noise Coherency (Inline and Cross
Channels, SAH, 9 March Data, AR Estimates)

33

0.5 mHz. This is typical behavior for AR spectra derived from data containing both low-frequency random drift and white noise. The spectral estimates from raw data, in contrast, are free of ripples because they are derived from data batches having short durations (34 minutes). This duration is appropriate for high-frequency analysis but is too short to yield an accurate estimate of the spectrum at low frequencies, which characterizes the long-term random drift. Therefore, the spectra from decimated and raw data are expected to have different qualities in their frequency range of overlap from 0.5 mHz to 3.9 mHz. The differences between decimated and raw estimates are judged to be statistically insignificant at a two-sigma (95%) confidence level.

Two conclusions can be drawn from these AR spectral estimates. The first is that the self noises in the two output channels are uncorrelated for the purposes of gravity gradient measurements. This conclusion derives from the AR coherency plot in Fig. 2.3-11, which indicates less than 10% coherency in the frequency bands where the estimates are statistically significant.

The second conclusion is that the AR spectral estimates based on decimated data are statistically consistent with the high-frequency estimates derived from raw data, i.e. in the frequency range of their overlap the two-sigma (95%) confidence intervals of the estimates intersect each other. (The dotted curves in the spectral plots (Figs. 2.3-7 to 2.3-11) are only one-sigma (68%) confidence intervals). The one exception to this consistency occurs in the phase of the cross-spectrum

(Fig. 2.3-10). Fortunately, precise estimates of this phase
function are not needed for developing gradiometer error models
because the two output channels contain essentially incoherent
noises.

Three sets of AR spectral estimates, such as illus-
trated in Figs. 2.3-7 to 2.3-11, were compared with each other
to validate the use of a stationary model for the gradiometer's
self noise. These estimates were generated from non-overlapping
blocks of both SAH and SAV decimated and raw data. The com-
parisons showed no statistically significant evidence of non-
stationary behavior in the frequency range below 24 mHz, i.e.,
the two-sigma confidence intervals of paired estimates over-
lapped each other. At higher frequencies, above 50 mHz, non-
stationary behavior was observed in the form of time-varying
narrow-band spectral peaks in both the spectrum and coherency
plots for SAH and SAV. These components were above the in-
tended 24 mHz cutoff frequency of the Butterworth low-pass
filters in the gradiometer and did not contribute significant
power to the self noise. For survey applications requiring
one measurement every 10 seconds, these resonances would not
be a practical concern because the required bandwidth is 50
mHz.

2.4   SELF-NOISE MODELS

2.4.1 Spectral Model

The spectral estimates for the Bell baseline GGI ob-
tained by the FFT and AR methods support each other and lead
to three important conclusions.

- At lower frequencies ($|f| < 0.1$ mHz) the autospectra are inversely proportional to the frequency squared (trend = -20 dB/decade)

- At high frequencies (2 mHz < $|f|$ < 24 mHz) the autospectra are independent of frequency

- Over the range of frequencies relevant to airborne gradiometric surveys 0.01 mHz < $|f|$ < 50 mHz, the self noises in the inline and cross channels are incoherent and have nearly the same autospectra.

In view of these results, an appropriate analytic noise model, which summarizes all of the FFT and AR spectral estimates for the Bell baseline GGI, consists of two uncorrelated processes with power spectra

$$S_{SAV}(f) = \frac{R_{SAV}}{f^2} + W_{SAV} \qquad 0.01 \text{ mHz} < |f| < 24 \text{ mHz}$$

$$(2.4-1)$$

$$S_{SAH}(f) = \frac{R_{SAH}}{f^2} + W_{SAH} \qquad 0.01 \text{ mHz} < |f| < 24 \text{ mHz}$$

These models correspond, respectively, to spin-axis-vertical (SAV) and spin-axis-horizontal (SAH) orientations of the gradiometers. (Results presented in Sections 2.5 and 2.6 show that similar formulas also apply to the Bell Ball-Bearing GGI and the Draper Floated Gravity Gradiometer No. 2.) Both the inline and cross-channel noise have these spectra. The positive constants R_{SAV} and R_{SAH} have the units of $E^2 \cdot Hz$ and determine the strength of the "red" noise* at lower frequencies.

---

*The term "red" noise refers to noise with a power spectrum proportional to $1/f^2$. This is a natural extension of the term "pink" noise, which is established nomenclature for acoustical signals having spectra proportional to $1/f$.

36

The positive constants W_{SAV} and W_{SAH} have the units E^2/Hz and determine the strength of the white noise at higher frequencies. The lower frequency limit of 0.01 mHz for this model corresponds to a period of 28 hours and is determined by the manner in which the data were analyzed. This frequency limit is consistent with the fact that simulations of airborne surveys do not require lower frequencies. The upper frequency limit of 24 mHz, on the other hand, was the result of the Butterworth filters in the gradiometer, which cause the spectra to decrease sharply above this frequency.

2.4.2 Time-Domain Markov Model

A Markov model consistent with the spectra in Eqs. 2.4-1 is shown in Fig. 2.4-1, where the symbols R and W denote the red and white noise parameters. The small parameter f_o is required for this model to yield stationary self noise. Its value within the range $0 \text{ Hz} < f_o < 10^{-6} \text{ Hz}$ is arbitrary for
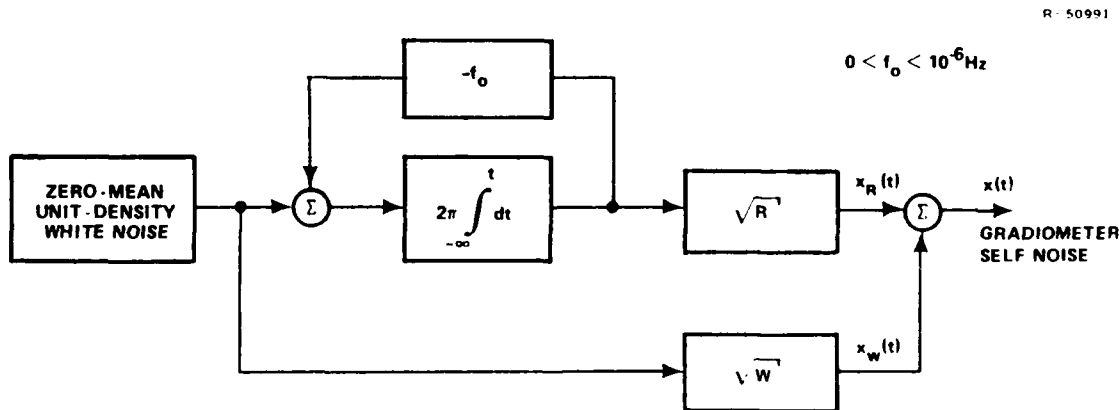
$$0 < f_o < 10^{-6} Hz$$

Figure 2.4-1   Markov Model of Self Noise, Validated for Frequencies Ranging from 0.01 mHz to 24 mHz

the purpose of modeling self noise in the frequency range above
0.01 mHz (periods less than 28 hours). The value $f_o = 10^{-6}$ Hz
yields a minimum-variance model consistent with the spectral
estimates. The white noise driving this model has a power
spectral density equal to unity.

Numerical values for the noise parameters R and W
were computed by individually fitting R and W values to all of
the TASC spectral estimates (both FFT and AR) and then comput-
ing the mean values of R and W for both SAV and SAH orienta-
tions. The results for the Bell baseline GGI are

$$
\begin{aligned}
R_{SAV} &= 2.0 \times 10^{-6} \ E^2 \cdot Hz \\
R_{SAH} &= 16 \times 10^{-6} \ E^2 \cdot Hz \\
W_{SAV} &= 81 \ E^2/Hz \\
W_{SAH} &= 86 \ E^2/Hz
\end{aligned}
\tag{2.4-2}
$$

The resulting power spectral densities (PSD's) computed from
Eqs. 2.4-1 are shown in Fig. 2.4-2. These models apply equal-
ly to the gradiometer's inline and cross channels. The cross-
spectrum between these channels is modeled to be zero because
of the small coherency in the FFT and AR spectral estimates.

2.4.3 Estimated Random Drift

A model for random drift in the gradiometer outputs
is implied by the self-noise power spectra. If $x(t)$ denotes
the output in eötvös at time t of either the inline or cross
channel, then the random drift over an interval T can be de-
fined as

$$
d(T) = x(t + T) - x(t)
\tag{2.4-3}
$$
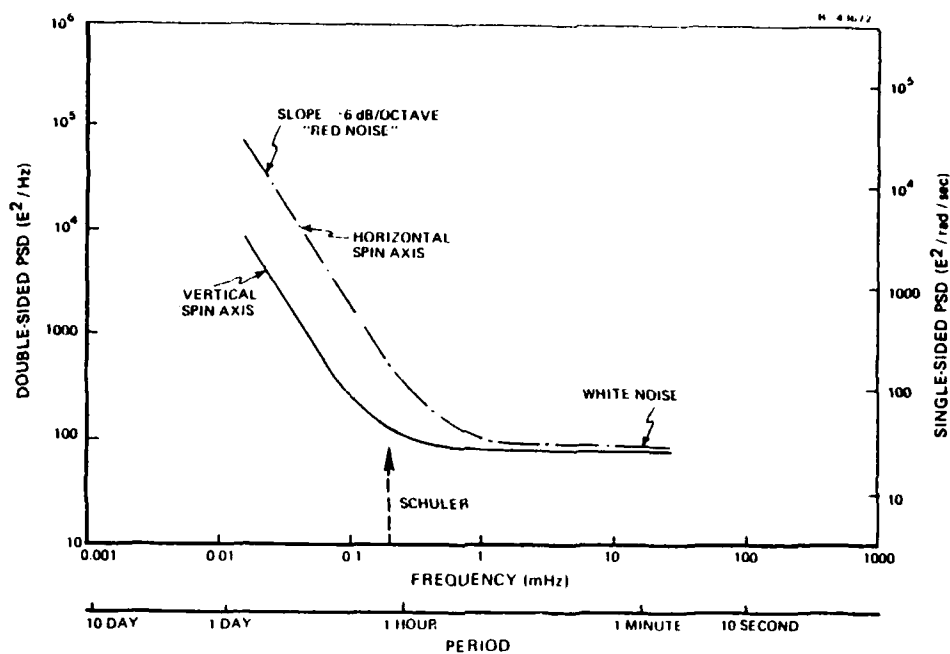
Figure 2.4-2   ARMA Models of Bell Gradiometer Self-Noise,
                Based on Smoothed FFT's and Least-Squares
                Autoregressive Models

Note that $d(T)$ is the accumulated end-to-end drift over the
interval T, as opposed to a drift rate. It can be shown that
the expected value of this drift is zero, and its variance
$\sigma_d^2(T)$ is

$$\sigma_d^2(T) = 2[R_{xx}(0) - R_{xx}(T)] \qquad (2.4-4)$$

where $R_{xx}(T) = E[x(t + T) x(t)]$ is the autocorrelation func-
tion of the self noise $x(t)$.

When this expression is evaluated for the Markov model,
it is found that the following approximation is valid for T_{ave}
$< T < 10^5$ s

$$\sigma_d{}^2(T) \simeq 4\pi^2 T \, R + 2 \, W/T_{ave} \qquad\qquad (2.4\text{-}5)$$

$$T_{ave} = \text{measurement averaging time (20 s for} \\ \text{24 mHz bandwidth)}$$

where R is the red-noise parameter ($E^2 \cdot Hz$) and W is the white-noise floor (E^2/Hz); see Eqs. 2.4-2. The rms random drift $\sigma_d(T)$ is plotted as a function of the drift time T in Fig. 2.4-3. The larger rms drift for the horizontal, as compared to the vertical spin axis, corresponds to the higher level of red self noise produced by the horizontal orientation. This figure indicates that the accumulated rms drift over the duration of a 5-hour gravity survey would be 3.0 E for SAV and 4.4 E for SAH. If the bandwidth of the gradiometer were increased to 50 mHz (10 second averaging time), then these values would increase to 4.2 E for SAV and 5.3 E for SAH.

A—50937
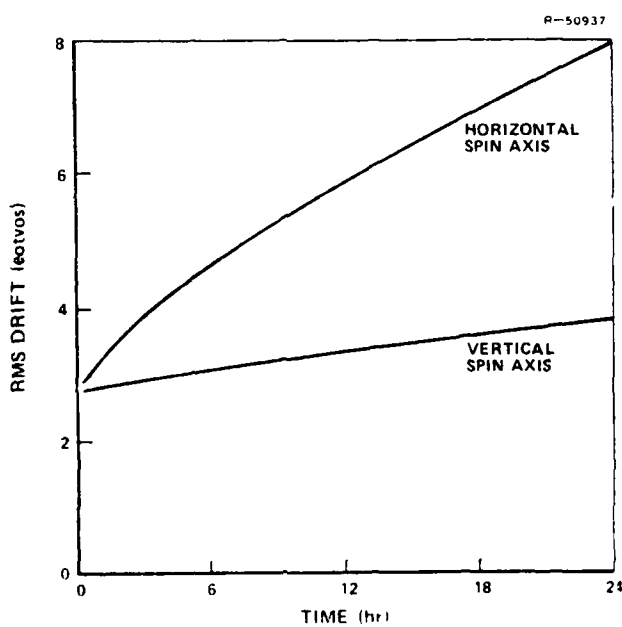
Figure 2.4-3   Computed RMS Random Drift for Bell Baseline
GGI Based on Self-Noise Models for $|f| <$ 24 mHz

2.4.4 Comparison of TASC, BELL, and NSWC/DL Spectral Estimates

Bell presented averaged and smoothed FFT autospectra on the SAV and SAH orientation of their baseline GGI in Ref. 1. In addition, Naval Surface Weapons Center/ Dahlgren (NSWC/DL) generated an averaged FFT autospectrum for SAH. These spectral estimates and the TASC estimate agree as shown in Fig. 2.4-4. The slightly reduced level of the Bell estimate below 0.2 mHz may be due to their use of a different data set as compared to NSWC/DL and TASC. The differences between estimates below 0.02 mHz are attributed to the finite length of the data time series and the different methods that were used in processing the data. Since these differences occur at frequencies corresponding to 1-day time periods, they are not important for airborne survey modeling.
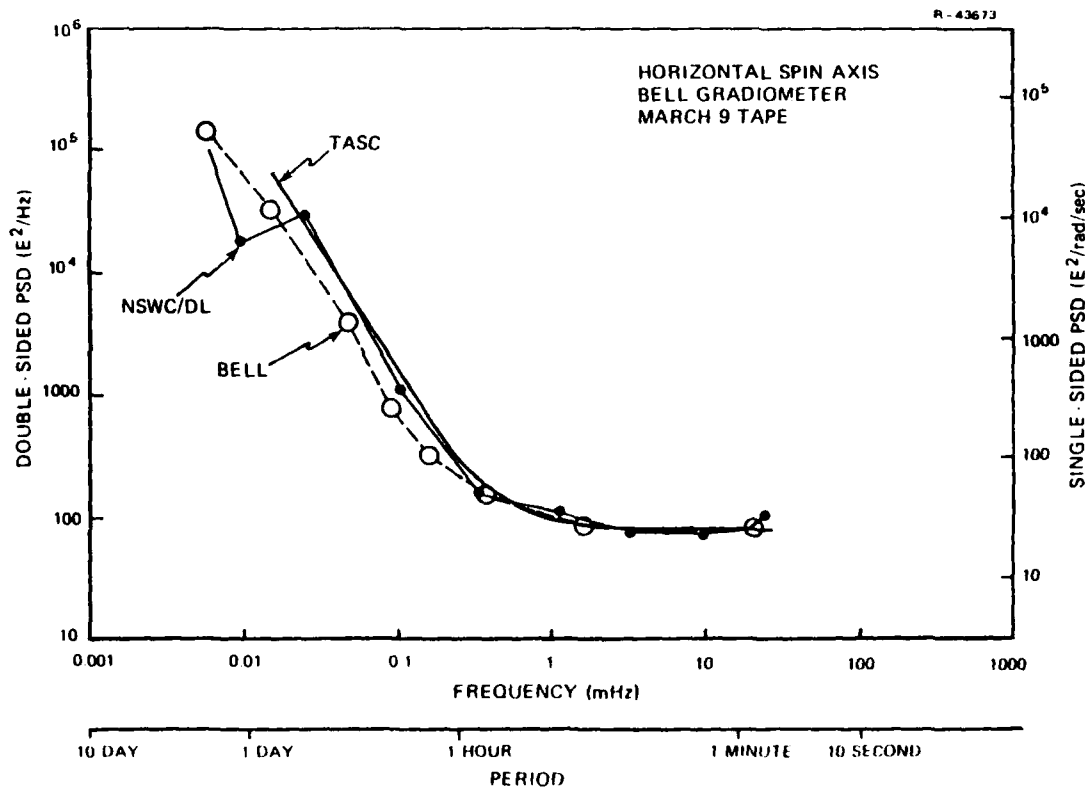
Figure 2.4-4   Comparison of Spectral Estimates

41

2.5   NOISE SPECTRA FOR THE BELL BALL-BEARING GGI

Self-noise data for the Bell prototype Ball-Bearing gradiometer recently became available. These data were spectrally analyzed using the AR technique, and the resulting self-noise autospectra are shown in Fig. 2.5-1 along with the analytic model for the Bell baseline GGI.
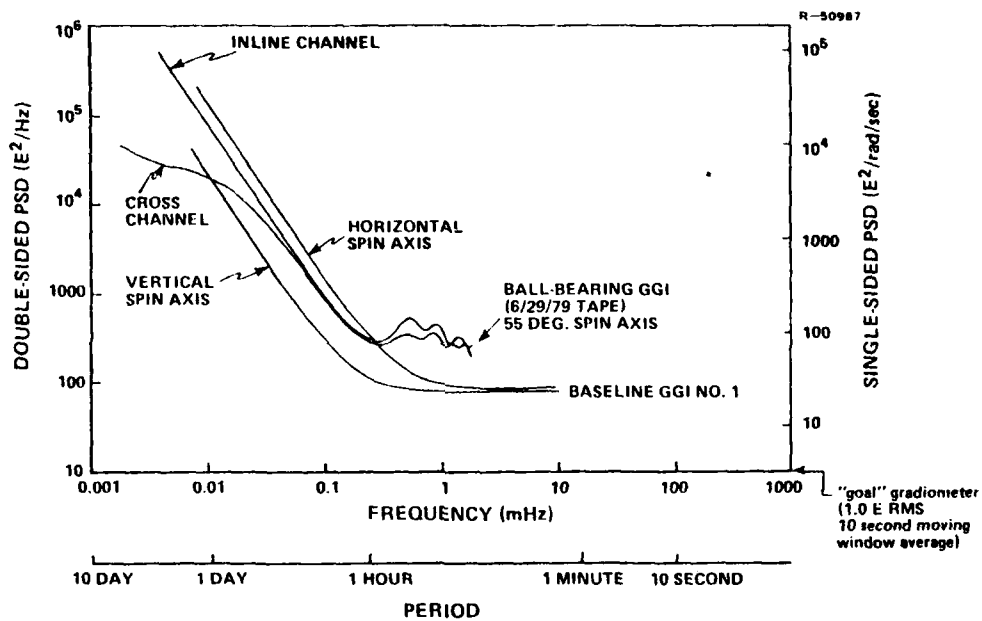
Figure 2.5-1   Comparison of Self-Noise Autospectra for Bell Baseline and Ball-Bearing GGI's

The Bell Ball-Bearing GGI (BB GGI) was operating with its spin axis inclined 55 degrees with respect to the vertical. This is the intended orientation for future moving-base applications. The BB GGI data spanned six days with a sampling frequency of 0.5 Hz. To provide a low-frequency noise spectrum, these data were decimated 128:1, which yielded 2074 data pairs at a reduced sampling frequency of 3.91 mHz. A ramp was removed from each channel of data (0.92 E/hr in the inline

42

channel and 0.30 E/hr in the cross-channel), and an AR model
was fitted to the residuals by minimizing the sum of the squares
of the one-step prediction errors (Ref. 15). The AIC statistic
(Refs. 18 through 20) dictated an order 9 model (out of a maxi-
mum permitted order of 24). In Fig. 2.5-1, the resulting auto-
spectra for inline and cross-channel noises of the BB GGI show
small ripples at high frequencies that are typical of high-order
AR spectra with white-noise floors. The BB GGI has a white-noise
floor that is about four times higher than that of the baseline
GGI, which corresponds to twice as much short-term variability
on an rms basis. The rising low-frequency parts of the spectra
indicate more long-term drift in the inline channel as compared
to the cross channel of the BB GGI. At frequencies between
0.01 mHz (1 day period) and 0.3 mHz (1 hour period), the in-
line and cross-channel noise spectra of the BB GGI fall between
the baseline spectra for vertical and horizontal spin axes.

For reference purposes, the spectrum level at the
bottom of Fig. 2.5-1 corresponds to the white-noise level of a
fictitious "goal" gradiometer that is free of long-term drift
and has an rms self noise of 1.0 eötvös with a 10 second aver-
aging time between measurements.

2.6   SELF-NOISE MODEL FOR THE DRAPER FLOATED GRADIOMETER

Noise data were spectrally analyzed for the Draper
Floated Gravity Gradiometer (FGG No. 2). An overview of the
largest data set is shown in Fig. 2.6-1, where the output sig-
nals of the FGG are resolved into independent cross gradients,
Γ_{WZ} and Γ_{WL}; these are defined by the gradiometer's axis of
weights and two orthogonal axes, denoted Z and L in Draper's
documentation (Ref. 21). Fig. 2.6-1 shows the residuals after
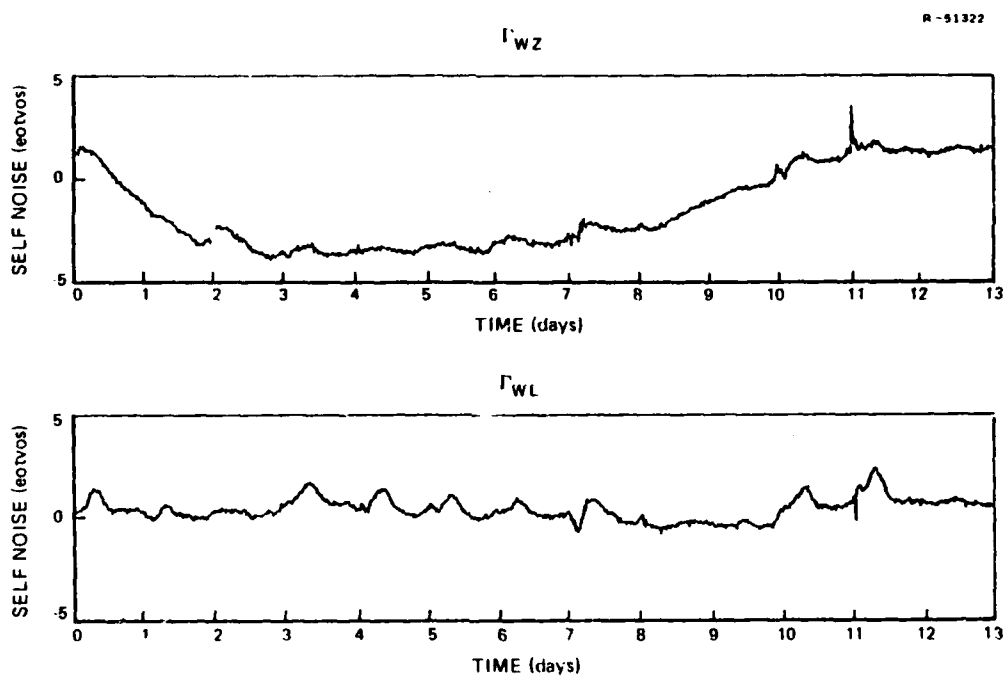
Figure 2.6-1   Draper FGG No. 2 Self-Noise Data
(9 July Tape)

ramps were subtracted from the data: 0.34 E/hr in the Γ_{WZ}
channel and 0.58 E/hr in the Γ_{WL} channel.

The data span 13 days, and the obvious periodic com-
ponents, evidenced by peaks and troughs, correlate with normal
work hours, weekends, and holidays over the period from June
23 through July 4, 1979.   Larger spikes in the data are at-
tributed by Draper to known mass disturbances in the labora-
tory environment.   Draper has also indicated that the sensi-
tivity of the FGG No. 2 to environmental temperature cycles
may have been impacted by the fact that two gradiometer tem-
perature controllers were inoperative.

Analyses by means of FFT and AR techniques indicated
that the self-noise of the FGG No. 2 can be represented ana-
lytically with the following model

$$S_{WL}(f) \approx S_{WZ}(f) = \frac{R}{f^2} + W$$

$$R = 2.0 \times 10^{-7} \ E^2 \cdot Hz \qquad (2.6\text{-}1)$$

$$W = 2.3 \ E^2/Hz$$

$$0.01 \ mHz < |f| < 50 \ mHz$$

This noise spectrum is compared with analytic models for the Bell baseline GGI in Fig. 2.6-2. The Draper white-noise floor is about three percent of Bell's; this corresponds to about 1/6 as much high-frequency noise (short-term variability) on an rms basis. A slightly larger difference between the two instruments occurs at lower frequencies.

The Draper white-noise floor falls beneath the 10 $E^2/$ Hz level of the fictitious "goal" gradiometer.[*] The bottom of *Fig. 2.6-2 represents the theoretical lower limit on self noise in the Draper gradiometer due to Brownian motion (Ref. 22).*

The rms accumulated random drift in the FGG output signals (due to self noise) is computed by means of the theory described previously in Section 2.4.3. For a gradiometer bandwidth of 24 mHz, which corresponds to the 20-second averaging time previously used for the Bell GGI, the drift variance over a time interval T is

$$\sigma_d^2(T) \cong 4 \ \pi^2 T \ R + 0.096 \ W$$

$$20 \ s < T < 10^5 \ s \qquad (2.6\text{-}2)$$

---

[*]The goal gradiometer is arbitrarily defined to have an rms error of 1 E when the output is averaged for 10 seconds. It is described further in Section 4.6.

HORIZONTAL
SPIN AXIS

VERTICAL
SPIN AXIS

10^5

10^4

10^3

DOUBLE-SIDED PSD (E²/Hz)

100

10

BELL BASELINE GGI NO.1

DRAPER FGG NO.2
$\Gamma_{WZ} \cdot \Gamma_{WL}$

10^4

10^3

100

SINGLE-SIDED PSD (E²/rad/sec)

10

SCHULER

DRAPER Brownian
motion limit

"goal" gradiometer
(1.0 E RMS ·
10 second moving
window average)

0.001   0.01   0.1   1   10   100   1000

FREQUENCY (mHz)

10 DAY   1 DAY   1 HOUR   1 MINUTE 10 SECONDS

PERIOD

Γ_{WZ} AND Γ_{WL} ARE CROSS GRADIENTS DEFINED BY THE FLOAT'S AXIS OF WEIGHTS (W) AND TWO
ORTHOGONAL AXES (Z AND L)

Figure 2.6-2   Comparison of Self-Noise Autospectra for
Draper FGG No. 2 and the Bell Baseline GGI

1.00

0.75

0.50

RMS DRIFT (eotvos)

0.25

0

0   6   12   18   24

TIME (hr)
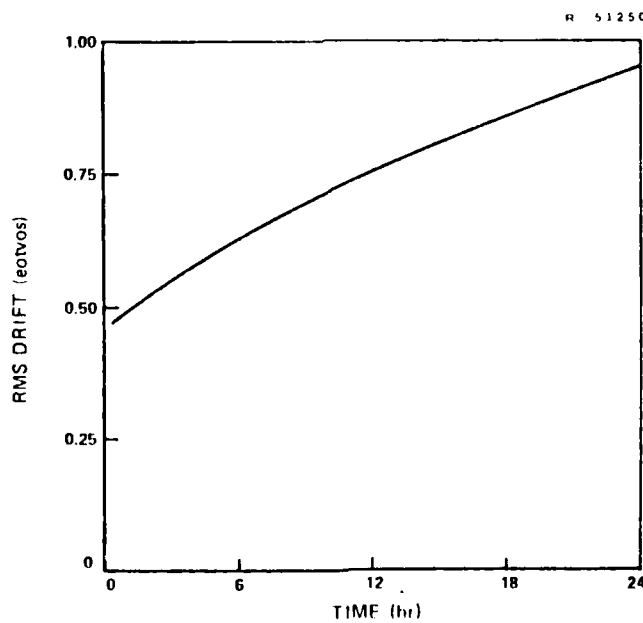
Figure 2.6-3   Computed RMS Random Drift for Draper FFG
No. 2, Based on Self-Noise Model for
|f| < 24 mHz

46

The rms drift $\sigma_d(T)$ is plotted in Fig. 2.6-3 for the self-noise model in Eq. 2.6-1. This plot indicates an rms random drift of 0.60 E over a 5-hour survey.

3.   VIBRATION-INDUCED ERRORS

3.1   INTRODUCTION

        This chapter describes vibration error models for the
Bell Gravity Gradiometer Instrument (GGI), which are based on
analyses of test data that extended over the last two years.
Vibration test data for the Draper Floated gradiometer, in
contrast, have only recently been available. As a result,
vibration models for the Draper gradiometer are not as fully
developed as those for the Bell instrument, although prelimin-
ary results are related to survey performance in Chapter 4.

        This chapter is organized as follows. In Section 3.2
a general model for vibration-induced errors is described for
the Bell GGI. This model is used in Sections 3.3 and 3.4 to
interpret the Bell data on vibration sensitivities and to de-
velop error models for the effects of aircraft vibrations such
as those occuring during airborne gravity surveys. Section
3.5 describes models for the vibration environment of an air-
borne gradiometer during a gravity survey. These models are
extrapolations based on available flight test data. Upper
bounds for vibration-induced errors during an airborne survey
are estimated in Section 3.6. The chapter closes with Section
3.7, which describes an error model for an airborne survey
system consisting of three gradiometers mounted on a single
inertial platform.

3.2 GENERAL ERROR MODEL FOR THE BELL GRAVITY GRADIOMETER

An ideal Bell gravity gradiometer is completely insensitive to linear vibrations as well as to angular vibrations about its spin axis. The only vibration-induced errors are those caused by angular vibrations about axes normal to the spin axis. (These vibrations cause centripetal gravity gradients that cannot be distinguished by the gradiometer from naturally occuring variations in the earth's gravity field.)

This ideal behavior is approximated in the Bell GGI by the use of on-line error-correcting feedback loops built into the gradiometer (Refs. 3 and 26). These loops provide corrections for accelerometer scale factor unbalances, misalignments of input axes, and even-order error coefficients (bilinear nonlinearities). They also provide correction for jitter in the spin rate.

A time-domain model of the input-output behavior of the Bell gradiometer is shown in Fig. 3.2-1. The part of this model contained within the dotted box represents an error-free gradiometer, i.e., one free of self noise, miscalibration or misalignment, and free of environmental disturbances. From a mathematical viewpoint, the error-free system has the same structure as a communications system employing coherent amplitude modulation and demodulation. The gravity gradient components $\Gamma_{yy}(t) - \Gamma_{xx}(t)$ and $\Gamma_{xy}(t)$ play the roles of modulation signals, while the sinusoids at twice the spin frequency f_s play the roles of inphase and quadrature carriers. The synchronous detector is phase locked to the gradiometer spin, which has a frequency of about 0.28 Hz. This value for f_s is much higher than the effective band limits of either the gradient signals or the lowpass output filters in the detector.

49
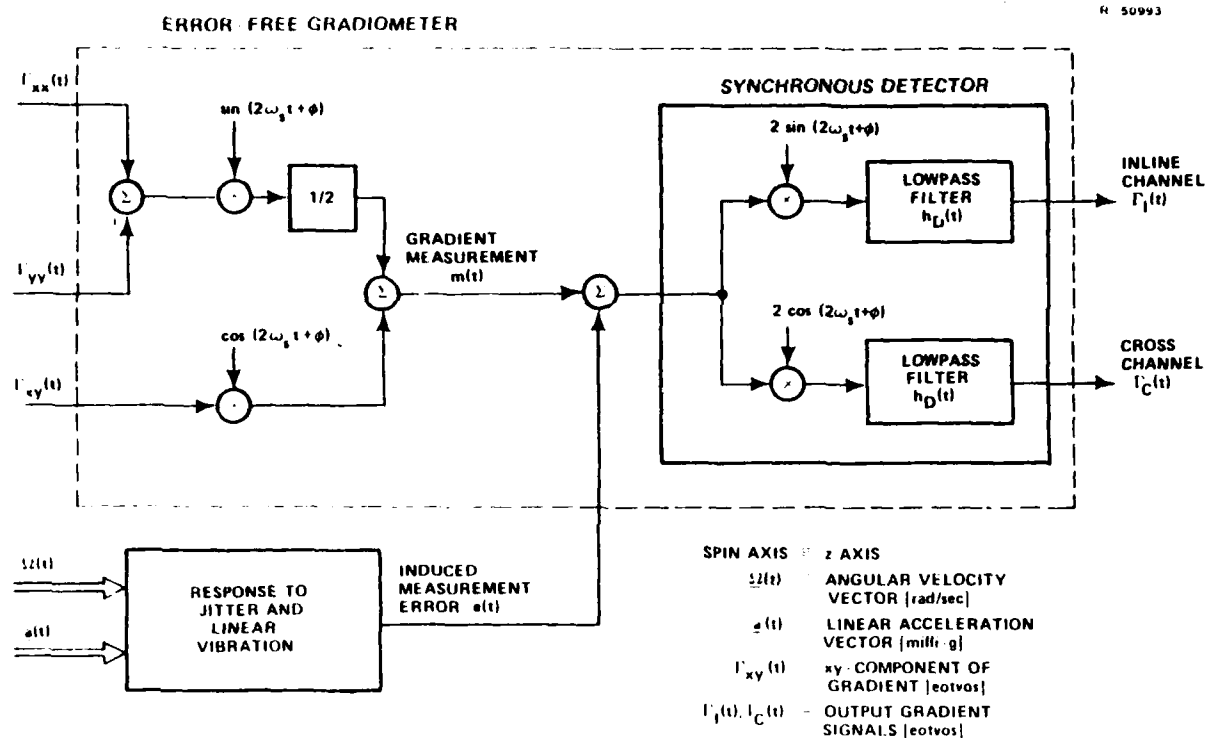
Figure 3.2-1   Time-Domain Input-Output Model for
Bell Gradiometer

As a result, the inline-channel output $\Gamma_I(t)$ and cross-channel output $\Gamma_C(t)$ of the error-free instrument are lowpass filtered versions of the input gravity gradient signals:

$$\Gamma_I(t) = h_D(t) * \frac{\Gamma_{yy}(t) - \Gamma_{xx}(t)}{2}$$

$$\Gamma_C(t) = h_D(t) * \Gamma_{xy}(t) \tag{3.2-1}$$

In these equations "$*$" denotes convolution, and $h_D(t)$ is the impulse response of the lowpass filters in the detector. In the GGI these are fourth-order Butterworth filters with a cutoff frequency of 25 millihertz (mHz), which is nearly equal to the effective bandwidth of a 20-second moving-window averager.

50

Measurement errors induced by jitter and linear vibration of the gradiometer are also indicated in Fig. 3.2-1. The jitter is characterized by the angular velocity vector $\underline{\Omega}(t)$ measured in radian/second (rad/s), while $\underline{a}(t)$ is an acceleration vector that characterizes the linear vibration in milli-g (mg).[*] In studies of airborne gravity surveys, $\underline{\Omega}(t)$ and $\underline{a}(t)$ represent the vibration environment of the gradiometer. Normall $\underline{\Omega}(t)$ is expected to be dominated by jitter in the inertial platform that supports the gradiometer, and $\underline{a}(t)$ is primarily driven by the structural vibrations and low-frequency motions of the aircraft.

A model for the vibration-induced measurement errors is shown in Fig. 3.2-2. The measurement error e(t) is modeled as the sum of three signals:

- **Linear jitter error**, caused by rotational vibrations near harmonics of the spin frequency. The gradiometer output error is proportional to the angular velocity of the jitter.

- **Quadratic jitter error**, caused by centripetal gradients due to rotational vibrations about axes normal to the spin axis. The gradiometer output error is proportional to the square of the angular velocity of the jitter.

- **Linear-vibration error**, caused by linear (translational) vibrations near harmonics of the spin frequency. The gradiometer output error is proportional to the linear acceleration.

In Fig. 3.2-2 the linear jitter and vibration sensitivities of the gradiometer are modeled by the two matrix gains G_{LJ} and G_{LV}. If the gradiometer were free of linear

---

[*]$1 \text{ g} = 9.81 \text{ m/s}^2$.

51
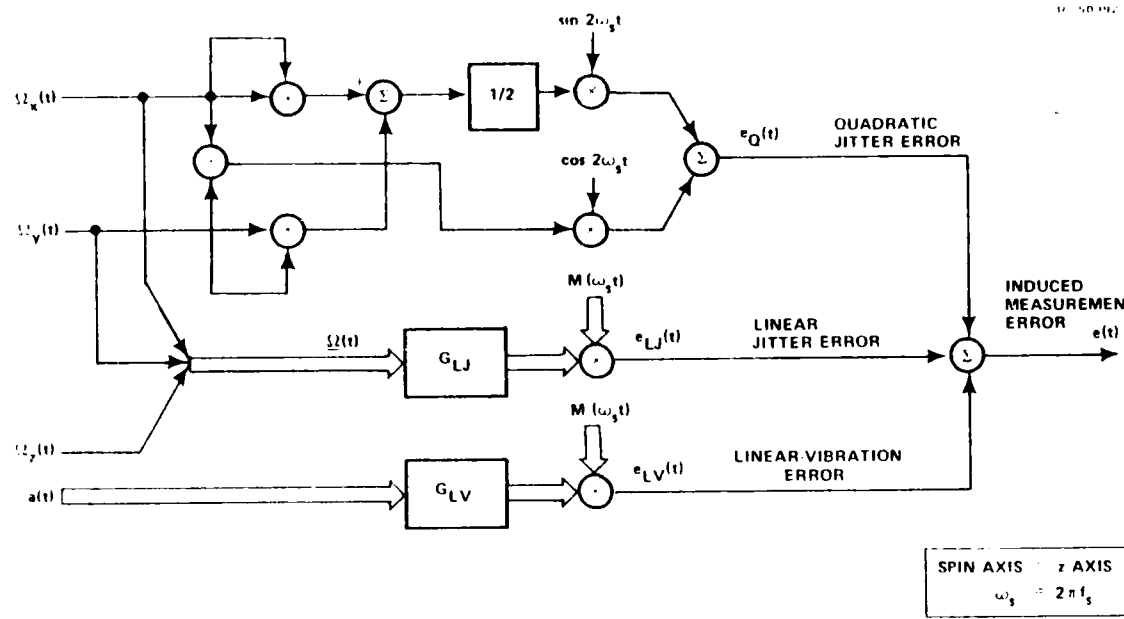
Figure 3.2-2   Input-Output Model for Vibration-Induced
                Measurement Error

jitter and vibration errors, these gain matrices would be
filled with zeros, and the induced measurement error e(t)
would equal only the quadratic jitter error $e_Q(t)$.

The linear jitter error $e_{LJ}(t)$ is a linear combina-
tion of the angular velocities in the jitter vector $\underline{\Omega}(t)$:

$$e_{LJ}(t) = \underline{M}^T(\omega_s t)\ G_{LJ}\ \underline{\Omega}(t) \qquad (3.2-2)$$

where $\omega_s = 2\pi f_s$, G_{LJ} is the matrix of gains that model the
gradiometer's linear sensitivity to jitter, and $\underline{M}^T(\omega_s t)$ is the
transpose of the modulation vector

52

$$
\underline{M}(\omega_s t) = \begin{bmatrix} 1 \\ \sin(\omega_s t + \phi) \\ \cos(\omega_s t + \phi) \\ \sin(2\omega_s t + \phi) \\ \cos(2\omega_s t + \phi) \end{bmatrix} \qquad (3.2\text{-}3)
$$

This modulation vector contains inphase and quadrature harmonics of the gradiometer spin, through order 2. The physical basis of this model for linear jitter error has been documented in Bell technical reports (Refs. 3 and 26). For the purposes of characterizing input-output behavior, specific physical interpretations of the individual elements of G_{LJ}, G_{LV}, and $\underline{M}(\omega_s t)$ are not required. The net effect on the performance of the gradiometer is that certain components of the jitter and vibration are modulated by the spin-frequency harmonics because the accelerometers in the gradiometer are attached to an instrument block that rotates at the spin frequency f_s.

An equation of identical form describes the linear-vibration error:

$$
e_{LV}(t) = \underline{M}^T(\omega_s t) \, G_{LV} \, \underline{a}(t) \qquad (3.2\text{-}4)
$$

In this equation, $\underline{a}(t)$ is the vibration vector of linear accelerations and G_{LV} is the matrix of gains that model the gradiometer's sensitivity to linear vibration.

The scalar output $e(t)$ of the error model in Fig. 3.2-2 generally has a broadband spectrum, but only the spectral components of $e(t)$ that lie within 24 mHz of $2f_s$ (twice the gradiometer spin frequency) contribute significant errors to the

outputs of the synchronous detector. This frequency selectivity is characteristic of narrowband AM modulation and demodulation. The selectivity implies that the input-output behavior of the error model can be identified from laboratory data obtained by shaking and rotating the gradiometer with sinusoidal test signals having frequencies equal to f_s and its first four harmonics. Bell performed such experiments in accordance with formal test procedures (Refs. 5 and 8). A method for using these vibration test data to characterize the output of the error model for random inputs, such as the vibration environments in airborne gravity surveys, is described in the next two sections.

3.3 ERRORS INDUCED BY LINEAR VIBRATIONS

3.3.1 Interpretation of Bell Test Data

The Bell tests for linear-vibration sensitivity are discussed first. During these experiments the gradiometer in both spin-axis-horizontal (SAH) and spin-axis-vertical (SAV) orientations was subjected to linear vibrations along specified directions. The *linear-acceleration vector*, therefore, ideally had the form

$$\underline{a}(t) = a_p \cos (2\pi f_a t + \theta) \, \hat{a} \qquad (3.3-1)$$

where

f_a is the frequency in hertz

a_p is the peak acceleration in milli-g

$\hat{a}$ is the unit vector that defines the direction of vibration (along one of the principal axes of the gradiometer)

θ is the phase angle in radians

54

The vibration frequency f_a was chosen to equal different low-order harmonics of the gradiometer spin frequency f_s. In accordance with the error model, the resulting steady-state outputs of the detector for $f_a = f_s$, $2f_s$, $3f_s$, and $4f_s$ can be shown to be of the form

$$\Gamma_I(t) = \text{constant} = C \cos (\psi)$$
$$\Gamma_C(t) = \text{constant} = \pm C \sin (\psi)$$

$$(3.3\text{-}2)$$

where C and ψ are real numbers. The phase angle ψ depends on the phase θ of the applied vibrations, which was held fixed for each frequency used in the experiment.

The root-mean-square (rms) values of the two output signals are equal to each other when the average is over all equally probable values for the two phase angles θ and ϕ of the linear vibration and the gradiometer spin:

$$[\Gamma_I(t)]_{rms} = [\Gamma_C(t)]_{rms} = \Gamma_{rms} \qquad (3.3\text{-}3)$$

where

$$\Gamma_{rms} = |C|/\sqrt{2} \qquad (3.3\text{-}4)$$

A per-channel rms sensitivity to linear vibration, denoted $S_{LIN}(\hat{a}, f_a)$, can be defined for each vibration direction $\hat{a}$ and frequency f_a:

$$S_{LIN}(\hat{a}, f_a) = \frac{\partial \Gamma_{rms}}{\partial a_{rms}} \qquad (3.3\text{-}5)$$

where the rms acceleration is

$$a_{rms} = a_p/\sqrt{2} \qquad (3.3\text{-}6)$$

Numerical values for these sensitivities were computed from the Bell test data by fitting least-squares straight lines to estimate the slopes $\partial\Gamma_I(t)/\partial a_p$ and $\partial\Gamma_C(t)/\partial a_p$. The sensitivities were then computed as

$$S_{LIN}(\hat{a},f_a) = \sqrt{\left(\frac{\partial\Gamma_I(t)}{\partial a_p}\right)^2 + \left(\frac{\partial\Gamma_C(t)}{\partial a_p}\right)^2} \bigg/ \sqrt{2} \qquad (3.3-7)$$

$S_{LIN}(\hat{a},f_a)$ is the gain with which the gradiometer demodulates (heterodynes) the input accelerations near frequency $\hat{f}_a$ to produce low-frequency errors in the output of the detector. The significance of this sensitivity for random acceleration disturbances is described next. It will be s wn that random accelerations, such as occur in airborne gravi ' surveys, cause white-noise errors in the gradiometer ; outputs.

3.3.2 Model for Errors Induced by Random Linear Acceleration

Let the acceleration vector $\underline{a}(t)$ be a random process of the form

$$\underline{a}(t) = a(t)\, \hat{a} \qquad (3.3-8)$$

where

$\hat{a}$ is a fixed unit vector specifying the direction of the acceleration

$a(t)$ is a stationary random scalar process with power spectrum

$$S_{aa}(f) = \int_{-\infty}^{\infty} R_{aa}(t)\, e^{-i2\pi ft}\, dt \qquad (3.3-9)$$

$R_{aa}(\tau)$ is the autocorrelation function of $a(t)$

$$R_{aa}(\tau) = E[a(t+\tau)a(t)] \qquad (3.3-10)$$

Also let the phase angle ϕ of the gradiometer spin be a random variable, uniformly distributed on the interval $(0, 2\pi)$.

The random acceleration $\underline{a}(t)$ induces low-frequency random error outputs from the synchronous detector. According to the error model, the power spectrum of the error signal at the output of the inline channel is the same as the error spectrum for the cross-channel output and is denoted $S_{\Gamma\Gamma}(f)$. This spectrum is the sum of heterodyned versions of the acceleration spectrum, weighted by the squared sensitivity coefficients for each spin-frequency harmonic and weighted also by the squared frequency response of the output filter.

$$S_{\Gamma\Gamma}(f) = \left| \frac{H_D(f)}{H_D(0)} \right|^2 \sum_{n=0}^{4} S_{LIN}^2(\hat{a}, f_n) \; [S_{aa}(f-f_n) + S_{aa}(f+f_n)]$$

(3.3-11)

where $f_n = n f_s = n^{th}$ harmonic of the spin frequency, and $H_D(f)$ is the Fourier transform of $h_D(t)$.

The pass band of the detection filter $H_D(f)$ is only 24 mHz, which is much smaller than the harmonics f_n of the spin frequency. Therefore, as long as the shifted spectra $S_{aa}(f \pm f_n)$ are free of resonances in the band $|f| \leq 24$ mHz, the expression for the output error spectrum can be approximated as

$$S_{\Gamma\Gamma}(f) \cong \left| \frac{H_D(f)}{H_D(0)} \right|^2 \; 2 \sum_{n=0}^{4} S_{LIN}^2(\hat{a}, f_n) \; S_{aa}(f_n)$$

(3.3-12)

which simply represents white noise in the output bandwidth. This means that the errors induced by random linear vibrations are equivalent to an increase in the white-noise level of the gradiometer's self noise.

57

The analysis is extended to 3-dimensional anisotropic random accelerations as follows. Assume that the acceleration vector

$$\underline{a}(t) = a_x(t)\hat{x} + a_y(t)\hat{y} + a_z(t)\hat{z} \qquad (3.3\text{-}13)$$

where $a_x(t)$, $a_y(t)$, and $a_z(t)$ are uncorrelated zero-mean stationary random processes that have the power spectra $S_{xx}(f)$, $S_{yy}(f)$, and $S_{zz}(f)$, and $\hat{x}$, $\hat{y}$, $\hat{z}$ are unit vectors pointing along the principal axes of the gradiometer. Then the white noise induced in the two detector outputs both have the same power spectrum:

$$S_{\Gamma\Gamma}(f) \cong \left| \frac{H_D(f)}{H_D(0)} \right|^2 2 \sum_{n=0}^{4} |S_{xx}(f_n)\, S^2_{LIN}(\hat{x}, f_n)$$

$$+ S_{yy}(f_n)\, S^2_{LIN}(\hat{y}, f_n) + S_{zz}(f_n)\, S^2_{LIN}(\hat{z}, f_n)|$$

$$(3.3\text{-}14)$$

The value of the sensitivity $S_{LIN}(\hat{a}, f_a)$ depends on the matrix gain G_{LV} in the error model. Fortunately, each element of G_{LV} does not have to be known for the purposes of estimating output errors due to stationary random inputs; the available test data are sufficient for developing a full 3-dimensional error model. However, such a model is based on the assumption that the gradiometer sensitivity to linear vibration is isotropic about the spin axis. This assumption is appropriate because practical limitations of the test stand used in the Bell tests made it impossible to apply vertically-directed accelerations to the gradiometer.

3.3.3 Estimated Linear Vibration Sensitivities

A set of estimated linear vibration sensitivities for the GGI is listed in Table 3.3-1. (Data were not available for sensitivities at the 4th spin-frequency harmonic.) Sensitivities at higher frequencies were expected to be small compared to the sensitivities in Table 3.3-1. This was verified by test data taken at 4 Hz, 8 Hz, and 16 Hz. However, at 30 Hz an unexplained larger sensitivity of 5 E/mg was observed for the SAH orientation when the vibration was normal to the spin axis. This anomaly is attributed by Bell to a structural resonance in the test stand or the structure of the gradiometer instrument. With regard to future testing of ball-bearing gradiometers, this suggests that the fundamental vibration modes of the test stand (and their possible interaction with the gradiometer) be identified to permit the clearest practical understanding of gradiometer vibration sensitivities.

TABLE 3.3-1
ESTIMATED LINEAR VIBRATION SENSITIVITIES
FOR BELL GGI NO. 1

SPIN AXIS ORIENTATION	VIBRATION DIRECTION WITH RESPECT TO SPIN AXIS	LINEAR VIBRATION SENSITIVITY (E/mg) VIBRATION FREQUENCY (f_s = SPIN FREQUENCY ~ 0.28 Hz)			
		0	f_s	$2f_s$	$3f_s$
Horizontal (SAH)	Parallel	$0.26^{\dagger}$	0.13	0.79	1.68
	Normal	$0.46^{\dagger}$	0.081	0.57	1.17
Vertical (SAV)	Normal	$0.46^{\dagger}$	4.30	0.049	4.40
	Parallel	$0.26^{\dagger}$	0.13^{*}	0.79^{*}	1.68^{*}

*Not available due to test geometry limitations - modeled consistently with SAH response.

$\dagger$From tilt test data on static g sensitivity.

3.4   ERRORS INDUCED BY ANGULAR VIBRATIONS

3.4.1   Interpretation of Bell Test Data

Bell conducted formal tests (Refs. 8, 27) to measure the angular vibration sensitivity of their baseline GGI.   For this purpose sinusoidal angular vibrations (jitter) were applied about the principal axes of the gradiometer, and the resulting error signals at the detector outputs were measured. These data can be interpreted with the help of the error model in Fig. 3.2-2 by expressing the angular-velocity vector $\underline{\Omega}(t)$ in the form

$$\underline{\Omega}(t) = \Omega_p \cos(2\pi f_a t + \theta)\underline{\Omega}$$ (3.4-1)

where Ω_p is the peak angular velocity in radians per second, f_a is the frequency in hertz, θ is the phase angle in radians, and $\underline{\Omega}$ is a unit vector pointing along the fixed axis of the applied rotation.   The x,y,z components of this velocity vector have the peak values

$$\Omega_{px} = \Omega_p\underline{\Omega}\cdot\hat{x}$$
$$\Omega_{py} = \Omega_p\underline{\Omega}\cdot\hat{y}$$ (3.4-2)
$$\Omega_{pz} = \Omega_p\underline{\Omega}\cdot\hat{z}$$

where $\hat{x}$, $\hat{y}$, $\hat{z}$ are unit vectors parallel to the x, y, and z axes.   (The z axis is chosen to coincide with the gradiometer spin axis.)   In the formal tests considered here, Ω was pointed along principal axes of the gradiometer, f_a was a harmonic of the gradiometer spin frequency f_s, and θ was a constant phase angle for each choice of f_a.

The error model includes both quadratic and linear errors that are induced by the jitter. The linear measurement error $e_{LJ}(t)$ is computed first, in the same way the linear vibration error $e_{LV}(t)$ was analyzed in the last section; the quadratic error $e_{QJ}(t)$, which is due to centripetal gradients, is analyzed in Section 3.4.3.

From Fig. 3.2-2, the jitter-induced linear measurement error is

$$e_{LJ}(t) = \underline{M}^T(\omega_s t) \ G_{LJ} \ \underline{\Omega}(t) \qquad (3.4-3)$$

The resulting steady-state error outputs of the detector are constants when f_a is a spin-frequency harmonic, and the rms values of these constants (averaged over all equally probable phase angles θ and ϕ) satisfy equations identical in form to those derived for linear vibrations in the previous section. Specifically,

$$[\Gamma_I(t)]_{rms} = [\Gamma_C(t)]_{rms} = \Gamma_{rms} \qquad (3.4-4)$$

where the value of Γ_{rms} depends on the jitter frequency f_a and the jitter axis $\hat{\Omega}$. A per-channel rms sensitivity to jitter can be defined in the same fashion as was done for linear vibration in Eq. 3.3-5:

$$S_{ANG}(\hat{\Omega}, f_a) = \frac{\partial \Gamma_{rms}}{\partial \Omega_{rms}} \qquad (3.4-5)$$

where the rms velocity is

$$\Omega_{rms} = \Omega_p / \sqrt{2} \qquad (3.4-6)$$

Numerical values for these angular sensitivities were computed from the Bell test data by fitting least-squares straight lines to estimate the slopes $\partial\Gamma_I(t)/\partial\Omega_p$ and $\partial\Gamma_C(t)/\partial\Omega_p$. The sensitivities were then computed as

$$S_{ANG}(\hat{\Omega},f_a) = \sqrt{\left(\frac{\partial\Gamma_I(t)}{\partial\Omega_p}\right)^2 + \left(\frac{\partial\Gamma_C(t)}{\partial\Omega_p}\right)^2} \Big/ \sqrt{2} \qquad (3.4\text{-}7)$$

3.4.2 Estimated Angular-Vibration Sensitivities

The angular sensitivities computed from the available test data are sufficient for developing a full 3-dimensional model for jitter-induced gradient measurement errors. In building this model it is assumed that the gradiometer's response to jitter is both isotropic about the spin axis and independent of spin axis orientation. These assumptions are appropriate because the design of Bell's test stand permitted application of rotations only about a horizontal axis. A full set of jitter sensitivities is shown in Table 3.4-1.

TABLE 3.4-1

ESTIMATED JITTER SENSITIVITES FOR BELL GGI NO. 1

SPIN AXIS ORIENTATION	VIBRATION DIRECTION WITH RESPECT TO SPIN AXIS	JITTER SENSITIVITIES (10^4 E/(rad/s))			
		f_s	$2f_s$	$3f_s$	$4f_s$
Horizontal (SAH)	Parallel	9.2	4.5	8.3	7.6
	Normal*	9.7	2.4	66	35
Vertical (SAV)	Parallel†	9.2	4.5	8.3	7.6
	Normal**	9.7	2.4	66	35

*Linear drift removed from raw data.

†Not available due to test geometry limitations - modeled consistently with SAH response.

**Data not available - modeled consistently with SAH response.

Some of the Bell data that were used to compute the sensitivities in Table 3.4-1 exhibited linear drift, which was subtracted from the data before estimating the sensitivities. Bell attributed this drift to the fact that resonance-hunting experiments preceded the jitter tests at spin-frequency harmonics. As a result, one of the error-correcting feedback loops in the gradiometer was over-loaded, and this loop had not recovered fully when the jitter tests were performed. The jitter data therefore exhibited drift corresponding to the transient response of the feedback loop. This drift would not occur during normal gradiometer operation.

3.4.3 Model for Errors Induced by Random Angular Velocities

The power spectra of errors caused by 3-dimensional stationary random jitter, which is used later to model aircraft vibrations during airborne gravity surveys, can be computed by using the same reasoning used in the previous section for linear vibration. The jitter vector is represented by

$$\underline{\Omega}(t) = \Omega_x(t)\hat{x} + \Omega_y(t)\hat{y} + \Omega_z(t)\hat{z} \tag{3.4-8}$$

where $\Omega_x(t)$, $\Omega_y(t)$, and $\Omega_z(t)$ are uncorrelated zero-mean stationary random processes that have the power spectra $S_{xx}(f)$, $S_{yy}(f)$, and $S_{zz}(f)$. Then the induced errors in the two detector outputs both have the same power spectrum:

$$S_{\Gamma\Gamma}(f) = \left| \frac{H_D(f)}{H_D(0)} \right|^2 2 \sum_{n=0}^{4} |S_{xx}(f_n)S_{ANG}^2(\hat{x}, f_n)$$

$$+ S_{yy}(f_n)S_{ANG}^2(\hat{y}, f_n) + S_{zz}(f_n)S_{ANG}^2(\hat{z}, f_n)|$$

$$\tag{3.4-9}$$

where $t_n = nt_s$. This is the sum of the contributions from the x, y, and z components taken separately.

The one remaining component of error in Fig. 3.2-2 is the quadratic jitter error $e_{QJ}(t)$ caused by centripetal gradients. This error source was negligible during the Bell tests conducted at spin-frequency harmonics and was therefore omitted in the preceding discussion. However, in other tests at high frequencies (4 Hz, 10 Hz, 20 Hz, 30 Hz, 40 Hz, and 50 Hz) the quadratic jitter error was the dominant error source.

According to Figs. 3.2-1 and 3.2-2, the inline and cross-channel outputs due to quadratic jitter error during these high-frequency tests are

$$\Gamma_I(t) = \frac{\Omega_{px}^2 - \Omega_{py}^2}{4} H_D(0)$$

$$\Gamma_C(t) = \frac{\Omega_{px}\Omega_{py}}{2} H_D(0)$$

(3.4-10)

where $H_D(0) = 10^9$ E/(rad/s)^2. The Bell data correspond to the case where $\Omega_{py}^2 >> \Omega_{px}^2 \approx 0$, which implies that

$$|\Gamma_I(t)| >> |\Gamma_C(t)| \cong 0$$
$$|\Gamma_I(t)| \leq \Omega_{py}^2 H_D(0)/4$$

(3.4-11)

These relations are verified by the Bell high-frequency test data. For example, in Fig. 3.4-1 the magnitude of the inline-channel output $\Gamma_I(t)$ for jitter normal to a vertical spin axis is plotted as a function of the peak angular velocity Ω_{py}. The dotted line is the upper bound for these data as predicted by Eq. 3.4.-11. The fact that the data are grouped
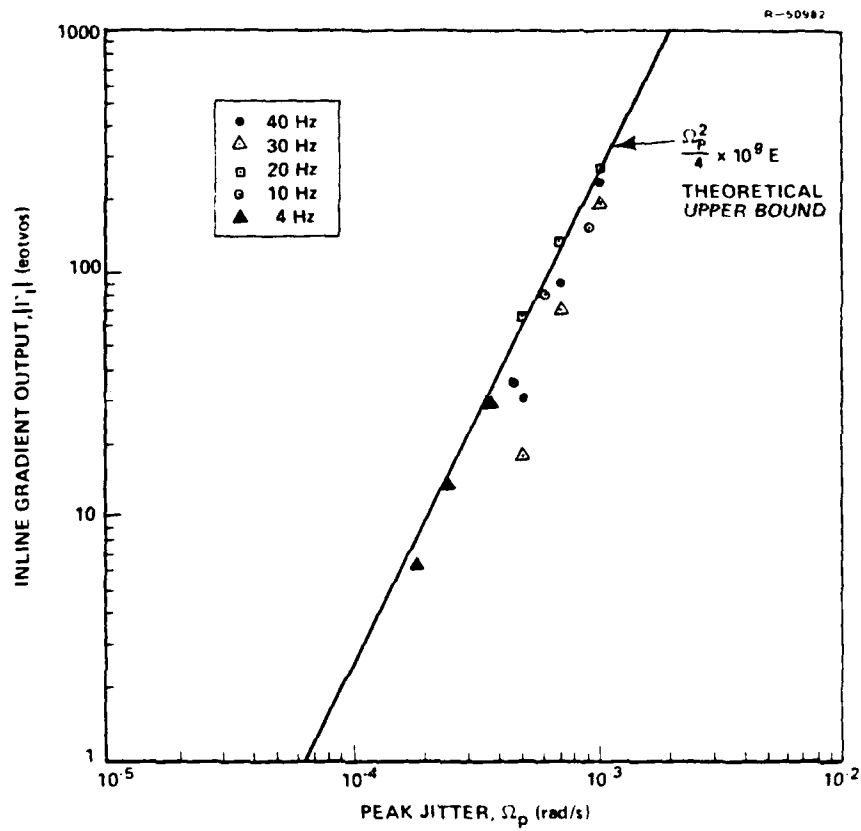
Figure 3.4-1   Bell Jitter Data (SAV, Bell Tape 22)

near and beneath this line indicates agreement with the error
model.   Figure 3.4-2 shows similar results for jitter normal
to a horizonal spin axis.

For gravity gradiometer survey simulations it is nec-
essary to compute the power spectrum of the gradient errors
caused by random quadratic jitter.   To do this the $\Omega_x(t)$ and
$\Omega_y(t)$ jitter components are modeled as independent jointly-
stationary zero-mean Gaussian random processes with power spec-
tra $S_{xx}(f)$ and $S_{yy}(f)$ and standard deviations σ_x and σ_y.   Ac-
cording to Fig. 3.2-2, the output error signals due to quad-
ratic jitter are accurately approximated by
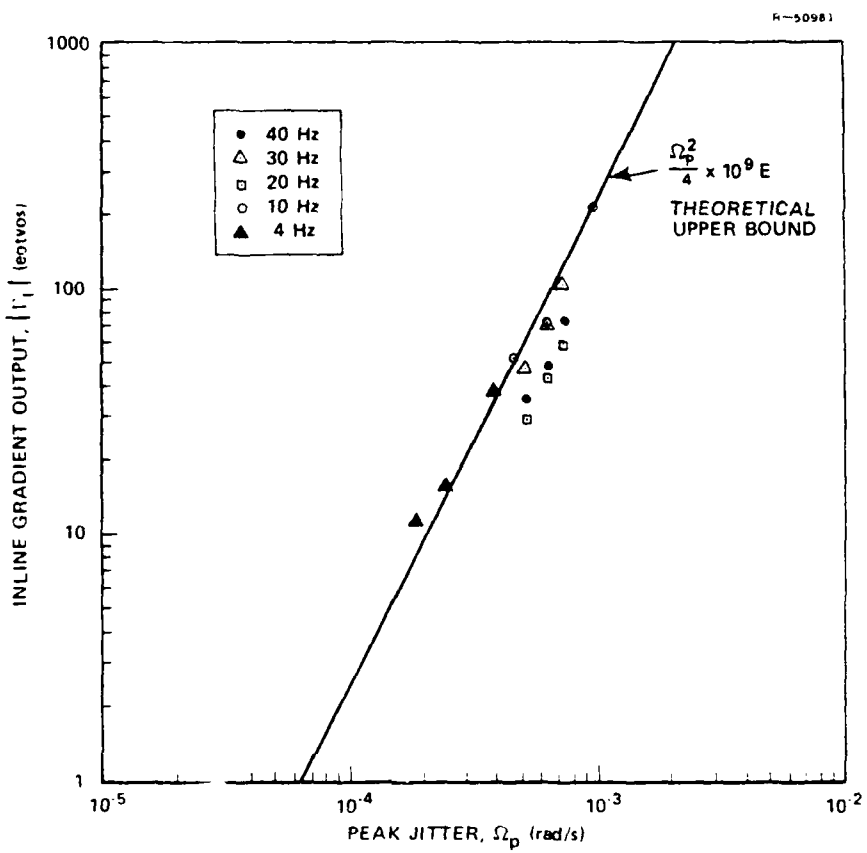
Figure 3.4-2   Bell Jitter Data (SAH, 16 November 1978 Data)

$$\Gamma_I(t) = \frac{\Omega_x^2(t) - \Omega_y^2(t)}{2} * h_D(t)$$

$$\Gamma_C(t) = [\Omega_x(t)\Omega_y(t)] * h_D(t) \tag{3.4-12}$$

If the power spectra of these processes are $S_{II}(f)$ and $S_{CC}(f)$ and their cross-spectrum is $S_{IC}(f)$, then

$$S_{II}(f) = H_D^2(0) [\sigma_x^2 - \sigma_y^2]^2 \delta(f)/4$$

$$+ \frac{S_{xx}(f)*S_{xx}(f) + S_{yy}(f)*S_{yy}(f)}{2} |H_D(f)|^2$$

$$\tag{3.4-13}$$

66

$$S_{CC}(f) = [S_{xx}(f) * S_{yy}(f)] \, |H_D(f)|^2$$

$$S_{IC}(f) = 0$$

$$H_D(0) = 10^9 \, E/(rad/s)^2$$

$$\delta(f) = \text{delta function}$$

The formulas for the autospectra can be simplified with a negligible loss in accuracy when the spectra $S_{xx}(f)$ and $S_{yy}(f)$ are analytic functions. The approximations are derived by expanding the integrands of the convolutions in powers of f and then retaining only the first terms. This procedure is appropriate when the lowpass filter $H_D(f)$ has a small bandwidth compared to the scale of the spectra $S_{xx}(f)$ and $S_{yy}(f)$. For example

$$S_{xx}(f) * S_{yy}(f) = \int_{-\infty}^{\infty} S_{xx}(f-f')S_{yy}(f')df'$$

$$= \int_{-\infty}^{\infty} S_{xx}(f'-f)S_{yy}(f')df'$$

$$= \int_{-\infty}^{\infty} [S_{xx}(f') - S_{xx}'(f')f + S_{xx}''(f')f^2/2 - \ldots]S_{yy}(f')df'$$

$$\cong \int_{-\infty}^{\infty} S_{xx}(f')S_{yy}(f')df' - f \int_{-\infty}^{\infty} S_{xx}'(f')S_{yy}(f')df' + 0(f^2)$$

$$(3.4-14)$$

where $0(f^2)$ denotes terms proportional to f^2 and higher powers of f. For f sufficiently small, only the first term is significant, and this is the term that is retained in the approximation. The resulting simplified formulas for inline and cross-channel error spectra are

$$S_{11}(f) \simeq H_D^2(0) \; [\sigma_x^2 - \sigma_y^2]^2 \delta(f)/4$$

$$+ \left| \frac{H_D(f)}{2} \right|^2 \int_{-\infty}^{\infty} [S_{xx}^2(f) + S_{yy}^2(f)] df \qquad (3.4\text{-}15)$$

$$S_{CC}(f) \cong |H_D(f)|^2 \int_{-\infty}^{\infty} S_{xx}(f) S_{yy}(f) df$$

These equations state that the quadratic jitter errors produce independent lowpass white-noise processes in the two output channels of the gradiometer.

These approximations are valid for jitter described by continuous power spectra, such as the broadband spectra used later in this report to model the vibration environment of the gradiometer in an airborne gravity survey. For narrowband jitter containing spectral delta functions, the above approximation is invalid. This case can actually arise in practice because the inertial platform that supports the gradiometer may have stiction, which is expected to result in narrowband spectral components at the resonance frequency of the platform and its harmonics. An analysis of platform jitter is given in Appendix A where its practical impact on gradiometer performance is discussed. It is concluded that uncompensated platform jitter could be a dominant error source in airborne surveys. However, compensation of the gradiometer outputs is feasible (via gyro measurements on the platform) to reduce the jitter errors to negligible levels. Such compensation has not yet been demonstrated by Bell.

3.5 MODELS FOR THE VIBRATION ENVIRONMENT OF AN AIRBORNE GRADIOMETER DURING GRAVITY SURVEYS

3.5.1 Introduction

In the previous sections it was shown that both linear and angular vibrations induce errors in the gradiometer output signals. These errors were shown to consist of biases plus white noise when the vibrations are stationary random processes. In Section 3.5.2 of this chapter, models are developed for random aircraft vibration. These models are based on available flight test data. Section 3.5.3 describes models for the passive isolation system and inertial platform that support the gradiometer in the aircraft.

3.5.2 Linear and Angular Aircraft Vibrations

Flight Test Data - A variety of flight test data on the linear and angular vibrations of military aircraft were evaluated for the purposes of modeling the vibration environment of a gradiometer during an airborne gravity survey. Ideally these data would provide power spectra for the x, y, and z components of both linear and angular vibrations at the location where the gradiometer system and its supporting hardware would be mounted. These spectra would ideally span the frequency range from 0.1 mHz to 1000 Hz and would correspond to typical survey flight conditions. The available test data that came closest to these ideals were in Ref. 2, which provides vibration power spectra for an NKC-135A aircraft in "moderate turbulence" at airspeeds ranging from 0.5 mach to 0.8 mach. The data are worst-case spectra obtained from two test flights. The altitude ranged from 5,000 feet to 37,000 feet, but was not uniquely specified in the test data. In addition the low-frequency limit of the power spectra was

approximately 0.1 Hz. These data were used to generate vibration models for survey simulations by fitting parametric spectrum models as explained in the following.

Vibration Models - The parametric vibration models were structured at low frequencies to extrapolate the test data down to zero frequency in the simplest possible way consistent with the physical constraint that the linear and angular displacements should have finite variances. The extrapolations provided constant spectral density values in the neighborhood of zero frequency for the linear-displacement and angular-displacement spectra. These extrapolations correspond to a low-frequency slope of 12 dB/octave in the linear acceleration spectrum and 6 dB/octave in the angular-velocity spectrum. Both the linear (vertical acceleration) and angular (pitch, roll, and yaw rates) test-data spectra had trends that could be modeled well by the following rational functions

$$S_{\Omega\Omega}^{A}(f) = 8 \times 10^{-4} \, K \, (f/0.2)^2 / [(f/0.2)^4 + 1] \; (\text{rad/s})^2/\text{Hz}$$

$$S_{aa}^{A}(f) = 4 \times 10^{-2} \, K \, (f/0.15)^4 / [(f/0.15)^4 + 1][(f/0.15)^2 + 1] \; g^2/\text{Hz}$$

$$K = 1/30^2 = \text{scale factor}$$

$$(3.5-1)$$

where $S_{\Omega\Omega}^{A}(f)$ and $S_{aa}^{A}(f)$ denote the spectra for the angular rates and linear accelerations. When the scale factor $K = 1$, these spectra model the flight test data corresponding to what is termed in Ref. 2 as worst-case "moderate turbulance." According to the model spectra, the linear vibration in the vertical direction then has an rms acceleration of 0.09 g, an rms velocity of 0.7 m/s, and an rms displacement of 1 m. Also for $K = 1$, the angular vibration about the pitch axis has an rms velocity of 1 deg/s and an rms rotation of 1 deg. These

70

are much larger than the vibration levels expected during a gravity survey; the scale factor value $K = 1/30^2$ reduces these rms levels by a factor of 30, which is believed to be a reasonable adjustment for survey modeling.

The model spectra are plotted together with the ensemble of available flight test data for comparison in Fig. 3.5-1 and 3.5-2. In these figures the quantities $2S_{\Omega\Omega}^{A}(f)$ and $2S_{aa}^{A}(f)$ (with $K = 1$) are plotted for easy comparison with the one-sided test-data spectra, which were measured with sensors at various locations on the aircraft.
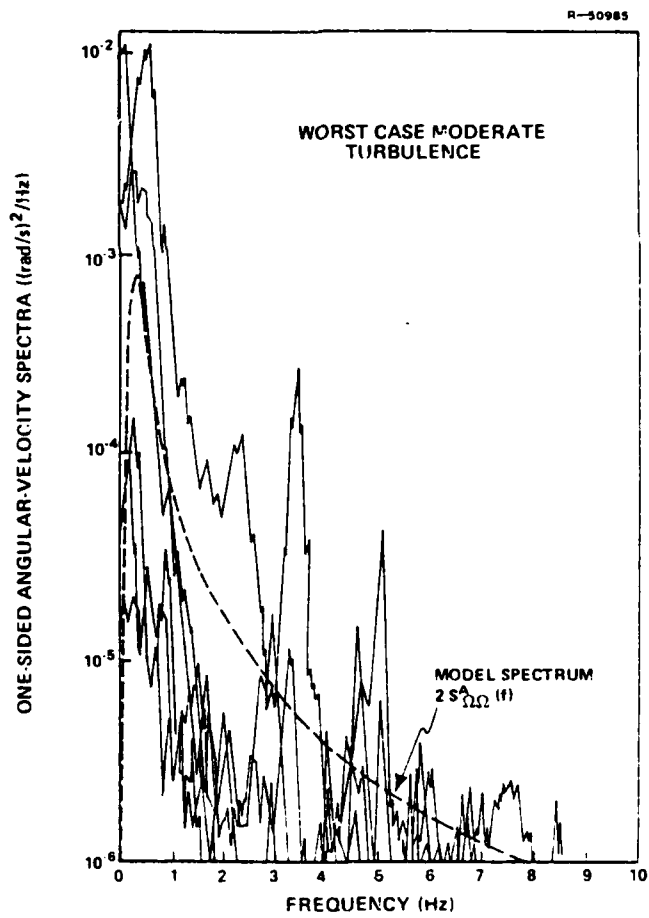
Figure 3.5-1   Ensemble of Flight Test Data for Pitch, Roll, and Yaw Rates and Model Spectrum
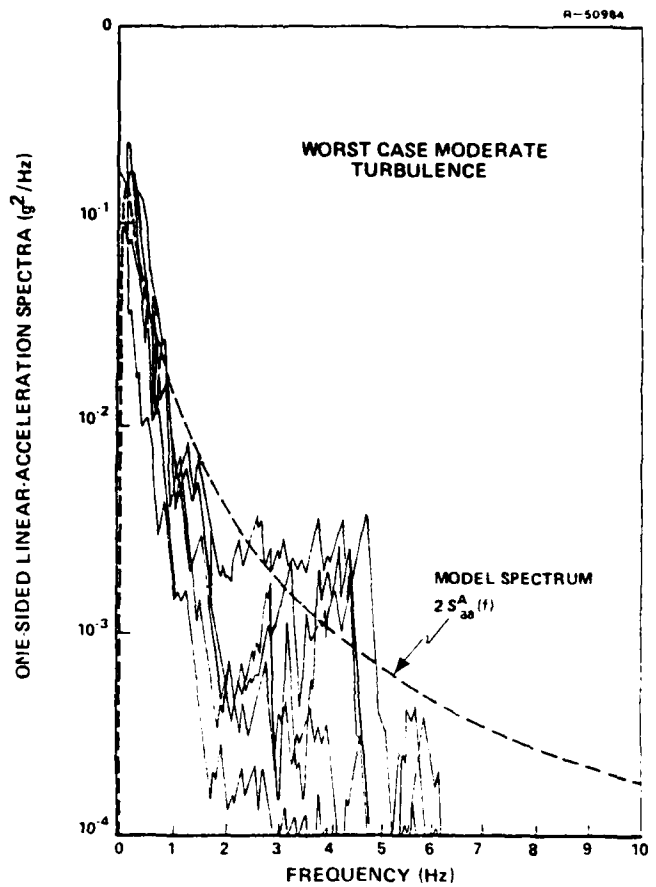
Figure 3.5-2   Ensemble of Flight Test Data for Vertical
Accelerations and Model Spectrum

These test data display a high degree of variability,
and they correspond to worst-case conditions during moderate
turbulance for a single aircraft. Furthermore, the data do
not include lateral and longitudinal linear accelerations.
Therefore, the vibration model is isotropic to allow a full
three-dimensional representation of the vibration environment.
That is, the pitch, roll, and yaw rates are independent random
processes, each having the power spectrum $S_{\Omega\Omega}^{A}(f)$, while the
linear accelerations along the vertical, lateral, and longitudi-
nal axes of the aircraft are also independent random processes,
each with the power spectrum $S_{aa}^{A}(f)$.

3.5.3 Gradiometer Isolation-System and Inertial-Platform Models

In projected airborne surveys the gradiometer is mounted on an inertial platform, which in turn is supported by a passive vibration isolation system attached to the airframe structure. Mechanical stability requirements put a practical lower limit of about 6 Hz on the natural frequencies of the passive isolator. For simplicity the 6 degrees of freedom (3 translational and 3 rotational) are modeled as uncoupled from each other, and the damping constant of the resonance for each mode is 0.25. The transfer function $T_{IS}(s)$ of such an isolator is

$$T_{IS}(s) = \frac{x_{out}(s)}{x_{in}(s)} = \frac{2\zeta_{IS}\omega_{IS}s + \omega^2_{IS}}{s^2 + 2\zeta_{IS}\omega_{IS}s + \omega^2_{IS}}$$

$$\zeta_{IS} = 0.25 \qquad\qquad (3.5-2)$$

$$\omega_{IS} = 2\pi 6 \text{ rad/s}$$

$$s = \text{complex frequency variable}$$

where $x_{out}(s)$ and $x_{in}(s)$ are the Laplace transforms of the output and input vibration quantity, which could be pitch, yaw, or roll rate, or vertical, lateral, or longitudinal linear acceleration. The magnitude of the frequency response of this transfer function, obtained by setting $s = i2\pi f$, is shown in Fig. 3.5-3.

The inertial platform provides isolation from angular vibrations and is described by a transfer function $T_{PI}(s)$ that relates input angular rates to the resulting output angular rates of the stabilized gradiometer with respect to an inertial reference:

73
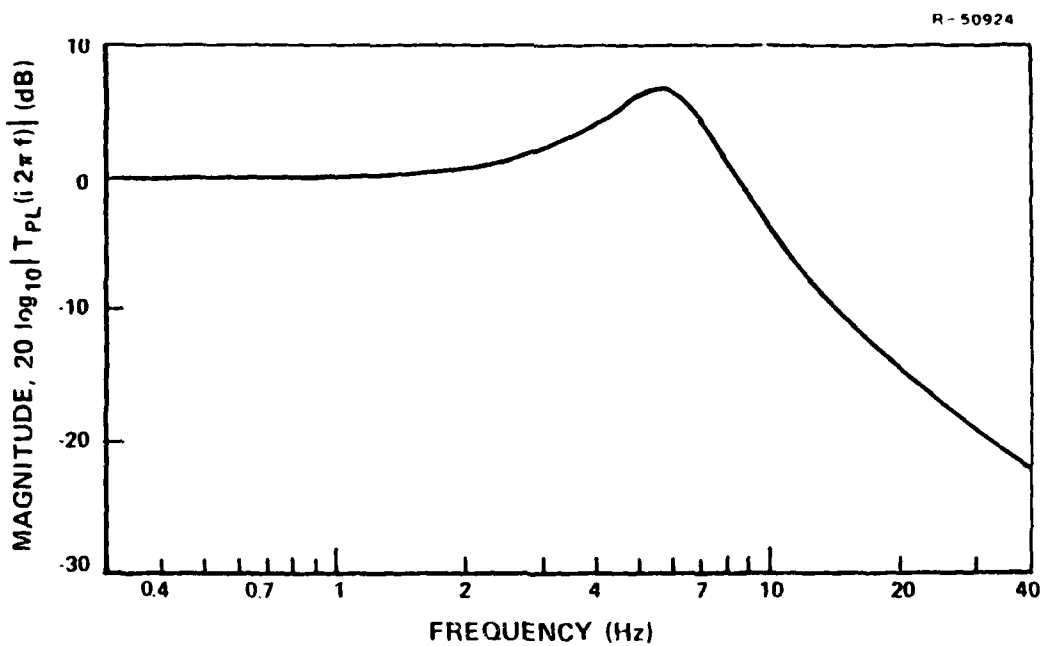
Figure 3.5-3   Magnitude of Transfer Function $T_{IS}(s)$
for Passive Isolator

$$T_{PL}(s) = K_{PL} \frac{2\zeta_{PL}\omega_{PL}s}{s^2 + 2\zeta_{PL}\omega_{PL}s + \omega_{PL}^2}$$

$\zeta_{PL} = 0.707$

$\omega_{PL} = 2\pi 20 \text{ rad/s}$ (3.5-3)

$K_{PL} = 3.16 \times 10^{-3}$

This model represents commonly used platform dynamics. At the damped 20 Hz resonance, it attenuates angular rates by a factor of 320 (50 decibels). The magnitude of the frequency response of this model is shown in Fig. 3.5-4.

R—50925
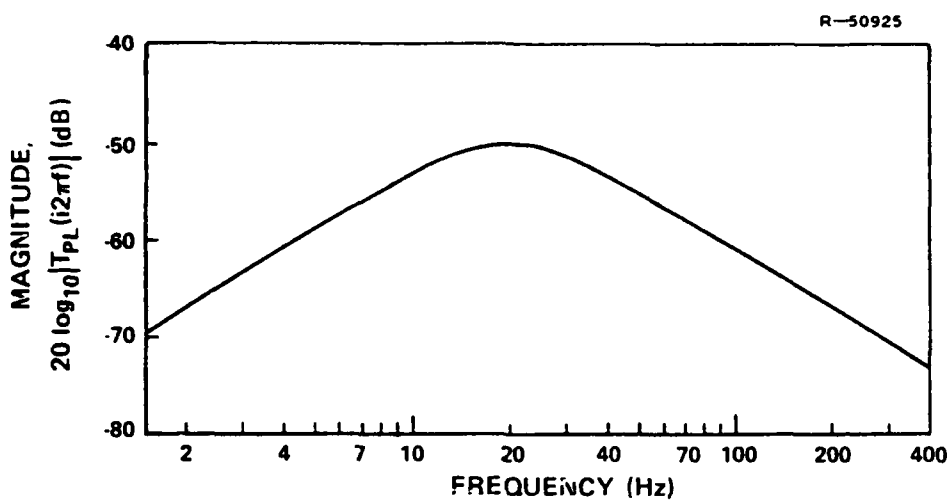
Figure 3.5-4   Magnitude of Transfer Function $T_{FP}(s)$
for Inertial Platform

3.6   ESTIMATED UPPER BOUNDS ON VIBRATION-INDUCED ERRORS
DURING AIRBORNE SURVEYS

3.6.1   Acceleration and Jitter Spectra

The models for the aircraft vibrations and the gradi-
ometer mounting system are now combined to yield power spectra
for modeling the vibration disturbances acting on a gradiometer
during an airborne survey. The vertical, lateral, and longi-
tudinal linear accelerations experienced by the gradiometer
each have the power spectrum

$$S_{aa}(f) = |T_{IS}(i2\pi f)|^2 \; S^A_{aa}(f) \qquad\qquad (3.6-1)$$

while the pitch, roll, and yaw rate spectra are

75

$$S_{\Omega\Omega}(f) = \left| T_{PL}(i2\pi f)T_{IS}(i2\pi f) \right|^2 S_{\Omega\Omega}^A(f) \qquad (3.6\text{-}2)$$

These vibration spectra are shown in Figs. 3.6-1 and 3.6-2. The critical spin-frequency harmonics of the gradiometer are indicated by the arrows in the 0.25 Hz to 1.0 Hz range. These are the frequencies at which the gradiometer exhibits linear vibration and linear jitter sensitivities.

3.6.2 A Bound on the RMS Error Due to Jitter

The practical significance of the jitter spectrum in Fig. 3.6-2 is discussed first. As previously explained in Section 3.4.3, jitter at any frequency induces error signals in the two gradiometer outputs. For the jitter model discussed here, which excludes stiction in the inertial platform, the inline and cross-channel error spectra due to quadratic jitter errors (centripetal gradients) are given by Eqs. 3.4-15 and 3.6-2 with $S_{xx}(f) = S_{yy}(f) = S_{\Omega\Omega}(f)$:

$$S_{II}(f) = 1.1 \times 10^{-10} \ E^2/Hz$$
$$S_{CC}(f) = 1.1 \times 10^{-10} \ E^2/Hz \qquad (3.6\text{-}3)$$
$$|f| < 0.24 \ Hz$$

The fluctuating white-noise component in each channel has an rms value of 2.3×10^{-6} E. These quadratic errors (due to aircraft jitter) are negligible because they are more than six orders of magnitude smaller than the rms errors due to the self noise of the gradiometer.

There are two remaining sources of jitter error: linear jitter sensitivity at spin-frequency harmonics, and
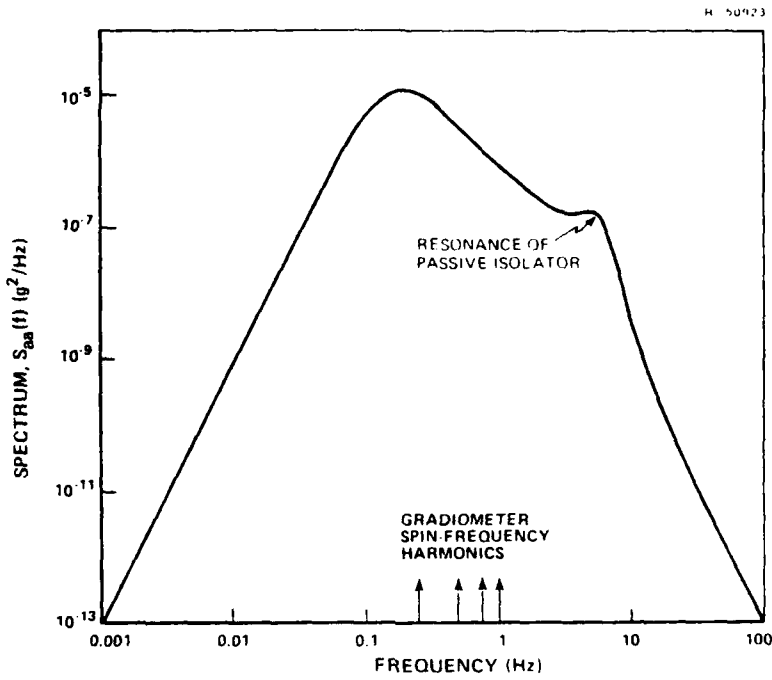
Figure 3.6-1   Estimated Power Spectrum of Vertical, Lateral or Longitudinal Acceleration Experienced by Airborne *Gradiometer*
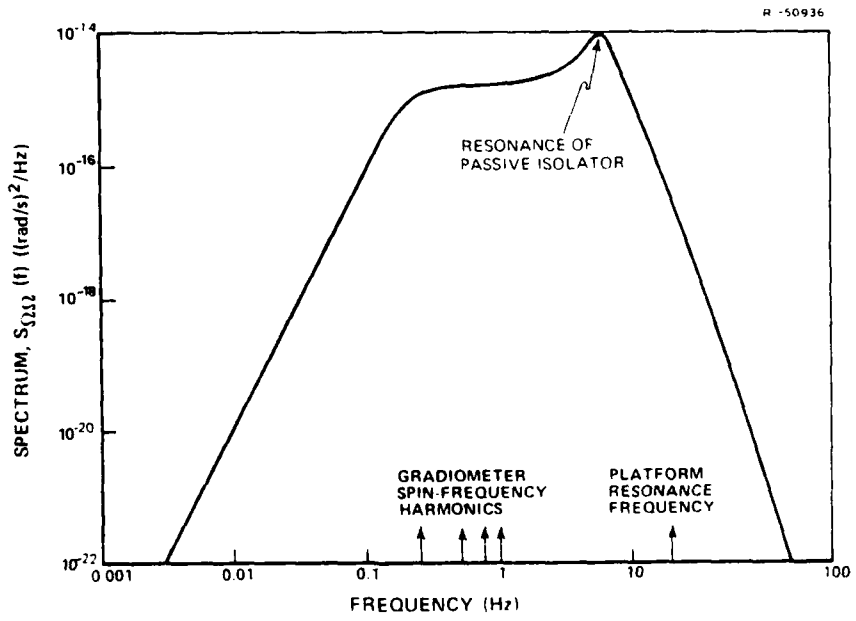
Figure 3.6-2   Estimated Power Spectrum for Pitch, Roll, or Yaw Rate Experienced by Airborne Gradiometer (No Platform Jitter)

77

quadratic sensitivity to stiction jitter in the inertial plat-
form. The rms gradient errors caused by linear sensitivity
can be estimated from the sensitivities listed in Table 3.4-1.
The largest sensitivity listed there is 6.6×10^5 E/(rad/s),
while the jitter spectrum in Fig. 3.6-2 has a value of about
3×10^{-15} (rad/s)^2/Hz at the spin-frequency harmonics. It then
follows from Eq. 3.4-9, with all sensitivities equal to 6.6×10^5
E/(rad/s) and all spectral densities set equal to 3×10^{-15} (rad/
s)^2/Hz, that the error spectrum in each of the two gradiometer
output channels is bounded for $|f| < 0.024$ Hz by

$$S_{\Gamma\Gamma}(f) < 0.04 \ E^2/Hz \qquad (3.6-4)$$

The corresponding rms error bound is 0.04 E. The
conclusion to be drawn from these calculations is that induced
errors due to linear jitter sensitivity are negligible compared
to the self noise of the gradiometer, which has an rms value
of 2 E.

Errors due to inertial-platform jitter are a poten-
tially significant source of error during gravity surveys.
Bell has proposed to measure the platform jitter with a gyro
and then continuously compute corrections to the gradiometer
outputs in real time. The feasibility of this jitter compen-
sation is discussed in Appendix A, where it is concluded that
Bell's approach to compensation is viable, but the magnitude
of the residual error depends on a number of questions that
can not be answered with the presently available data.

3.6.3 A Bound on the RMS Error Due to Linear Acceleration

The practical significance of the linear acceleration
spectrum in Fig. 3.6-1 is now estimated by calculations similar

to those used above for jitter. To compute an upper-bound for the errors due to linear accelerations, the largest sensitivity in Table 3.3-1 (4.4 E/mg) is used, along with the worst-case acceleration value $S_{aa}(0.25) = 1\times10^{-5}$ g^2/Hz in Fig. 3.6-1; the upper bound on the error spectrum $S_{\Gamma\Gamma}(f)$ in each output channel of the gradiometer is then given by Eq. 3.3-14, with all spectral densities equal to $S_{aa}(0.25)$ and all sensitivities equal to 4.4 E/mg. The result is, for $|f| < 0.024$ Hz,

$$S_{\Gamma\Gamma}(f) < 5800 \; E^2/Hz \qquad (3.6-5)$$

The corresponding rms error bound is 17 E. This bounding value is eight times the rms error due to the gradiometer's self noise, which indicates that errors due to linear accelerations may be a significant error source in airborne gravity surveys.

3.7 ERROR MODEL FOR AN AIRBORNE SURVEY SYSTEM CONTAINING THREE BELL GRADIOMETERS

3.7.1 Introduction

In projected gradiometric gravity surveys, three gradiometers are to be used simultaneously to recover all five independent components of the gravity gradient. This section describes the error model for such an instrument triad consisting of three Bell GGI's.

3.7.2 Recovery of the Gravity Gradient from Gradiometer-System Outputs

Each of the three gradiometers comprising the instrument triad has two outputs: the inline-channel gradient meas-

urement $\Gamma_I(t)$ and the cross-channel measurement $\Gamma_C(t)$. These six output functions are arranged in a vector

$$\underline{\Gamma}_O(t) = \begin{bmatrix} \Gamma_I^1(t) \\ \Gamma_C^1(t) \\ \Gamma_I^2(t) \\ \Gamma_C^2(t) \\ \Gamma_I^3(t) \\ \Gamma_C^3(t) \end{bmatrix} \qquad (3.7-1)$$

where the superscripts indicate particular gradiometers in the triad, and the subscript on $\Gamma_O(t)$ indicates output signals.

If the gradiometer system were free of errors, then the six distinct components of the gravity gradient

$$\Gamma(t) = \begin{bmatrix} \Gamma_{xx}(t) \\ \Gamma_{xy}(t) \\ \Gamma_{xz}(t) \\ \Gamma_{yy}(t) \\ \Gamma_{yz}(t) \\ \Gamma_{zz}(t) \end{bmatrix} \qquad (3.7-2)$$

could be computed from the system output $\Gamma_O(t)$ as follows

$$\Gamma(t) = T_O \Gamma_O(t) \qquad (3.7-3)$$

where the transformation matrix is

80

$$T_o = \begin{bmatrix} -2/3 & 0 & -2/3 & 0 & 0 & 0 \\ 0 & 1 & 0 & 0 & 0 & 0 \\ 0 & 0 & 0 & 1 & 0 & 0 \\ 2/3 & 0 & 0 & 0 & -2/3 & 0 \\ 0 & 0 & 0 & 0 & 0 & 1 \\ 0 & 0 & 2/3 & 0 & 2/3 & 0 \end{bmatrix} \qquad (3.7\text{-}4)$$

and, e.g., $\Gamma_{xz} = \partial g_x/\partial z \equiv \partial g_z/\partial x$, with g_x and g_z being the x and z components of the gravity vector. This transformation is derived in Appendix C.2. It corresponds to an x, y, z rectangular coordinate system with the x-axis pointing east, the y axis pointing north, and the z axis pointing up. In addition, the first gradiometer in the instrument triad is assumed to have a vertical spin axis, the second gradiometer has a south-pointing axis, while the third instrument's axis points east. Strictly vertical and horizontal spin axes are assumed because the formal test data on the baseline GGI were obtained with the gradiometer in these two orientations.

The measurement described in Eq. 3.7-3 also applies to gradiometer triads in which the spin axes are inclined at 55° to the vertical. (Such an "umbrella" configuration is p...ed for the Gravity Sensor System now being designed by Bell.) In this case the elements of T_o in Eq. 3.7-4 are changed to reflect the geometry of the sensors. Equation 3.7-3 also applies to gradiometer triads consisting of Draper gradiometers; this simply requires a redefinition of the output vector $\Gamma_o(t)$ and appropriate choice of matrix T_o.

T_o is the transformation that maps ideal measurement vectors (error-free gradiometer output signals) into gradient

vectors that satisfy Laplace's equation for the gravity potential. Since T_O is a known matrix, it is sufficient to develop an error model for the gradiometer output vector $\underline{\Gamma}_O(t)$. The resulting errors induced in the gradient vector $\underline{\Gamma}(t)$ can then be computed from Eq. 3.7-3.[*]

3.7.3 Gradiometer-System Error Model

In discussing error models it is convenient to decompose the measurement vector $\underline{\Gamma}_O(t)$ into two component vectors

$$\underline{\Gamma}_O(t) = \underline{\Gamma}_{IM}(t) + \underline{\Gamma}_e(t) \tag{3.7-5}$$

where $\underline{\Gamma}_{IM}(t)$ is an error-free ideal measurement vector and $\underline{\Gamma}_e(t)$ is a vector containing the six error signals in the outputs of the gradiometer triad. The error model for simulating airborne gradiometric gravity surveys computes the spectral density matrix $S_{\Gamma_e \Gamma_e}(f)$ of these errors. The structure of the error model is shown in Fig. 3.7-1, where the errors caused by aircraft vibrations (linear accelerations and angular velocities) are modeled along with the self noise of the gradiometers.

3.7.4 Aircraft Linear Accelerations

In Fig. 3.7-1 the aircraft linear accelerations at the mounting site of the gradiometer are characterized by a vector

---

[*]It is recognized that Eq. 3.7-3 does not necessarily describe an optimal estimator for $\Gamma(t)$ when the measurements are noisy, but rather a convenient transformation for error-modeling purposes. References 23-25 address the estimation problem.
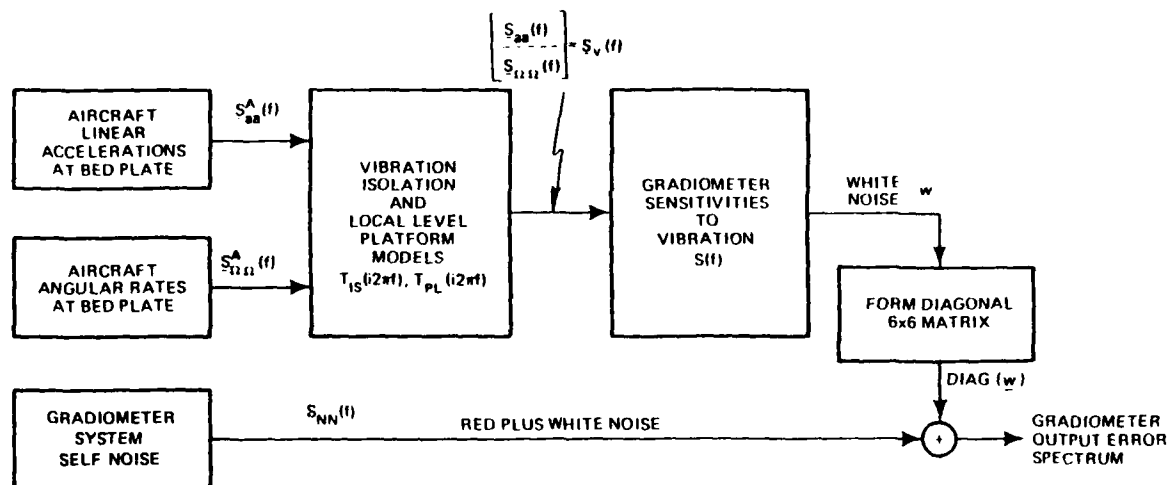
Figure 3.7-1   Airborne Gradiometric Survey Error Model

$$\underline{S}^A_{aa}(f) = \begin{bmatrix} S^A_{a_z a_z}(f) \\ S^A_{a_y a_y}(f) \\ S^A_{a_x a_x}(f) \end{bmatrix} \qquad (3.7-6)$$

whose elements are the power spectra of random accelerations in the z, y, and x directions. This ordering corresponds to up, across, and along track axes for a west-to-east flight path. In the error model developed in Section 3.5.2 these three components of acceleration are independent identical random processes with the spectral density $S^A_{aa}(f)$

$$S^A_{aa}(f) = \begin{bmatrix} S^A_{aa}(f) \\ S^A_{aa}(f) \\ S^A_{aa}(f) \end{bmatrix} \qquad (3.7-7)$$

where $S_{aa}^{A}(f)$ is given in equation 3.5-1.

3.7.5 Aircraft Angular Velocities

In similar fashion the aircraft angular rates at the gradiometer mounting site are represented by the vector

$$S_{\underline{\Omega}\Omega}^{A}(f) = \begin{bmatrix} S_{\Omega_y\Omega_y}^{A}(f) \\ S_{\Omega_x\Omega_x}^{A}(f) \\ S_{\Omega_z\Omega_z}^{A}(f) \end{bmatrix} \qquad (3.7\text{-}8)$$

whose elements are the power spectral densities of the angular velocities about the y, x, and z axes. This ordering corresponds respectively to pitch, roll, and yaw axes for a west-to-east flight path. These three components of velocity are modeled as independent indentical random processes with spectral density $S_{\Omega\Omega}^{A}(f)$

$$S_{\underline{\Omega}\Omega}^{A}(f) = \begin{bmatrix} S_{\Omega\Omega}^{A}(f) \\ S_{\Omega\Omega}^{A}(f) \\ S_{\Omega\Omega}^{A}(f) \end{bmatrix} \qquad (3.7\text{-}9)$$

where $S_{\Omega\Omega}^{A}(f)$ is given in Eq. 3.5-1.

3.7.6 Isolation System and Inertial Platform

The output of the vibration isolation and local-level platform models in Fig. 3.7-1 is the vibration vector

$$
\underline{S}_V(f) \quad = \quad \begin{bmatrix} \underline{S}_{aa}(f) \\ \hline \underline{S}_{\Omega\Omega}(f) \end{bmatrix} = \begin{bmatrix} S_{a_z a_z}(f) \\ S_{a_y a_y}(f) \\ S_{a_x a_x}(f) \\ \hline S_{\Omega_y \Omega_y}(f) \\ S_{\Omega_x \Omega_x}(f) \\ S_{\Omega_z \Omega_z}(f) \end{bmatrix} \qquad (3.7\text{-}10)
$$

which contains the x, y, and z components of both the linear acceleration and angular velocity experienced by the gradi-ometer instrument triad. From Eqs. 3.6-1 and 3.6-2 the vibration vector can be written out as

$$
\begin{bmatrix} \underline{S}_{aa}(f) \\ \hline \underline{S}_{\Omega\Omega}(f) \end{bmatrix} = \begin{bmatrix} |T_{IS}(i2\pi f)|^2 \; \underline{S}^A_{aa}(f) \\ \hline |T_{PL}(i2\pi f) \; T_{IS}(i2\pi f)|^2 \; \underline{S}^A_{\Omega\Omega}(f) \end{bmatrix} \qquad (3.7\text{-}11)
$$

where the transfer functions T_{PL} and T_{IS} of the inertial platform and passive isolation systems are given in Eqs. 3.5-2 and 3.5-3.

3.7.7 Gradiometer-System Vibration Sensitivities

The linear sensitivities of the gradiometer to vibration are represented in Fig. 3.7-1 by a 6 × 6 mean-square sensitivity matrix $S(f) = [S_{ij}(f)]$, whose ij^{th} element is the mean-square sensitivity of the ith output of the instrument triad to the jth element of the vibration vector $S_V(f)$. The output vector W of white-noise spectral densities is given (in accordance with Eq. 3.3-14) as

$$W = 2 \sum_{k=0}^{4} S(f_k)\underline{S}_V(f_k) \qquad (3.7\text{-}12)$$

where $f_k = kf_s$, for $k = 0,1,\ldots,4$ and $f_s = 0.28$ Hz, are the spin-frequency harmonics of the gradiometer.

In the coordinate system used for the gradiometer triad, the mean-square sensitivity matrix has the form

$$S(f_k) = \left[S_{LIN}(f_k) \ \vdots \ S_{ANG}(f_k) \right] \qquad (3.7\text{-}13)$$

where

$$S_{LIN}(f_k) = \begin{bmatrix} s^2_{LIN}(\|\,VSA,f_k) & s^2_{LIN}(\underline{\perp}VSA,f_k) & s^2_{LIN}(\underline{\perp}VSA,f_k) \\ s^2_{LIN}(\|\,VSA,f_k) & s^2_{LIN}(\underline{\perp}VSA,f_k) & s^2_{LIN}(\underline{\perp}VSA,f_k) \\ s^2_{LIN}(\underline{\perp}HSA,f_k) & s^2_{LIN}(\|\,HSA,f_k) & s^2_{LIN}(\underline{\perp}HSA,f_k) \\ s^2_{LIN}(\underline{\perp}HSA,f_k) & s^2_{LIN}(\|\,HSA,f_k) & s^2_{LIN}(\underline{\perp}HSA,f_k) \\ s^2_{LIN}(\underline{\perp}HSA,f_k) & s^2_{LIN}(\underline{\perp}HSA,f_k) & s^2_{LIN}(\|\,HSA,f_k) \\ s^2_{LIN}(\underline{\perp}HSA,f_k) & s^2_{LIN}(\underline{\perp}HSA,f_k) & s^2_{LIN}(\|\,HSA,f_k) \end{bmatrix}$$

$$(3.7\text{-}14)$$

$$S_{ANG}(f_k) = \begin{bmatrix} s^2_{ANG}(\underline{\perp}VSA,f_k) & s^2_{ANG}(\underline{\perp}VSA,f_k) & s^2_{ANG}(\|\,VSA,f_k) \\ s^2_{ANG}(\underline{\perp}VSA,f_k) & s^2_{ANG}(\underline{\perp}VSA,f_k) & s^2_{ANG}(\|\,VSA,f_k) \\ s^2_{ANG}(\|\,HSA,f_k) & s^2_{ANG}(\underline{\perp}HSA,f_k) & s^2_{ANG}(\underline{\perp}HSA,f_k) \\ s^2_{ANG}(\|\,HSA,f_k) & s^2_{ANG}(\underline{\perp}HSA,f_k) & s^2_{ANG}(\underline{\perp}HSA,f_k) \\ s^2_{ANG}(\underline{\perp}HSA,f_k) & s^2_{ANG}(\|\,HSA,f_k) & s^2_{ANG}(\underline{\perp}HSA,f_k) \\ s^2_{ANG}(\underline{\perp}HSA,f_k) & s^2_{ANG}(\|\,HSA,f_k) & s^2_{ANG}(\underline{\perp}HSA,f_k) \end{bmatrix}$$

$$(3.7\text{-}15)$$

in which S^2_{LIN} and S^2_{ANG} denote the squares of the rms linear
sensitivities defined in Sections 3.2.1 and 3.4.1, HSA and VSA
denote horizontal and vertical spin axes, and the symbols " $\parallel$ "
and " $\perp$ " respectively denote vibration axes that are parallel
and normal to the spin axes. The numerical values for the rms
sensitivities that have been estimated from available test data
and that are used in the TASC error model are listed in Tables
3.3-1 and 3.4-1. The values in these tables are expressed in
E/mg or 10^4 E/(rad/s) and must therefore be squared and scaled
properly to yield $S^2_{LIN}(f_k)$ in E^2/g^2 and $S^2_{ANG}(f_k)$ in $E^2/(rad/s)^2$
as shown in Appendix C.3.

The diagonal white-noise spectral density matrix DIAG($\underline{W}$)
is constructed from the six independent white-noise densities
in $\underline{W}$:

$$DIAG(\underline{W}) = \begin{bmatrix} W_1 & 0 & 0 & 0 & 0 & 0 \\ 0 & W_2 & 0 & 0 & 0 & 0 \\ 0 & 0 & W_3 & 0 & 0 & 0 \\ 0 & 0 & 0 & W_4 & 0 & 0 \\ 0 & 0 & 0 & 0 & W_5 & 0 \\ 0 & 0 & 0 & 0 & 0 & W_6 \end{bmatrix} \quad (3.7-16)$$

This diagonal form represents the independence of the vibration-
induced white noises in the six outputs of the gradiometer
triad.

Discussion of Omitted Terms - The current version of
the TASC error model for airborne gradiometric surveys omits
measurement errors caused by platform jitter. Active jitter
compensation is planned by Bell. Although not yet demonstrated
"on-line," preliminary tests indicate that such compensation

87

may be feasible. The analysis in Appendix A supports the concept. Of course, to demonstrate the practicality of jitter compensation requires that a compensation scheme be implemented and verified by laboratory tests. As such data become available they will be evaluated. If the magnitudes of the residual jitter errors are large enough, it will then be justified to include platform jitter in the TASC error model.

The analysis of quadratic sensitivity to aircraft jitter in Section 3.6.2 showed that the resulting rms measurement errors are expected to be more than six orders of magnitude smaller than the self noise of the gradiometer. For this reason, quadratic sensitivity to aircraft jitter is excluded from the error model.

3.7.8 Gradiometer Self Noise

The final error source in Fig. 3.7-1 is the gradiometer system self noise, which is represented by the spectral density matrix

$$
S_{NN}(f) = \begin{bmatrix} S_{NN}^1(f) & 0 & 0 \\ 0 & S_{NN}^2(f) & 0 \\ 0 & 0 & S_{NN}^3(f) \end{bmatrix} \qquad (3.7\text{-}17)
$$

where $S_{NN}^j(f)$, $j = 1,2,3$, is the spectral density matrix for the self noise in the two outputs of the jth gradiometer of the instrument triad. The self noises of separate gradiometers are independent of each other. The first gradiometer has a vertical spin axis, and its spectral density matrix is

$$
S_{NN}^1(f) = \begin{bmatrix} S_{II}^{VER}(f) & S_{IC}^{VER}(f) \\ S_{CI}^{VER}(f) & S_{CC}^{VER}(f) \end{bmatrix} \qquad (3.7\text{-}18)
$$

where, from the analysis in Sections 2.4.1 and 2.4.2, the spectral densities for the inline and cross-channel noises are

$$S_{II}^{VER}(f) = W_{SAV} + \frac{R_{SAV}}{f^2} \; , \; 0.01 \text{ mHz} < |f| < 24 \text{ mHz}$$

$$S_{IC}^{VER}(f) = S_{CI}^{VER}(f) = 0 \hspace{3cm} (3.7\text{-}19)$$

$$W_{SAV} = 81 \; E^2/Hz$$

$$R_{SAV} = 2.0 \times 10^{-6} \; E^2 \cdot Hz$$

In similar manner, the two horizontally oriented gradiometers have spectral density matrices

$$S_{NN}^2(f) = S_{NN}^3(f) \hspace{3cm} (3.7\text{-}20)$$

where

$$S_{NN}^2(f) = \begin{bmatrix} S_{II}^{HOR}(f) & S_{IC}^{HOR}(f) \\ S_{CI}^{HOR}(f) & S_{CC}^{HOR}(f) \end{bmatrix} \hspace{2cm} (3.7.8\text{-}5)$$

with

$$S_{II}^{HOR}(f) = W_{SAH} + \frac{R_{SAH}}{f^2} \; , \; 0.01 \text{ mHz} < |f| < 24 \text{ mHz}$$

$$S_{CC}^{HOR}(f) = S_{II}^{HOR}(f)$$

$$S_{IC}^{HOR}(f) = S_{CI}^{HOR}(f) = 0 \hspace{3cm} (3.7\text{-}22)$$

$$W_{SAH} = 86 \; E^2/Hz$$

$$R_{SAH} = 1.6 \times 10^{-5} \; E^2 \cdot Hz$$

All components of the gradiometer system error model have been defined. In the next chapter, this model is combined with models for other gravimetric sensors and used in simulations to demonstrate some typical results for airborne gradiometric surveys.

4. GRADIOMETRIC SURVEY SIMULATION RESULTS

4.1 INTRODUCTION

The TASC Multisensor Survey Simulation software uses models for the gravity field, survey geometries, and sensor errors to compute the rms errors inherent in statistically optimal recoveries of gravity quantities. A detailed description of the Simulation program and its capabilities, which include trajectory and impact error analyses, will be given in a forthcoming report (Ref. 25). This chapter describes typical simulation results obtained for airborne gradiometric surveys. A variety of gradiometer error models are used to illustrate the flexibility of the software and to indicate the usefulness of gradiometer error models for determining the sensitivity of recovery errors to gradiometer measurement errors.

The overall structure of the Survey Simulation is shown in Fig. 4.1-1 for the case in which airborne gradiometry is combined with either satellite altimetry or surface gravimetry to estimate the rms error in point estimates of the gravity disturbance vector. The gradiometer-system error model described in Section 3.7 is used[*] in this software to represent the self noise and sensitivities to mechanical vibration of the Bell GGI. In addition, preliminary error models for the Bell Ball-Bearing GGI and the Draper Floated Gravity

---

[*]The gradiometer bandwidth is set equal to 50 mHz to model a survey sampling rate of one measurement every 10 seconds.
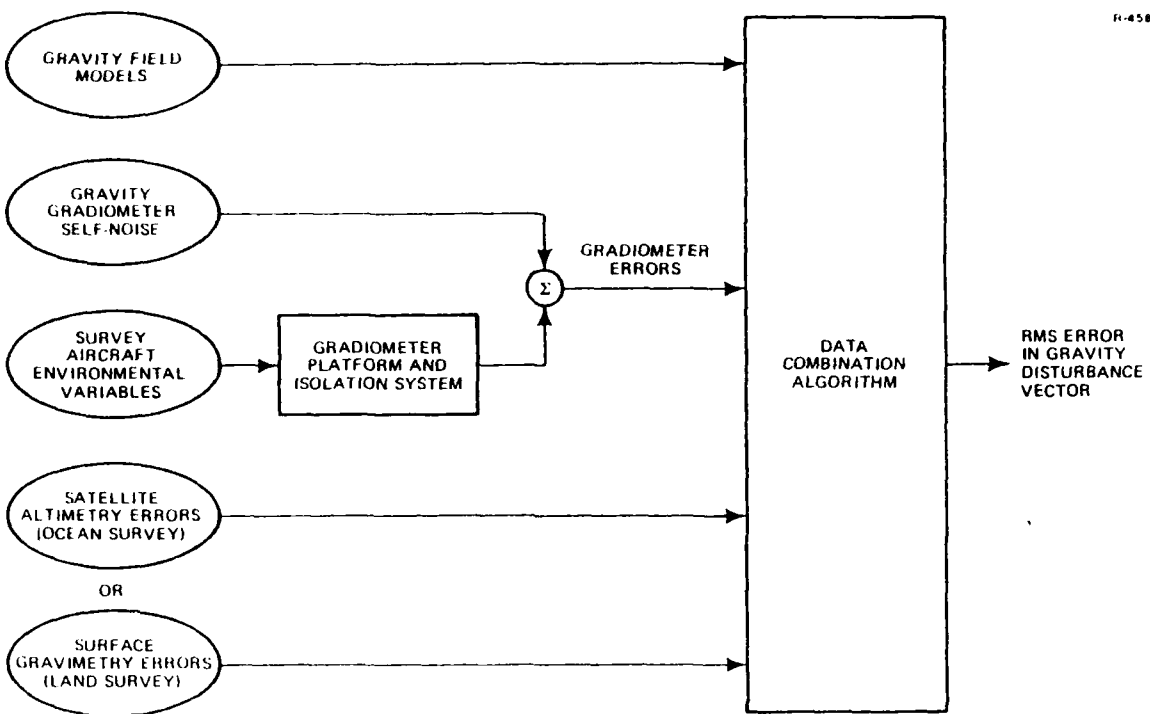
Figure 4.1-1   Structure of Multisensor Survey Simulation

Gradiometer are also included for comparison.   These prelimin-
ary error models are subject to revision when additional test
data are analyzed.

4.2   GRADIOMETER SURVEY GEOMETRY

The airborne gradiometer survey model covers a rec-
tangular area as shown in Fig. 4.2-1.   The survey aircraft has
a constant altitude of 6 km and flies along parallel east-west
tracks spaced 10 km.   The measurement spacing along a track is
1.5 km, which corresponds to one measurement every 10 seconds
at a speed of 300 kt.   Each track is 2780 km long (5 hour flight).

SURVEY GEOMETRY MODEL

- STRAIGHT LINE EAST   WEST TRACKS

- THREE AXIS INSTRUMENTATION

- TRACK SPACING: T   10 km

- MEASUREMENT SPACING   a   1 5 km
  (10 sec SAMPLING at 300 kt)

- HEIGHT OF SURVEY: h   20,000 ft

ERROR MODEL

- LOW FREQUENCY DRIFT CHARACTERISTICS

- WHITE NOISE FLOOR AT HIGH FREQUENCIES

- SAMPLING ERROR: ALIASING AND OMISSION AT HIGH FREQUENCIES

- FINITE TRACK LENGTH: WAVELENGTHS LONGER THAN 2780 km
  (5 hr flight) ASSUMED INACCURATE

Figure 4.2-1   Gradiometer Survey Geometry and Error Modeling

4.3   SURVEY MODELS FOR OTHER SENSORS

The satellite altimetry model used in the simulation is chosen to represent GEOS-3 survey data. The track geometry is shown in Fig. 4.3-1, together with numerical values for the track parameters. The error model for the altimetry is also described in this figure.

The gravimeter survey model is described in Fig. 4.3-2. Measurements are located on a grid of equally spaced points separated from each other by 150 nautical miles (nm) and extending sufficiently far beyond the gradiometer survey region to provide good long wavelength recovery. This spacing is adequate to recover the lower frequency components of the gravity field.

SURVEY GEOMETRY MODEL

INFINITE GRID OF ASCENDING AND DESCENDING
STRAIGHT LINE TRACKS

- TRACK SPACING (EQUATORIAL CROSSINGS):
    $T = 55.6$ km

- MEASUREMENT SPACING (INTENSIVE MODE):
    $s = 663$ m

- ORBIT INCLINATION (AT EQUATOR):
    $\theta = 65°$
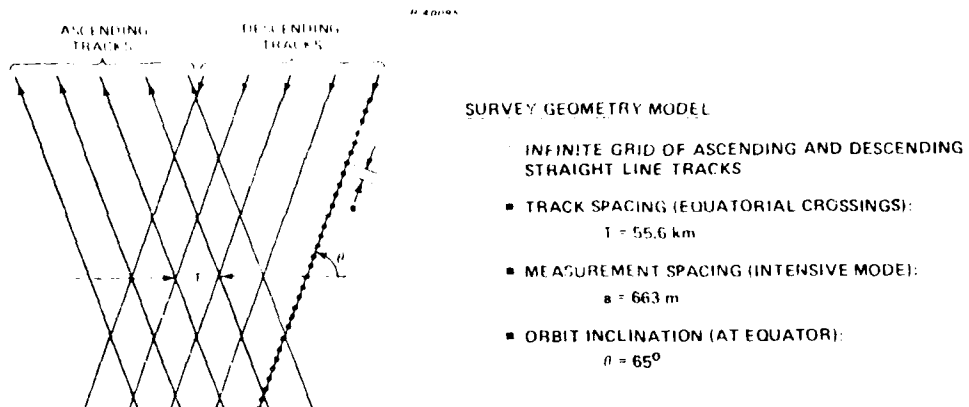
ERROR MODEL

- BIAS, ORBIT, TIDE CORRECTION ERRORS: 50 CM RMS (POST ADJUSTMENT)

- OCEAN CURRENT DYNAMIC HEIGHT (UNCORRECTED): 60 CM RMS, 122 km CORRELATION DISTANCE

- INSTRUMENT NOISE AND SEA STATE: 60 CM RMS UNCORRELATED

- SAMPLING ERROR: ALIASING AND OMISSION AT HIGH FREQUENCIES

Figure 4.3-1   Satellite Altimeter Survey Geometry and
Error Modeling (GEOS-3 Parameters)

SURVEY GEOMETRY MODEL

- GRID OF EQUISPACED MEASUREMENTS

- $d = 150$ km

ERROR MODEL

- MEASUREMENT ERROR: 3 mgal RMS UNCORRELATED

- SAMPLING ERROR: ALIASING AND OMISSION AT
HIGH FREQUENCIES
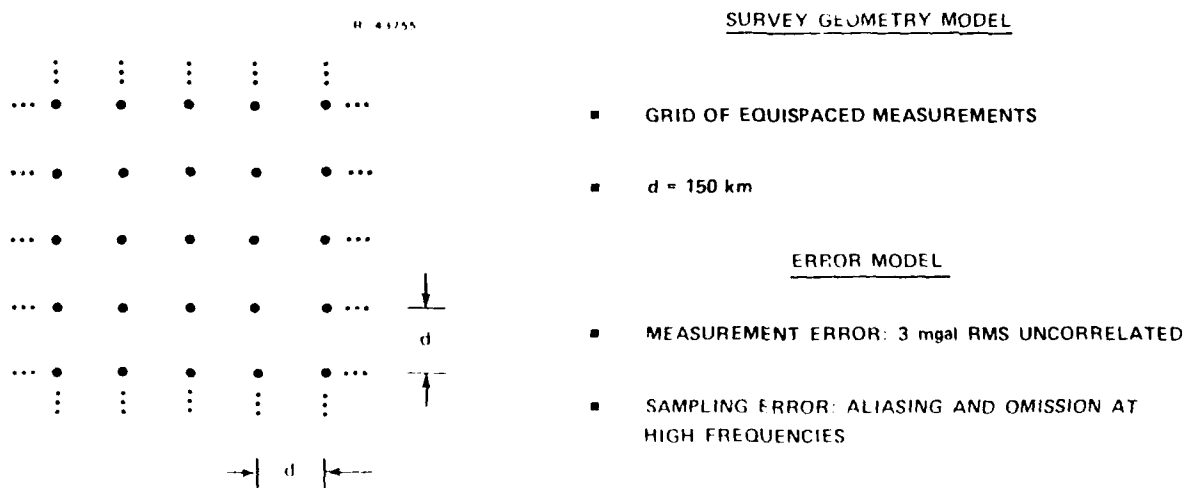
Figure 4.3-2   Land-Based Gravimeter Survey Geometry
and Error Modeling

The gravimeter measurement errors are uncorrelated with each
other and have an rms value of 3 mgal (this includes elevation
errors and reduction errors).

4.4   GRAVITY MODELS

Two gravity models are used to simulate both "active"
and "moderate" gravity fields. The active-field model is the
sum of two third-order stationary random Markov models with
very strong high-frequency content; the rms vertical deflec-
tions are 16.8 $\widehat{sec}$, and the rms anomaly is 113 mgal. Such a
model is appropriate for areas such as mountain ranges, ocean
trenches, escarpments, and other areas with sharp physical
relief.

The moderate-field model is relatively low in high-
frequency energy and has behavior close to the worldwide aver-
age. It is a 5-shell attenuated white noise model (Ref. 28)
with rms deflections of the vertical of 6.8 $\widehat{sec}$ and rms anomaly
of 43 mgal.

4.5   GRADIOMETER ERROR MODELS

The gradiometer-system error model for the Bell base-
line GGI is described in Section 3.7. The error model for the
Bell ball-bearing GGI is similar except for the self-noise,
which is modeled to reflect the preliminary data analysis de-
scribed in Section 2.5. The Draper Floated Gravity Gradiometer
No. 2 is modeled in accordance with the noise spectrum presented
in Section 2.6, plus a preliminary analysis of vibration test data.

95

4.6 SIMULATION RESULTS FOR THE GOAL GRADIOMETER PLUS A SATELLITE ALTIMETER

Before presenting simulation results for the Bell and Draper gradimeters, it is instructive to consider the rms recovery errors for a fictitious "goal" gradiometer, which is defined as having a self noise with a flat power spectrum and an rms value of 1 eötvös when a 10 second moving-window average is used to obtain one measurement every 10 seconds. The goal gradiometer is defined to be insensitive to all environmental disturbances. The along-track vertical deflection recovery errors for this gradiometer model and the active gravity model are described in Fig. 4.6-1, which shows the (two-sided) power spectral density of the errors as a function of wavelength. The lowest curve corresponds to recovery errors when both gradiometry and satellite altimetry are optimally combined. Also shown are the recovery errors when the altimeter data and the gradiometer data are used separately. The effect of limited
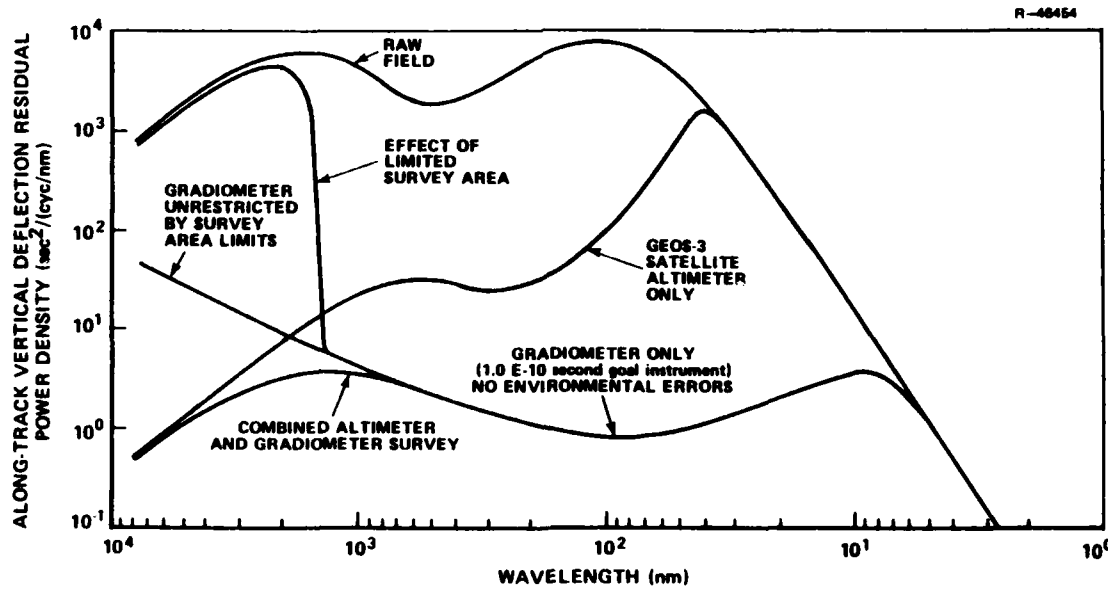
Figure 4.6-1   Gravity Field Recovery by Wavelength (Active Gravity Model)

96

survey area on long-wavelength recovery from gradiometer data alone is also illustrated. For the survey simulation considered here, the goal gradiometer data provide most of the gravity information at wavelengths less than 1000 nm, while the altimeter data supply most of the information for wavelengths longer than 1000 nm.

4.7 SIMULATION RESULTS FOR GRADIOMETRY COMBINED WITH GRAVIMETRY OR ALTIMETRY

The computed rms recovery errors for several gradiometer surveys scenarios are listed in Table 4.7-1. These results were obtained with the smooth worldwide gravity model.

TABLE 4.7-1

MULTISENSOR GRADIOMETER SURVEY PERFORMANCE
(WORLDWIDE GRAVITY MODEL-RMS GRAVITY DISTURBANCE
FIELD IS 6.8 $\widehat{SEC}$, 43 MGAL) AIRBORNE GRADIOMETRY
COMBINED WITH LAND SURVEY/OCEAN SURVEY

R 4651u

GRADIOMETER	NORTH DEFLECTION ERROR (sec-rms)	EAST DEFLECTION ERROR (sec-rms)	VERTICAL DISTURBANCE ERROR (mgal-rms)
NONE*	5.4/1.4	5.4/1.5	36.2/9.6
GOAL GRADIOMETER	0.6/0.5	0.5/0.5	3.8/3.3
BELL GAS BEARING MODEL	2.1/1.0	1.2/1.0	11.4/6.6
BALL BEARING PROTOTYPE[†]	2.1/1.2	1.5/1.2	12.1/7.7
CSDL FLOATED GRADIOMETER NO. 2[**]	1.3/0.5	0.5/0.3	6.4/2.9
CSDL WITH CURRENT NOISE FLOOR EXTENDED TO LOW FREQUENCIES	0.5/0.4	0.4/0.3	3.0/2.3
BALL BEARING PROTOTYPE WITH CURRENT NOISE FLOOR EXTENDED TO LOW FREQUENCIES[†]	1.3/1.1	1.3/1.1	8.8/7.5

*i.e., SURFACE GRAVIMETRY ALONE OR GEOS-3 SATELLITE ALTIMETRY ALONE

[†]BASED ON PRELIMINARY DATA

[**]BASED ON PRELIMINARY ANALYSIS OF VIBRATION TEST DATA

The rms errors are listed in pairs separated by slashes: values to the <u>left</u> of the slashes are the errors for gradiometry plus <u>gravimetry</u>, while values to the <u>right</u> are for gradiometry combined with satellite <u>altimetry</u>.

The first row represents the limiting case of no gradiometry. The resulting errors are large because the gravimetry and altimetry lack information about the gravity field at medium and short wavelengths. The second row applies to the fictitious goal gradiometer system introduced in the previous section. The third row corresponds to the Bell GGI system error model that was developed in this report, while the fourth row was obtained with a preliminary error model for the Bell ball-bearing gradiometer

Results for the Draper (CSDL) Floated Gradiometer No. 2 are in rows 5 and 6. The last two rows (6 and 7) contain estimated recovery errors for <u>idealized</u> Draper and Bell gradiometers that are defined to be free of long-term random drift, i.e., there are no low-frequency "red" components in their self noises. This limiting case may be approximated in practice by intentionally rotating the gradiometer platform so as to modulate the gradients sensed by the gradiometer. Additional signal processing is then required for demodulating the gradiometer measurements to recover the gradient components. An analysis of intentional platform motion is given in Appendix D.

Table 4.7-2 lists projected rms recovery errors for the same gradiometer surveys covered by Table 4.7-1, except that here the <u>active</u> gravity model is used. The much larger high-frequency energy in the active gravity model yields larger rms recovery errors as compared with the worldwide gravity model.

TABLE 4.7-2

MULTISENSOR GRADIOMETER SURVEY PERFORMANCE (ACTIVE GRAVITY
MODEL-RMS DISTURBANCE FIELD IS 16.8 SEC, 113 MGAL) AIRBORNE
GRADIOMETRY COMBINED WITH LAND SURVEY/OCEAN SURVEY

n-46516

GRADIOMETER	NORTH DEFLECTION ERROR (sec-rms)	EAST DEFLECTION ERROR (sec-rms)	VERTICAL DISTURBANCE ERROR (mgal-rms)
NONE*	16.4/5.4	16.4/8.0	110/46.0
GOAL GRADIOMETER	1.4/1.3	1.1/0.9	8.0/7.5
BELL GAS BEARING MODEL	4.0/2.2	1.9/1.6	20.9/12.7
BALL BEARING PROTOTYPE[†]	4.1/2.5	2.3/2.0	22.3/15.1
CSDL FLOATED GRADIOMETER NO. 2**	3.5/1.9	1.0/0.8	17.4/9.6
CSDL WITH CURRENT NOISE FLOOR EXTENDED TO LOW FREQUENCIES	1.4/1.3	0.9/0.8	8.0/7.0
BALL BEARING PROTOTYPE WITH CURRENT NOISE FLOOR EXTENDED TO LOW FREQUENCIES†	2.1/2.0	2.1/2.0	14.2/13.3

*i.e., SURFACE GRAVIMETRY ALONE OR GEOS-3 SATELLITE ALTIMETRY ALONE

†BASED ON PRELIMINARY DATA

**BASED ON PRELIMINARY ANALYSIS OF VIBRATION TEST DATA

99

5. AIRBORNE GRADIOMETER TEST PLAN ELEMENTS

5.1 STATUS OF ONGOING GRADIOMETER DEVELOPMENT

The Bell Aerospace Division of Textron, Inc. (under contract with the Sperry System Management Division of Sperry Rand Corp. and sponsored by the Strategic Systems Project Office of the Navy) is currently developing an Advanced Development Model (ADM) gravity gradiometer system, which is to include the following:

- Three ball-bearing gradiometers

- Three gyros suited for carouselling experiments and jitter compensation

- Inertial platform

- Temperature controlled binnacle

- Vibration isolators

- Associated electronic equipment.

The package is designated the Gravity Sensor System (GSS) ADM. Preliminary to the ADM, Bell is testing two ball-bearing gradiometers, designated AF-2 S/N 1 and S/N 2, which are development versions of the gradiometers to be used in the GSS. The delivery date for the GSS ADM is planned for October 1981, as indicated in Fig. 5.1-1. If the Navy development proceeds according to plan, Bell will have the capability to produce a gradiometer triad for airborne use soon thereafter.

```
                                                              R—50986

  ┃├─── GSS ADM DEVELOPMENT ──────►┃├── AT-SEA TESTING ──────►
            (Already Scheduled)

  └──────────┴──────────────┴──────────────┴──────────►
  Jan 1980        Jan 1981       Jan 1982       Jan 1983
```
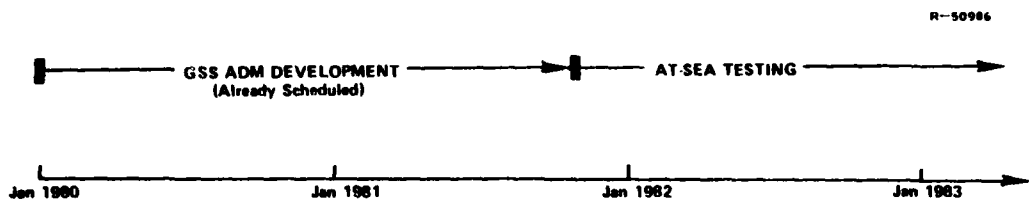
Figure 5.1-1   Ongoing GSS ADM Development

Although actual flight testing of gradiometers is
several years away, and the concomitant details of the test
scenario are unknown, several factors and issues are now clear.
This section briefly discusses these areas and directs emphasis
toward the "long lead-time" items. The overall objective is
to illustrate, for planning use by DMA, the key portions of a
coordinated airborne gradiometer test program. An overall
schedule which such a program might follow is presented in
Fig. 5.1-2.

5.2   TEST PROGRAM ITEMS

In one sense the initial portion of an airborne grad-
iometer test program has already begun with the analysis of
both Bell and Draper moving-base data. While a continuing
study of laboratory data is a necessary adjunct to a success-
ful airborne gradiometer program, this section looks beyond
the expected evolutionary developments of laboratory testing.
The items below are directed towards the epoch following de-
livery of a gradiometer triad and its stabilized platform to a
test site remote from the manufacturer's laboratory.
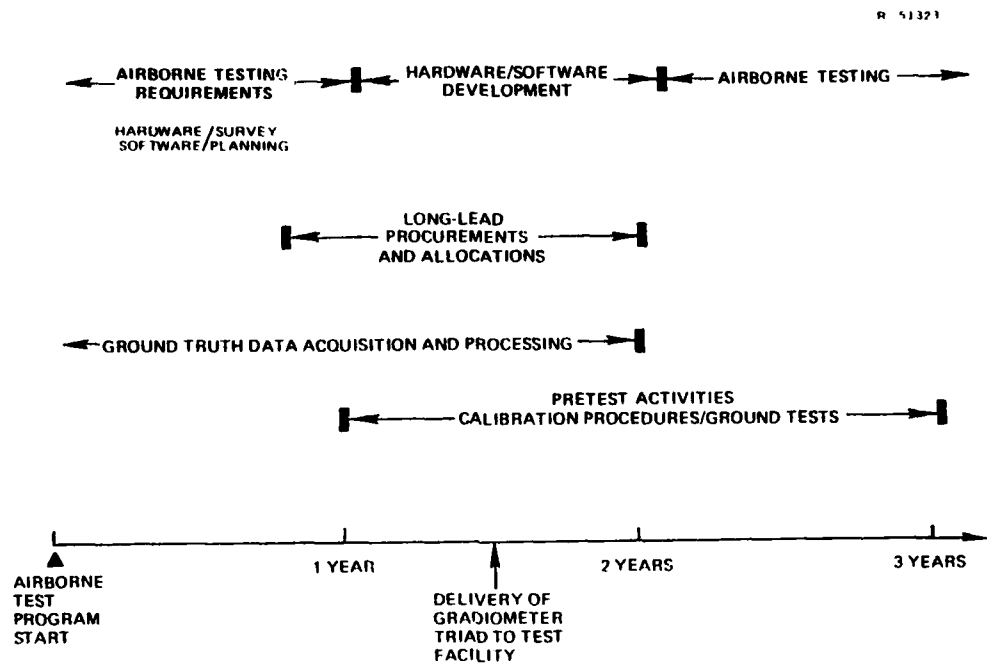
Figure 5.1-2   Elements of an Airborne Gradiometer Test Program

Ground Truth - The accuracy, density, and total
coverage of gravity data required to support air-
borne testing is yet to be determined. Ancillary
issues include types of data most appropriate
for the database (e.g., gravity vs. deflections
of the vertical), the data subsets required for
moving-base checkout testing on the surface,
data needed for system calibration, and the pro-
cessing techniques to be used for upward continu-
ation to aircraft altitude. The acquisition and
reduction of these data will require considerable
lead time.

Inertial Navigation System (INS) and Navigation
Aid Selection - The choice of aircraft, test
site, and test-program navigation accuracy re-
quirements will be the chief constraints in se-
lecting an INS. The use of Navigation Aides
(Navaid) will largely be dictated by availabil-
ity and cost. Integration of a Global Positioning
System (GPS) receiver into the system is particu-
larly promising. In the absence of GPS, a radar

altimeter and doppler radar would probably be required. Lead and back-up navigation systems need to be defined, selected, and procured in pace with gradiometer acquisition.

Data Recording and Monitoring - The equipment and system required for adequate monitoring of the gradiometer triad's performance must be defined. Among the issues to be resolved include which variables are to be recorded, necessary environmental data monitors, the degree of post-mission vs. real-time data processing to be done, onboard storage vs. telemetry as well as data formats and hierarchy. In addition to allowances for system procurement and setup time, a period of test equipment software development is likely to be needed.

Ground Testing - Prior to operation in an aircraft, testing and calibration of the gradiometer triad and platform must be performed at the airfield. The detail and extent of this testing will be dictated by the philosophy of those directing the program at the time. Ground testing can range from simple check-out of the gradiometer instruments and recording systems prior to flight, to a complete ground test program designed to provide high predictability of flight test performance. Regardless of the specific program chosen, well-defined procedures and schedules must be developed. Similarly, the analysis objectives for the ground test data should be specified early in the program. Some software development is likely to be required for the data analysis.

Flight Test Operational Plan - Because of the high cost of operating test aircraft, it is desirable to maximize the information return from each flight. A pre-flight checkout procedure is therefore necessary for the gradiometer/INS/Navaid systems, as well as data recording and/or telemetering equipment. In-flight procedures are required to verify proper data acquisition and to make data-reasonableness checks. Post-flight calibration procedures should also be well-defined.

Flight Test Data Analysis/Evaluation - Comparison of in-flight gradiometer measurements to data derived from ground truth will most likely be performed after the flight. Many other facets

of gradiometer performance will probably have to
be studied post-mission too. Sufficient time
and resources should be allocated for this ac-
tivity. Experience has shown that unanticipated
problems can seriously impact the effort required
in this phase of the test program. Close coor-
dination of the gradiometer navigation, data
acquisition, and truth data development are re-
quired to prevent such surprises.

Technical Improvement/Iteration Procedures - In
a development program such as gradiometry, it is
in the interest of all parties to assure that
needed adjustments, design changes, and repairs
are affected from time to time. It is also nec-
essary that such procedures occur with the cog-
nizance of appropriate personnel and in an
orderly fashion. Procedures for such actions
must be designed which assure adequate documen-
tation and discipline for all with access to the
instrumentation, but encourage creativity and
rapid response to problems that may develop.

Test Program to Survey Transition - Once confi-
dence in the gradiometer is established, and
error estimates for its airborne performance are
obtained, flights might be extended to areas
where ground truth data are not dense. Simi-
larly, the training of new nonflight-test per-
sonnel might be appropriate. Such flights could
be interspersed with test program flights as the
program nears completion. To effect an efficient
transition to survey procedures, requirements
and goals of the survey program should be defined.

5.3 APPROPRIATE NEXT STEPS

The current umbrella-angle design for a triad of Bell
gradiometers (Ref. 3) is suitable for airborne survey opera-
tions with a moderate augmentation of the instrument's band-
width. This bandwidth increase is not expected to be difficult.

A gradiometer inertial platform, integral with the
gradiometer triad, is under development by Bell. However, it

is currently unclear to what extent the Bell-designed platform, intended for marine use, will have to be modified for the airborne application. This is the chief critical-path item for airborne gradiometry as of this date.

Bell has not yet implemented their gradiometer's jitter compensation scheme in an on-line environment. Although the concept appears sound (see Appendix A), it should be tested prior to an extensive commitment to an airborne test program. Definitive testing would demonstrate an operative gradiometer mounted on the intended aircraft-compatible inertial platform while subjected to linear and angular vibration that simulates the host aircraft. The testing should include conditions of angular motion (such as encountered in an aircraft) of the stabilizing platform's base.

As stated earlier, continued monitoring of the manufacturer's development and laboratory testing is necessary. This effort, in addition to enabling DMA to maintain a high level of technical awareness in the field of gradiometry, also provides the flexibility to embark, without delay, on a wider program of airborne gradiometry as the resources become available.

6.   CONCLUSIONS AND RECOMMENDATIONS

The accuracy with which gravity can be estimated from an airborne gradiometric survey depends on the gravity field, the survey geometry, the additional data from other sensors, and the gradiometer measurement errors. This report has focused on the last of these factors by describing error models for airborne gradiometers. These models have been incorporated in the TASC Multisensor Survey Simulation software, which provides estimates of recovery errors when different types of gravity survey data are optimally combined.

The error models in this report were chosen to fit test data for the baseline Gravity Gradiometer Instrument No. 1 (GGI No. 1) developed by the Bell Aerospace Division of Textron, Inc. This is the gradiometer for which comprehensive formal test data have been analyzed, and its performance is believed to be indicative of the Bell ball-bearing gradiometers that are currently being built for field tests in 1981. It is recommended that the error models in this report be updated to fit test results for the Ball-Bearing instrument when additional data for that gradiometer are available.

Investigative test results and a limited amount of formal test data were available on the Floated Gravity Gradiometers (FGG's) developed at the Charles Stark Draper Laboratory. Analysis of these data yielded self-noise spectra for the FGG NO. 2 that are included in this report. The FGG models for vibration-induced errors, however, are only preliminary and are subject to change after additional data are analyzed.

Gradiometer measurement errors are due to systematic effects, self noise originating inside the instrument, and to environmental disturbances to which the gradiometer is sensitive. The dominant measurement errors during an airborne survey are expected to be caused by the self noise and the mechanical vibration environment of the gradiometers. Major emphasis in this report was therefore placed on these two error sources.

Analysis of the test data indicates that the self noise in the inline and cross channels of the Bell baseline GGI is well modeled as two random processes. Power spectral densities for these processes were estimated from data for both vertical (VSA) and horizontal spin-axis (HSA) orientations of the gradiometer.

- At frequencies below 0.1 millihertz (mHz), the spectral densities are inversely proportional to the frequency squared. This is termed "red" noise, and it accounts for <u>long-term drift</u> in the gradiometer outputs

- At higher frequencies (2 mHz < f < 24 mHz), the spectral densities are independent of frequency. This is the "white-noise floor," and it accounts for <u>short-term variability</u> in the gradiometer outputs.

- The rms accumulated random drift projected for a 5-hour survey is 4.2 eötvös (E) for VSA and 5.3 E for HSA. The measurement averaging time for these projections is 10 seconds.

Analysis of test data for the Draper FGG No. 2 indicates that its self noise has the following properties:

- The power spectra of the FGG's self noise are <u>similar in shape</u> but <u>smaller in magnitude</u> as compared with those of the Bell

107

GGI (the FGG No. 2 spectral magnitudes
are typically 3 percent of the corre-
sponding Bell baseline GGI spectral mag-
nitudes)

● The. projected rms accumulated random
drift during a 5-hour survey is 0.6 E
for a 10-second averaging time.

Analysis of Bell vibration data, together with flight
test data on the vibrations of an NKC-135A aircraft, led to
the following conclusions regarding vibration-induced measure-
ment errors during airborne gradiometric surveys:

● Aircraft angular jitter is expected to
induce small measurement errors. In con-
trast, uncompensated inertial platform
jitter is identified as a potentially
important error source. Compensation
for platform jitter appears to be feasi-
ble and may reduce the jitter-induced
errors. The successful implementation
of such compensation, however, remains
to be demonstrated

● Aircraft linear vibrations are expected
to induce uncorrelated measurement errors
that are comparable in order of magnitude
to the gradiometer's white-noise floor.
This conclusion is based on available
flight test data.

Error models were developed for airborne gradiometric
survey systems that consist of three gradiometers mounted on
one inertial platform. These error models were incorporated
into the Multisensor Survey Simulation routines and used to
compute the rms errors inherent in statistically optimal re-
coveries of point values for the gravity vector when airborne
gradiometry is combined with long-wavelength data from satel-
lite altimetry or land-based gravimetry. The following is a
sample of the simulation results.

- When airborne gradiometry is combined
  with satellite altimetry, the worldwide
  rms vertical disturbance error is 3.3
  mgal, and the rms along-track vertical
  deflection error is 1.0 sec for the Bell
  baseline GGI

- For the Draper FGG No. 2 the correspond-
  ing rms vertical disturbance error is 2.9
  mgal, and the rms along-track vertical
  deflection error is 0.3 sec.

Future modifications of the gradiometer error models
are expected to include:

- Adjustments of parameter values to re-
  flect additional test data from the Bell
  Ball-Bearing GGI

- The addition of a platform jitter model
  if justified by future test data

- Refinements in the aircraft vibration
  models if additional flight test data
  representative of survey conditions be-
  come available.

From the data that were analyzed for this report as
well as the technical maturity of both the Bell and Draper in-
struments, it appears likely that the transition from labora-
tory to various types of field tests is near. In this context
the following recommendations are made to assist in the plan-
ning and development of an airborne gradiometric survey capa-
bility. The focus is on elements that should be addressed
soon to provide maximum flexibility in later airborne gradi-
ometer program activity.

- Current gradiometer data analysis studies
  should be continued to provide DMA with
  ongoing high-level technical insight into

gradiometer development. Such studies should include test data processing as well as independent mechanization studies and should relate gradiometer design developments to the airborne survey scenario

- Independent analysis of gradiometer platform requirements should be initiated

- Planning for a gradient "truth data base" should commence at the earliest possible date. Even before the selection of a test site, the type, accuracy, densification, and extent of required surface data must be determined. The generation of gravity gradients for comparison with gradiometer outputs at aircraft altitudes is likely to require considerable time. The necessarily large quantities of data should therefore be matched with efficient algorithms (e.g., GEOFAST in references 32 and 33).

APPENDIX A
JITTER COMPENSATION TECHNIQUE
FOR THE BELL GRADIOMETER

The purpose of this Appendix is to examine Bell's
method of gradiometer compensation for angular jitter motion
of the inertial stabilization platform. In the approach stud-
ied, a gyro is used to measure the jitter and to compute cor-
rections continuously for the gradiometer outputs. The com-
pensation is to be applied in real time.

The analysis herein finds this approach to be viable
if the gradiometer's mechanical structure meets certain yet-
to-be-demonstrated goals. A description of these requirements
is provided in Section A.2. Conclusions are given in Section
A.3.

A.1   INTRODUCTION

Concerns have been expressed in the gradiometer com-
munity that gyro-based jitter compensation could prove inef-
fective because of the wide-bandwidth multiplications required
to compute the jitter-correction gradient terms. The potential
problem is that gyro noise over the bandwidth from DC to the
mechanical response cutoff frequency of the gradiometer plat-
form would be excessive. The following example is illustra-
tive.

Suppose a gradiometer is mounted on a "state-of-the-
art" platform which exhibits randomly occuring limit-cycle

111

behavior with an average frequency of 20 Hz. Consider sinu-soidal platform motion with an amplitude of 1 arcsecond ($\widehat{\sec}$), i.e.,

$$\theta = \theta_m \cos 2\pi ft \qquad (A.1-1)$$

where $\theta_m = 1.0 \; \widehat{\sec}$ and $f = 20$ Hz. The angular velocity of the limit cycle is

$$\dot{\theta} = -2\pi f\theta_m \sin 2\pi ft \qquad (A.1-2)$$

with a peak value of

$$\dot{\theta}_m = 2\pi f\theta_m = 40\pi \; \widehat{\sec}/s \qquad (A.1-3)$$

The corresponding centripetal gradient is

$$\Gamma = \dot{\theta}^2 = \frac{1}{2}\dot{\theta}_m^2 - \frac{1}{2}\dot{\theta}_m^2 \cos 4\pi ft \qquad (A.1-4)$$

Only the DC part of Eq. A.1-4 is of concern because the double-frequency term is beyond the gradiometer's operating bandwidth. However, since the platform jitter is not stationary (i,e., it comes and goes), the "DC" term in Eq. A.1-4 appears as a random gradiometer output.

Using the jitter-rate amplitude of (A.1-3) yields the rectified term

$$\Gamma_{DC} = 8.0 \cdot 10^2\pi^2 \; \widehat{\sec}^2/s^2 = 186 \; E \qquad (A.1-5)$$

This is the measurement error that an uncompensated gradiometer would exhibit in the presence of platform jitter as described above. Note that if the limit-cycle amplitude were a factor

112

of ten larger (10 arcseconds), the effect on gradient error would be a factor of one hundred worse.

Since this single-frequency error is an impulse in the frequency domain, it can be observed with a very large signal-to-noise ratio. Therefore, compensation for jitter-induced error presents no problem in the single-frequency case.

However, several questions remain:

- What happens if the limit cycle is more realistically characterized by a spectrum containing harmonics?

- What is the net effect of gyro self-noise on gradiometer output error?

- What level of gyro resolution is required?

- The jitter-induced gradient error originates as an acceleration error. Thus the rectified portion of the jitter is comprised of all jitter frequencies contained within the platform's mechanical response bandwidth. (Neither the gradiometer signal bandwidth nor the accelerometer constrainment loop bandwidth are important.) How much difficulty do high frequency mechanical resonances cause?

A.2 JITTER COMPENSATION ISSUES

A.2.1 Rectification Effect

Angular motion of the gradiometer instrument affects the individual sensed gradients via the following relation

113

$$\delta\Gamma = \begin{bmatrix} -(\omega^2 + \Omega_y^2) & \Omega_x\Omega_y & \omega\Omega_x \\ \Omega_x\Omega_y & -(\omega^2 + \Omega_x^2) & \omega\Omega_y \\ \omega\Omega_x & \omega\Omega_y & -(\Omega_x^2 + \Omega_y^2) \end{bmatrix}$$

$$(A.2-1)$$

where $\delta\Gamma$ is the jitter-induced gradient tensor measurement error, ω is the jitter rate about the spin axis, and Ω_x and Ω_y are jitter rates about two other orthogonal axes.

Jitter about the spin axis does not appear in the Bell gradiometer's output. Thus, terms of interest are gradient errors of the form

$$\delta\Gamma = \Omega_x^2, \ \Omega_y^2, \ \Omega_x\Omega_y \qquad (A.2-2)$$

Examination of a single component of jitter is instructive. Consider Ω_x to be Gaussian random process and to have the power spectrum $S_{xx}(f)$. The gradient error spectrum of $\delta\gamma$ is given by (Ref. 29 Eq. 14-20)

$$S_{\Gamma\Gamma}(f) = 2S_{xx}(f) * S_{xx}(f) + \sigma_x^4 \delta(f) \qquad (A.2-3)$$

where σ_x^2 is the variance of Ω_x, $\delta(f)$ is the Dirac delta function, and $*$ denotes convolution. The second term of Eq. A.2-3 is the source of the rectification. The magnitude of this effect, if uncompensated, was illustrated in Section A.1.

A.2.2 Compensation

The jitter signal Ω_x is to be measured by a gyro with error ε_g (also a Gaussian random process)

114

$$m = \Omega_x + \varepsilon_g \qquad (A.2-4)$$

The estimated jitter gradient is

$$\hat{\delta\Gamma} = m^2 = \Omega_x^2 + 2\varepsilon_g\Omega_x + \varepsilon_g^2 \qquad (A.2-5)$$

The actual jitter gradient is

$$\delta\Gamma = \Omega_x^2 \qquad (A.2-6)$$

The resulting compensated gradiometer output error is

$$\delta\Gamma_\varepsilon = \hat{\delta\Gamma} - \delta\Gamma = 2\varepsilon_g\Omega_x + \varepsilon_g^2 \qquad (A.2-7)$$

The autocorrelation of $\delta\Gamma_\varepsilon$ is given by

$$R_{\varepsilon\varepsilon}(\tau) = 4E\{\tau_g(t)\,\Omega_x(t)\,\varepsilon_g(t-\tau)\,\Omega_x(t-\tau)\}$$
$$+ 2E\{\tau_g(t)\,\Omega_x(t)\,\varepsilon_g(t-\tau)\,\varepsilon_g(t-\tau)\}$$
$$+ 2E\{\varepsilon_g(t)\,\varepsilon_g(t)\,\varepsilon_g(t-\tau)\,\Omega_x(t-\tau)\}$$
$$+ E\{\varepsilon_g(t)\,\varepsilon_g(t)\,\varepsilon_g(t-\tau)\,\varepsilon_g(t-\tau)\} \qquad (A.2-8)$$

where t is signal time and τ is shifted time. $E\{...\}$ is the ensemble expectation operator. Using Eq. 4.9 of Ref. 31, Eq. A.2-8 can be reduced to

$$R_{\varepsilon\varepsilon}(\tau) = 4 \quad R_{gx}^2(0) + R_{gg}(\tau)\,R_{xx}(\tau) + R_{gg}(\tau)\,R_{xg}(\tau)$$
$$+ 2 \quad R_{gx}(0)\,R_{gg}(0) + R_{gg}(\tau)\,R_{xg}(\tau) + R_{gg}(\tau)\,R_{xg}(\tau)$$
$$+ 2 \quad R_{gg}(0)\,R_{gx}(0) + R_{gg}(\tau)\,R_{gx}(\tau) + R_{gx}(\tau)\,R_{gg}(\tau)$$
$$+ R_{gg}^2(0) + 2R_{gg}^2(\tau)$$
$$\qquad (A.2-9)$$

115

where the correlaton functions are defined according to

$$R_{gx}(\tau) = E \{\varepsilon_g(t) \, \Omega_x \, (t-\tau)\} \qquad \text{(A.2-10)}$$

Since platform jitter and gyro errors are uncorrelated,

$$R_{gx}(\tau) = R_{xg}(\tau) = 0 \qquad \text{(A.2-11)}$$

Using Eq. A.2-11 to simplify Eq. A.2-9 gives

$$R_{\varepsilon\varepsilon}(\tau) = 4 \, R_{gg}(\tau) \, R_{xx}(\tau) + 2R_{gg}^2(\tau) + \sigma_g^2 \, \sigma_x^2 \qquad \text{(A.2-12)}$$

Taking the Fourier transform of Eq. A.2-12 gives the power spectral density (PSD) of the residual gradiometer error due to jitter,

$$S_{\varepsilon\varepsilon}(f) = 4 \, S_{gg}(f) * S_{xx}(f) + 2S_{gg}(f) * S_{gg}(f) + \sigma_g^4 \delta(f)$$
$$\text{(A.2-13)}$$

The final term of Eq. A.2-13 contributes only to the zero-frequency component of $\delta\Gamma_\varepsilon$; the rms contribution is

$$\delta\Gamma_\varepsilon^{DC} = \sigma_g^2 \qquad \text{(A.2-14)}$$

It is convenient to preserve the distinction between the DC and all other spectral components of $\delta\gamma_\varepsilon$. The DC effect is treated first.

Gyro errors for second generation dry-tuned gyros such as those used the LN-15 inertial navigation system have

---

*Gyro vendor data indicate that error spectra as low as 10^{-4} $(\text{deg/hr})^2/\text{Hz}$ over this bandwidth are available.

been modeled by a first-order Markov process with an rms value of 10^{-3} deg/hr and a correlation time of 2 hours (Ref. 30). Bell has tested and expects to use an advanced version of this, or a similar gyro, for jitter detection. The gyro error PSD (white) at low frequencies is

$$S_g = 3.6 \times 10^{-3} (\widehat{sec}/s)^2/Hz* \qquad (A.2-15)$$

It is instructive to consider the case in which the increased bandwidth required for jitter compensation (100 Hz)* is accomplished only at the expense of accepting the error spectral density, S_g, over the entire gyro pass band. The gyro error variance is then

$$\sigma_g^2 = \int_{-100}^{100} S_g df = 0.72 \; (\widehat{sec}/s)^2 \qquad (A.2-16)$$

which yields a DC gradient error of

$$\delta\Gamma_\varepsilon^{DC} = 0.02 \; E \qquad (A.2-17)$$

This result indicates that the DC component is not a significant source of error.

Turning to the frequency spectrum of $\delta\Gamma_\varepsilon$, evaluation of the first two terms of Eq. 2.2-10 is required. Taking the gyro error spectrum to be white out to its cutoff frequency f_{co} (f_{co} = 100 Hz) gives

$$S_{gg}(f) = \begin{cases} S_g & |f| \leq f_{co} \\ 0 & |f| \geq f_{co} \end{cases} \qquad (A.2-18)$$

---

*100 Hz is used as the effective cutoff frequency for platform mechanical response.

which is to be inserted into

$$S_{\varepsilon\varepsilon}(f) = 4S_{gg}(f) * S_{xx}(f) + 2S_{gg}(f) * S_{gg}(f) \qquad (A.2\text{-}19)$$

It is convenient to rewrite Eq. A.2-16 to include f_{co} as a parameter

$$S_g = \frac{\sigma_g^2}{2f_{co}} \qquad (A.2\text{-}20)$$

For the numerical values considered, the second convolution in Eq. A.2-19 yields the error spectrum $S_{\varepsilon\varepsilon}^{(2)}(f)$ shown in Fig. A.2-1. The maximum value is

$$S_{\varepsilon\varepsilon}^{(2)}(0) = \frac{\sigma_g^4}{f_{co}} = 3 \times 10^{-4} \ E^2/Hz \qquad (A.2\text{-}21)$$

This result is more than 5 orders of magnitude smaller than the self-noise spectral density of the Bell GGI discussed in Chapter 2. Therefore, the second term in Eq. A.2-19 is negligible.
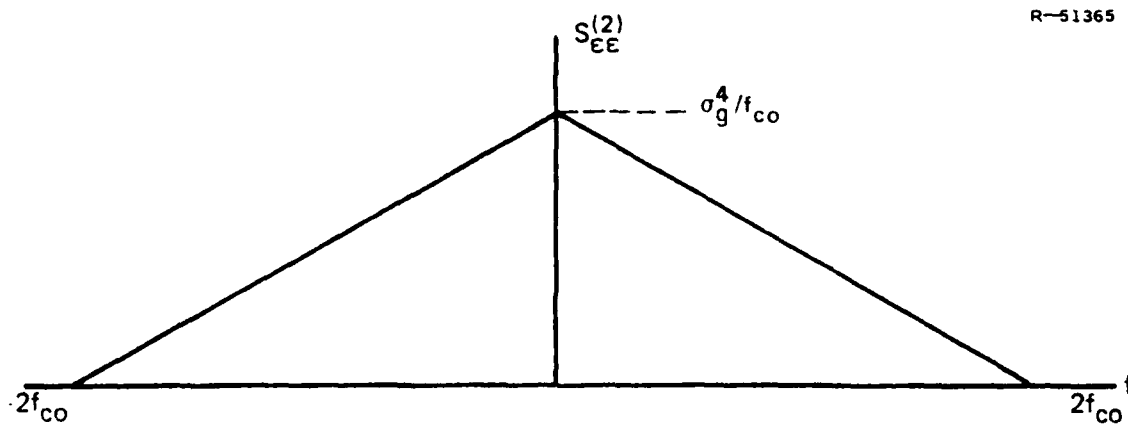
Figure A.2-1   Frequency Spectrum $S_{\varepsilon\varepsilon}^{(2)}(f)$

It remains to evaluate the first convolution term of Eq. A.2-19. Although discussion of jitter spectra is deferred until Section A.2.4 it is useful to anticipate a worst-case jitter model as illustrated in Fig. A.2-2.
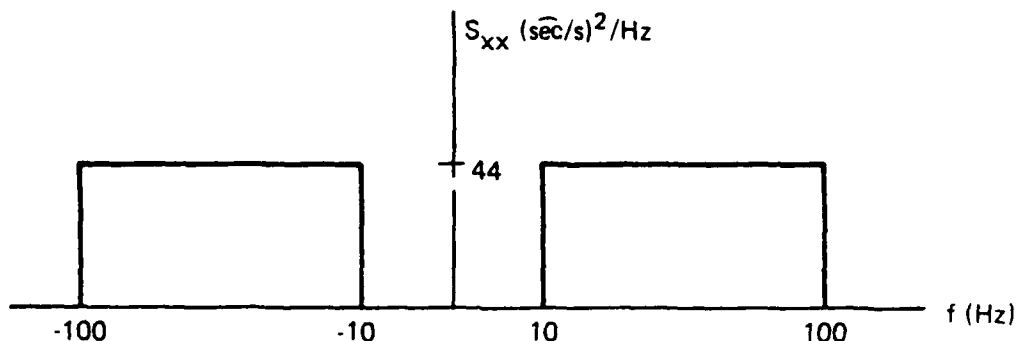
Figure A.2-2   Band-Limited White-Noise Jitter Spectrum (Schematic)

The result of convolving the jitter and gyro error spectra is

$$S_{\varepsilon\varepsilon}^{(1)}(0) = 0.06 \ E^2/Hz \qquad (A.2-22)$$

Although this spectral level is somewhat larger than the one in Eq. A.2-21, it is still too small to contribute significant gradiometer error.

A.2.3 Resolution

Suppose the gyro's resolution is no worse than the rms value of its broadband noise, given in Eq. A.2-16 as 0.85 $\widehat{sec}/s$. If the resolution is the same at all frequencies, the worst-case effect occurs when the jitter is wideband and of density greater than the resolution density over the entire band. In that case the contribution of gyro resolution is

119

nearly same as that of gyro self-noise and is therefore negligible in comparison to the gradiometer's self noise.

A.2.4 Gyro-to-Platform Relative Motion

The gradiometer body exhibits resonances that occur near the mechanical frequency-response limits of the structure. Because of the modal motion associated with resonance conditions, the gyro is subjected to different angular vibrations than are experienced by the gradiometer. Bell has measured this effect as a function of frequency (Ref. 27). The departure of gyro-measured jitter gradients from gradiometer-measured jitter gradients is indicated in Fig. A.2-3. Note that deviation begins to occur at 10 Hz and becomes serious at 40 Hz.
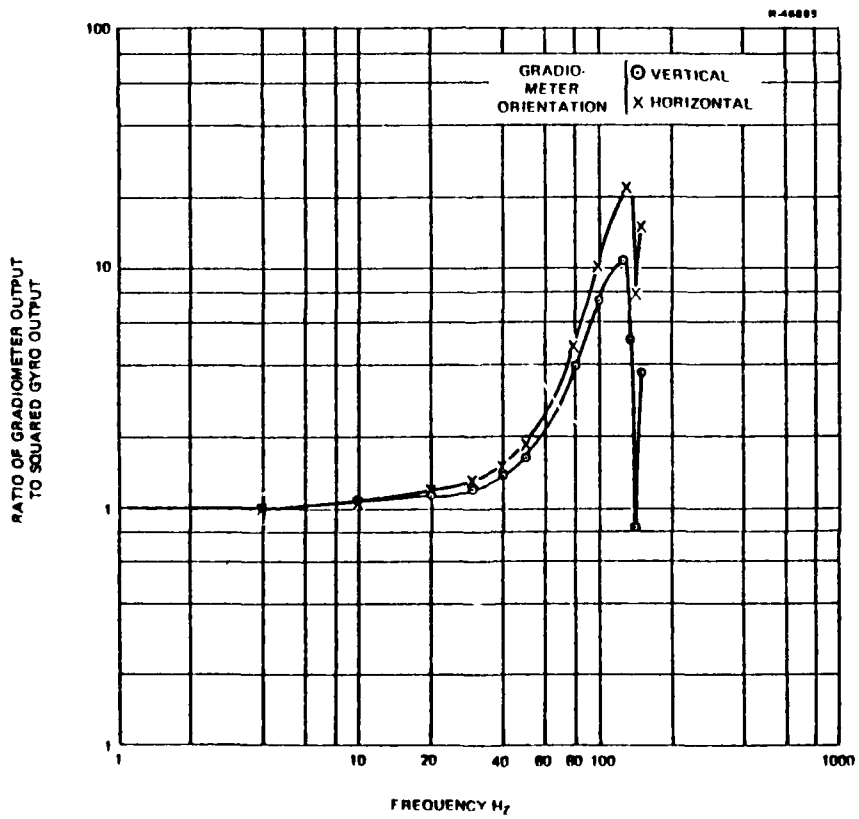
Figure A.2-3   Bell Jitter Compensation Test Results

Measurement capability is effectively lost by 100 Hz. To the extent that these resonances are stable, some improvement will be realized by using shaping filters at the gyro output. However only small gains are to be expected with this technique.

Estimates of gradient errors (which, because of resonances, are "not seen" by the gyro) depend strongly on the spectral distribution of the assumed jitter. The following two cases are illustrative.

A.2.5 White Noise Platform Jitter Model

A pessimistic jitter model that has a flat spectrum between 10 Hz and 100 Hz can be rationalized as follows: Consider the fundamental limit-cycle frequency of 20 Hz to have a bandwidth of ±10 Hz. Let the attenuation of the harmonics be offset by the increased structural response at higher frequencies. Consider the case of a structural response with a cutoff frequency of 100 Hz.

The rms jitter rate corresponding to Eq. A.1-3 is

$$\sigma_x = 20\sqrt{2}\,\pi = 89 \; \widehat{sec}/s \qquad\qquad (A.2\text{-}23)$$

The flat PSD is obtained from

$$\sigma_x^2 = 2(100 - 10)\, S_{xx} \qquad\qquad (A.2\text{-}24)$$

which gives

$$S_{xx}(f) = \begin{cases} 44(\widehat{sec}/s)^2/Hz & 10 \text{ Hz} \le |f| \le 100 \text{ hz} \\ 0 & otherwise \end{cases}$$

$$(A.2\text{-}25)$$

If the jitter below 60 Hz is compensated, the variance of the uncompensated portion is:

$$\sigma^2_{uncomp} = 2\ (100\text{-}60)S_{xx} = 3.5 \times 10^3 (\widehat{sec}/s)^2$$

$$(A.2\text{-}26)$$

The resulting DC gradient measurement error is

$$\sigma_\Gamma = 82\ E \qquad (A.2\text{-}27)$$

An additional error results from the spectral components represented by the convolution in Eq. A.2-3. The resulting error within the gradiometer's passband, due to this term, is white noise with a spectral density of 173 E^2/Hz. Note that this value is the error spectrum for the second inline gradient term of Eq. A.2-1. To compare this figure with error spectra for the Bell gradiometer, it is appropriate to take into account the measurement provided by the gradiometer's inline channel, Eq. 3.4-12. When this is done and an equal magnitude of independent uncompensated jitter is present in the y direction, the jitter error spectrum referenced to the Bell gradiometer's inline channel is 82 E/Hz. This is comparable in magnitude to the instrument's self noise (see Fig. 2.5-1) and is therefore a significant error source.

A.2.6 Harmonic Jitter Model

Consider a platform limit cycle that is narrow-band at 20 Hz and, in the worst case, is only piecewise continuous. The jitter spectrum is given by

$$S_{xx}(f) = A \sum_{n=1}^{5} \frac{1}{n^2} [\delta(f\text{-}20n) + \delta(f\text{+}20n)] \qquad (A.2\text{-}28)$$

122

where n=5 corresponds to the 100 Hz cutoff. The constant A is selected so that the rms jitter is again given Eq. A.2-23, i.e.,

$$A = \frac{\sigma_x^2}{\int_{-100}^{100} \sum_{n=1}^{5} \frac{1}{n^2} [\delta(f-20n) + \delta(f+20n)] \, df} = 2.7 \times 10^3 \, (\widehat{sec}/s)^2$$

(A.2-29)

Neglecting structural effects and again assuming no gyro compensation above 60 Hz yields the uncompensated jitter variance

$$\sigma_{x(uncomp)}^2 = 2A \sum_{3}^{5} \frac{1}{n^2} = 1.2 \times 10^3 (\widehat{sec}/s)^2 \qquad (A.2-30)$$

This is the appropriate variance to use in the delta-function term of Eq. A.2-3. However, because the model of Eq. A.2-28 is comprised solely of impulse functions, the convolution of Eq. A.2-3 contributes additional zero-frequency power to the jitter gradients. Since only the zero-frequency component of the convolution falls within the gradiometer's passband, only the power at zero frequency is of interest. The variance of this uncompensated jitter gradient is

$$\sigma_{g(uncomp)}^2 = 4 A^2 \sum_{n=3}^{5} \frac{1}{n^2} = 5.2 \times 10^5 (\widehat{sec}/s)^4 \qquad (A.2-31)$$

Adding the "$\smile$" term of Eq. A.2-30 to the result of Eq. A.2-31 yields an rms value for the total gradient bias of

$$\sigma_g = 32 \text{ E} \qquad (A.2-32)$$

123

A.2.7 Discussion

The values of rms gradiometer error given by Eq. A.2-27 and A.2-31 represent extremes for 1 arcsecond of platform jitter motion. The actual effect of high-frequency jitter probably falls somewhere in between. However, it is reasonable to conclude that the demonstrated Bell jitter compensation capability leaves room for gradiometer error of several tens of eötvös (or more) for a less-than-superb platform.

Note that some gradiometer platform designs are under consideration for which the goal is an inner element that is "jitter free" when the platform is at rest. Although such a platform would provide a very beneficial gradiometer environment, platform jitter errors may occur during commanded platform motion. During a mission such as an airborne survey, ongoing small attitude changes ordinarily associated with flight could result in essentially continous gradiometer platform slewing. In such a case jitter compensation would still be required.

A.3 CONCLUSIONS

Gyro-based gradiometer jitter compensation appears to be viable. Considerations such as gyro noise, bandwidth, and resolution are not serious issues. However, tests conducted to date by Bell indicate that resonances in the gradiometer structure may be a source of difficulty. Since Bell's findings apply to the large gas-bearing gradiometer model, future tests with the reduced-size ball-bearing gradiometer will be particularly instructive. The key question which remains to be answered is whether structural resonances of the gradiometer can be controlled at high mechanical frequencies (> 50 Hz).

APPENDIX B

MEASUREMENT EQUATIONS FOR AN IDEALIZED
BELL GRAVITY GRADIOMETER

B.1   INTRODUCTION

The Bell gradiometer consists of four accelerometers
mounted on a rotating platform. The axis of rotation is per-
pendicular to the sensitive axes of the accelerometers. The
orientation and reference frames to be used are depicted in
Fig. B.1-1.
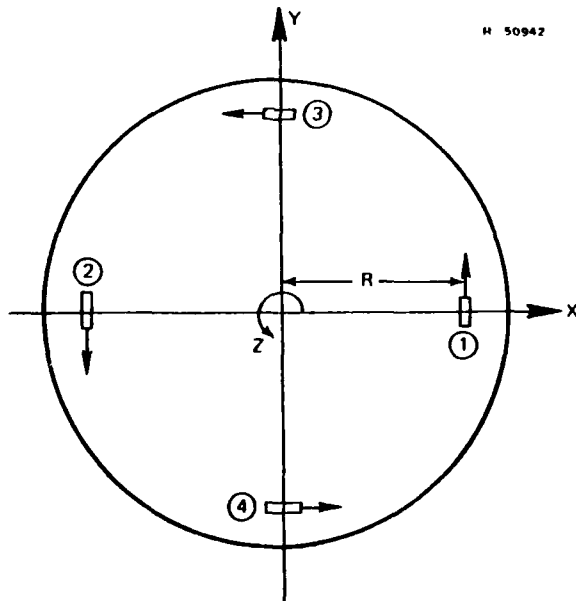
Figure B.1-1   Coordinate System for Gradiometer Analysis

In this diagram the axis of platform rotation is Z.
The constant rate of rotation is denoted by ω. The four spe-

cific forces sensed by the four accelerometers are combined into an overall measurement according to:

$$z = f_{s1} + f_{s2} - f_{s3} - f_{s4} \qquad (B.1\text{-}1)$$

where

$$f_{si} = \text{specific force from } i^{th} \text{ accelerometer.}$$

B.2   MEASUREMENT EQUATIONS

B.2.1   Linear Accelerations

Generally,

$$f_{si} = g_i - a_i \qquad (B.2\text{-}1)$$

where

g_i = component of gravity along i^{th} accelerometer sensitive axis

a_i = acceleration in the direction of the ith accelerometer sensitive axis

The basic process of interest is mathematically described by:

$$g_i = g_o + \Gamma \underline{r}_i \qquad (B.2\text{-}2)$$

That is, the gravity vector at the ith location (g_i) is described to first order by the sum of the gravity vector at the origin (g_o) plus the gravity gradient (Γ) times the position vector ($\underline{r}_i$).

The component of gravity sensed can be expressed as

$$g_i = c_i \, g_i \qquad \text{(B.2-3)}$$

where c_i is the appropriate matrix of elements to resolve g_i.

Combining all of the above yields:

$$z = c_1 \, (g_0 + \Gamma \underline{r}_1) - a_1 + c_2 \, (g_0 + \Gamma \underline{r}_2) - a_2 - c_3 \, (g_0 + \Gamma \underline{r}_3)$$
$$+ \, a_3 - c_4 \, (g_0 + \Gamma \underline{r}_4) + a_4 \qquad \text{(B.2-4)}$$

If the platform is stabilized in inertial space (even if it is translating),

$$\begin{aligned} a_1 &= -a_2 \\ a_3 &= -a_4 \end{aligned} \qquad \text{(B.2-5)}$$

making

$$z = c_1 \Gamma \underline{r}_1 + c_2 \Gamma \underline{r}_2 - c_3 \Gamma \underline{r}_3 - c_4 \Gamma \underline{r}_4 \qquad \text{(B.2-6)}$$

By direct calculation it can be shown that

$$\underline{r}_1 = -\underline{r}_2 = \begin{bmatrix} R \cos \omega t \\ R \sin \omega t \\ 0 \end{bmatrix} \qquad \text{(B.2-7))}$$

$$\underline{r}_3 = -\underline{r}_4 = \begin{bmatrix} -R \sin \omega t \\ R \cos \omega t \\ 0 \end{bmatrix} \qquad \text{(B.2-8)}$$

$$c_1 = -c_2 = |-\sin \omega t \quad \cos \omega t \quad 0| \tag{B.2-9}$$

$$c_3 = -c_4 = |-\cos \omega t \quad -\sin \omega t \quad 0| \tag{B.2-10}$$

The above four equations can be used to reduce Eq. B.2-6 to

$$z = 2c_1 \Gamma \underline{r}_1 - 2c_2 \Gamma \underline{r}_3 \tag{B.2-11}$$

Utilizing Eqs. B.2-7 and B.2-9 yields

$$c_1 \Gamma \underline{r}_1 = R[-\Gamma_{xx} \cos \omega t \sin \omega t + \Gamma_{xy} (\cos^2 \omega t - \sin^2 \omega t)$$
$$+ \Gamma_{yy} \cos \omega t \sin \omega t] \tag{B.2-12}$$

From Eqs. B.2-8 and B.2-10 it can be shown that

$$c_3 \Gamma \underline{r}_3 = -c_1 \Gamma \underline{r}_1 \tag{B.2-13}$$

Thus,

$$z = 4R \; |(\Gamma_{yy} - \Gamma_{xx}) \cos \omega t \sin \omega t + \Gamma_{xy}(\cos^2 \omega t - \sin^2 \omega t)| \tag{B.2-14}$$

Now, the following two identities:

$$\cos \omega t \; \sin \omega t = \frac{1}{2} \sin 2\omega t$$
$$\cos^2 \omega t - \sin^2 \omega t = \cos 2\omega t \tag{B.2-15}$$

yield

$$\boxed{z = 2R \; (\Gamma_{yy} - \Gamma_{xx}) \sin 2\omega t + 4R\Gamma_{xy} \cos 2\omega t} \tag{B.2-16}$$

This equation describes the measurement obtained from the Bell gradiometer when its spin axis is fixed with respect to inertial space.

B.2.2 Angular Velocities

If angular motion of the spin axis relative to inertial space is present, the inertia forces generated by this motion will be sensed by the accelerometers. For this analysis, let

$$f_{si} = c_i(\underline{g}_i - \underline{a}_i) \qquad (B.2-17)$$

where

$$\underline{a}_i = \underline{a}_o + \underline{\dot{\Omega}} \times \underline{r}_i + \underline{\Omega} \times \underline{\Omega} \times \underline{r}_i \qquad (B.2-18)$$

In this equation $\underline{\Omega}$ and $\underline{\dot{\Omega}}$ are the angular rates and accelerations of the proof mass of the ith accelerometer. Using a matrix notation for cross products,

$$f_{si} = c_i(\underline{g}_o + \Gamma \underline{r}_i - a_o - [\dot{\Omega}]\,\underline{r}_i - [\Omega]^2 \underline{r}_i) \qquad (B.2-19)$$

where

$$[\dot{\Omega}] = \begin{bmatrix} 0 & -\dot{\omega} & \dot{\Omega}_y \\ \dot{\omega} & 0 & -\dot{\Omega}_x \\ -\dot{\Omega}_y & \dot{\Omega}_x & 0 \end{bmatrix} \qquad (B.2-20)$$

$$[\Omega] = \begin{bmatrix} 0 & -\omega & \Omega_y \\ \omega & 0 & -\Omega_x \\ -\Omega_y & \Omega_x & 0 \end{bmatrix} \qquad (B.2-21)$$

$$[\Omega]^2 = \begin{bmatrix} -(\omega^2 + \Omega_y^2) & \Omega_y \Omega_x & \omega\Omega_x \\ \Omega_x \Omega_y & -(\omega^2 + \Omega_x^2) & \omega\Omega_y \\ \omega\Omega_x & \omega\Omega_y & -(\Omega_x^2 + \Omega_y^2) \end{bmatrix} \qquad (B.2-22)$$

and Ω_x, Ω_y are the components of angular velocity of the spin axis.

The overall system measurement given by Eq. B.2-11 now becomes

$$z = 2c_1(\Gamma - [\dot{\Omega}] - [\Omega]^2) \, \underline{r}_1 - 2c_3(\Gamma - [\dot{\Omega}] - [\Omega]^2) \, \underline{r}_3$$

(B.2-23)

which reduces to

$$\boxed{z = 2R \, (\Gamma_{yy} - \Gamma_{xx} + \Omega_x^2 - \Omega_y^2) \, \sin 2\omega t + 4R \, (\Gamma_{xy} - \Omega_y \Omega_x) \, \cos 2\omega t}$$

(B.2-24)

For the special case $\Omega_x \equiv \Omega_y \equiv 0$, this reduces to previous result in Eq. B.2-16.

APPENDIX C

DEFINITIONS OF KEY MATRICES IN THE ERROR MODEL
FOR AN AIRBORNE GRADIOMETRIC SURVEY SYSTEM

C.1   INTRODUCTION

This appendix contains two major sections. In the first is a derivation of the transformation that maps gradiometer-system output signals into the six distinct elements of the gravity gradient tensor. In the last section numerical values are given for the vibration sensitivity matrices in the gradiometer-system error model.

C.2   RECOVERY OF THE GRAVITY GRADIENT FROM GRADIOMETER-SYSTEM OUTPUTS

In keeping with the notation of Section 3.7, the six output functions of the gradiometer system are arranged in a vector

$$\underline{\Gamma}_o(t) = \begin{bmatrix} \Gamma_I^1(t) \\ \Gamma_C^1(t) \\ \Gamma_I^2(t) \\ \Gamma_C^2(t) \\ \Gamma_I^3(t) \\ \Gamma_C^3(t) \end{bmatrix} \qquad (C.2\text{-}1)$$

131

where the superscripts indicate the first, second, or third
gradiometer in the instrument triad, and the subscripts denote
inline or cross-channel measurements.

If the measurement system were free of errors, then
the output $\underline{\Gamma}_O(t)$ would equal an ideal measurement vector de-
noted $\underline{\Gamma}_{IM}(t)$, whose elements are specific linear combinations
of the gradient components sensed by the individual instru-
ments in the triad. The measurement vector $\underline{\Gamma}_{IM}(t)$ depends
both on the gravity field and the orientations of the three
gradiometers. To compute this measurement vector, let an x,
y, z rectangular coordinate system be chosen with the x axis
pointing east, the y axis pointing north, and the z axis point-
ing up. The gravity gradient at the center of the instrument
triad can then be represented by the matrix

$$\begin{bmatrix} \Gamma_{xx} & \Gamma_{xy} & \Gamma_{xz} \\ \Gamma_{yx} & \Gamma_{yy} & \Gamma_{yz} \\ \Gamma_{zx} & \Gamma_{zy} & \Gamma_{zz} \end{bmatrix} \tag{C.2-2}$$

where, e.g., $\Gamma_{xz} = \partial g_x/\partial z = \partial g_z/\partial x$, with g_x and g_z being the x
and z components of the gravity vector. The six distinct com-
ponents of this matrix* can be arranged in a column vector

$$\underline{\Gamma}(t) = \begin{bmatrix} \Gamma_{xx}(t) \\ \Gamma_{xy}(t) \\ \Gamma_{xz}(t) \\ \Gamma_{yy}(t) \\ \Gamma_{yz}(t) \\ \Gamma_{zz}(t) \end{bmatrix} \tag{C.2-3}$$

*Note that only five of the gradient elements are independent.
The inline gradients are related by $\Gamma_{xx} + \Gamma_{yy} + \Gamma_{zz} = 0$.

132

The particular orientations of the three gradiometers in the triad then uniquely determine a transformation matrix T that maps the gradient vector $\underline{\Gamma}(t)$ into the ideal measurement vector $\underline{\Gamma}_{IM}(t)$

$$\underline{\Gamma}_{IM}(t) = T\underline{\Gamma}(t) \qquad (C.2\text{-}4)$$

In the system error model of Section 3.7, the first gradiometer in the instrument triad is assumed to have a vertical spin axis, the second gradiometer has a south-pointing axis, while the third instrument's axis points east. The ideal measurement vector is then

$$\underline{\Gamma}_{IM}(t) = \begin{bmatrix} \dfrac{\Gamma_{yy}(t) - \Gamma_{xx}(t)}{2} \\[2ex] \Gamma_{xy}(t) \\[2ex] \dfrac{\Gamma_{zz}(t) - \Gamma_{xx}(t)}{2} \\[2ex] \Gamma_{xz}(t) \\[2ex] \dfrac{\Gamma_{zz}(t) - \Gamma_{yy}(t)}{2} \\[2ex] \Gamma_{yz}(t) \end{bmatrix} \qquad (C.2\text{-}5)$$

and the transformation matrix T is

$$T = \begin{bmatrix} -\frac{1}{2} & 0 & 0 & \frac{1}{2} & 0 & 0 \\ 0 & 1 & 0 & 0 & 0 & 0 \\ -\frac{1}{2} & 0 & 0 & 0 & 0 & \frac{1}{2} \\ 0 & 0 & 1 & 0 & 0 & 0 \\ 0 & 0 & 0 & -\frac{1}{2} & 0 & \frac{1}{2} \\ 0 & 0 & 0 & 0 & 1 & 0 \end{bmatrix} \qquad (C.2\text{-}6)$$

133

In practice, the outputs of the instrument triad (represented in the ideal case by $\Gamma_{IM}(t)$) are the observed quantities, and the gradient $\underline{\Gamma}(t)$ is to be computed from them. However, the transformation matrix T can not be inverted because it is singular; the sum of its first, fourth, and sixth columns is the zero vector. Therefore, to each ideal measurement vector $\underline{\Gamma}_{IM}$ in the range space of T, there exist an infinite number of gradient vectors $\underline{\Gamma}$ that satisfy $\underline{\Gamma}_{IM} = T\underline{\Gamma}$. However, only one of these $\underline{\Gamma}$ is admissable, namely that for which Laplace's equation for the gravity potential is satisfied.

$$\Gamma_{xx} + \Gamma_{yy} + \Gamma_{zz} = 0 \qquad (C.2-7)$$

Solving this equation for Γ_{zz} and substituting the result for Γ_{zz} in the expression for $\underline{\Gamma}_{IM}(t)$ yields

$$\underline{\Gamma}_{IM}(t) = \begin{bmatrix} \dfrac{\Gamma_{yy}(t) - \Gamma_{xx}(t)}{2} \\[2ex] \Gamma_{xy}(t) \\[2ex] \dfrac{-\Gamma_{yy}(t) - 2\Gamma_{xx}(t)}{2} \\[2ex] \Gamma_{xz}(t) \\[2ex] \dfrac{-\Gamma_{xx}(t) - 2\Gamma_{yy}(t)}{2} \\[2ex] \Gamma_{yz}(t) \end{bmatrix} \qquad (C.2-8)$$

Since $\Gamma_{zz}(t)$ no longer appears in $\underline{\Gamma}_{IM}(t)$, the ideal measurement vector can be computed from a reduced gradient vector $\underline{\Gamma}_R(t)$, which is obtained by deleting the $\Gamma_{zz}(t)$ component from $\underline{\Gamma}(t)$:

$$\underline{\Gamma}_R(t) = \begin{bmatrix} \Gamma_{xx}(t) \\ \Gamma_{xy}(t) \\ \Gamma_{xz}(t) \\ \Gamma_{yy}(t) \\ \Gamma_{yz}(t) \end{bmatrix} \qquad (C.2\text{-}9)$$

The corresponding reduced transformation matrix T_R satisfies $\underline{\Gamma}_{IM}(t) = T_R \underline{\Gamma}_R(t)$ and is given as

$$T_R = \begin{bmatrix} -\tfrac{1}{2} & 0 & 0 & \tfrac{1}{2} & 0 \\ 0 & 1 & 0 & 0 & 0 \\ -1 & 0 & 0 & -\tfrac{1}{2} & 0 \\ 0 & 0 & 1 & 0 & 0 \\ -\tfrac{1}{2} & 0 & 0 & -1 & 0 \\ 0 & 0 & 0 & 0 & 1 \end{bmatrix} \qquad (C.2\text{-}10)$$

The reduced transformation matrix T_R is also singular (because it is not square), but it has full column rank. Therefore, each ideal measurement $\underline{\Gamma}_{IM}(t)$ that satisfies $\underline{\Gamma}_{IM}(t) = T_R \underline{\Gamma}_R(t)$ corresponds to exactly one reduced gradient vector $\underline{\Gamma}_R(t)$. This unique vector can be computed as

$$\underline{\Gamma}_R(t) = T_R^{\#} \, \underline{\Gamma}_{IM}(t) \qquad (C.2\text{-}11)$$

where $T_R^{\#}$ is the pseudo inverse of T_R

$$T_R^{\#} = (T_R^T \, T_R)^{-1} \, T_R^T \qquad (C.2\text{-}12)$$

As a result, the full gradient vector

$$\underline{\Gamma}(t) = \begin{bmatrix} \Gamma_R(t) \\ \text{-------} \\ \Gamma_{zz}(t) \end{bmatrix} \qquad\qquad (C.2\text{-}13)$$

satisfies

$$\underline{\Gamma}(t) = T_o \underline{\Gamma}_{IM}(t) \qquad\qquad (C.2\text{-}14)$$

where the transformation matrix T_o is given by

$$T_o = \begin{bmatrix} (T_R^T T_R)^{-1} T_R^T \\ \text{--------------------------} \\ 0 \quad 0 \quad 2/3 \quad 0 \quad 2/3 \quad 0 \end{bmatrix} \qquad (C.2\text{-}15)$$

C.3 GRADIOMETER SYSTEM VIBRATION SENSITIVITIES

This section gives estimated numerical values for both the linear and angular vibration sensitivity matrices, $S_{LIN}(f_k)$ and $S_{ANG}(f_k)$, as defined in Section 3.7.7. These estimates are based on test data as summarized in Tables 3.3-1 and 3.4-1.

$S_{LIN}(f_k)$ is considered first. This 6 x 3 matrix of mean-square sensitivities to linear vibration depends on the vibration frequency $f_k = kf_s$, $k=0,1,2,3$, where the spin frequency $f_s \approx 0.28$ Hz. Equation 3.7-3 is used to associate a specific entry in Table 3.3-1 with each element of $S_{LIN}(f_k)$. The units of $S_{LIN}(f_k)$ are E^2/g^2; therefore, the entries in Table 3.3-1 are multiplied by 1000 mg/g and then squared. This yields

$$S^2_{LIN} (\|VSA, f_o) = 6.8 \times 10^4 \quad E^2/g^2$$

$$S^2_{LIN} (\|VSA, f_1) = 1.7 \times 10^4 \quad E^2/g^2$$

$$S^2_{LIN} (\|VSA, f_2) = 6.2 \times 10^5 \quad E^2/g^2 \qquad (C.3-1)$$

$$S^2_{LIN} (\|VSA, f_3) = 2.8 \times 10^6 \quad E^2/g^2$$

$$S^2_{LIN} (\perp VSA, f_o) = 2.1 \times 10^5 \quad E^2/g^2$$

$$S^2_{LIN} (\perp VSA, f_1) = 1.8 \times 10^7 \quad E^2/g^2$$

$$S^2_{LIN} (\perp VSA, f_2) = 2.4 \times 10^3 \quad E^2/g^2 \qquad (C.3-2)$$

$$S^2_{LIN} (\perp VSA, f_3) = 1.9 \times 10^7 \quad E^2/g^2$$

$$S^2_{LIN} (\|HSA, f_k) = S^2_{LIN} (\|VSA, f_k) \text{ for } k = 0,1,2,3 \quad (C.3-3)$$

$$S^2_{LIN} (\perp HSA, f_0) = 2.1 \times 10^5 \quad E^2/g^2$$

$$S^2_{LIN} (\perp HSA, f_1) = 6.6 \times 10^3 \quad E^2/g^2$$

$$S^2_{LIN} (\perp HSA, f_2) = 3.2 \times 10^5 \quad E^2/g^2 \qquad (C.3-4)$$

$$S^2_{LIN} (\perp HSA, f_3) = 1.4 \times 10^6 \quad E^2/g^2$$

The same procedure is used to determine numerical values for the elements of $S_{ANG}(f_k)$ in Eq. 3.7-15, except that Table 3.4-1 is used, and its scale factor of 10^4 must be taken into account. The results for $k=1,2,3,4$ are

137

$$S^2_{ANG} \, (\|VSA, f_1) = 8.5 \times 10^{-7} \quad E^2/(rad/s)^2$$

$$S^2_{ANG} \, (\|VSA, f_2) = 2.0 \times 10^{-7} \quad E^2/(rad/s)^2$$

$$S^2_{ANG} \, (\|VSA, f_3) = 6.9 \times 10^{-7} \quad E^2/(rad/s)^2 \qquad \text{(C.3-5)}$$

$$S^2_{ANG} \, (\|VSA, f_4) = 5.8 \times 10^{-7} \quad E^2/(rad/s)^2$$

$$S^2_{ANG} \, (\perp VSA, f_1) = 9.4 \times 10^{-7} \quad E^2/(rad/s)^2$$

$$S^2_{ANG} \, (\perp VSA, f_2) = 5.8 \times 10^{-8} \quad E^2/(rad/s)^2$$

$$S^2_{ANG} \, (\perp VSA, f_3) = 4.4 \times 10^{-5} \quad E^2/(rad/s)^2 \qquad \text{(C.3-6)}$$

$$S^2_{ANG} \, (\perp VSA, f_4) = 1.2 \times 10^{-5} \quad E^2/(rad/s)^2$$

$$S^2_{ANG} \, (\|HSA, f_k) = S^2_{ANG}(\|VSA, f_k) \text{ for } k=1,2,3,4 \qquad \text{(C.3-7)}$$

$$S^2_{ANG} \, (\perp HSA, f_k) = S^2_{ANG}(\perp VSA, f_k) \text{ for } k=1,2,3,4 \qquad \text{(C.3-8)}$$

APPENDIX D
INTENTIONAL GRADIOMETER PLATFORM MOTION

D.1   INTRODUCTION

Most studies of gradiometer/inertial platform mech-
anizations visualize a triad of gradiometers attached to the
inner element of a local-level gimballed platform. The ge-
ometry of the triad involves a symmetric distribution of the
three instruments about the vertical with each gradiometer
inclined at the same "umbrella" angle. This "conventionally-
mechanized" gradiometer is illustrated in Fig. D.1-1. Figure
D.1-1 also defines the gradiometer body axes u, v, and w and
the local-level coordinates x, y, z.

In the conventional mechanization, the platform's
inner element is held fixed about the two horizontal axes and
in azimuth.[*] However, as illustrated in the following, speci-
fic advantages can be gained by superimposing platform rota-
tion motions onto the nominal local-level platform orientation.
Such motions have the potential for decreasing the effective
noise of the gradiometer and reducing the number of gradiome-
ters needed for completely measuring the gradient tensor.
Several variations exist. The simplest is constant rate ro-
tation or "carouselling" about the vertical axis. Carousel-
ling is discussed in detail in Sections D.2 and D.3. The other
rotation concepts have similar, although more mathematically

---

[*]Azimuth wander mechanizations would also be suitable for
gradiometers.
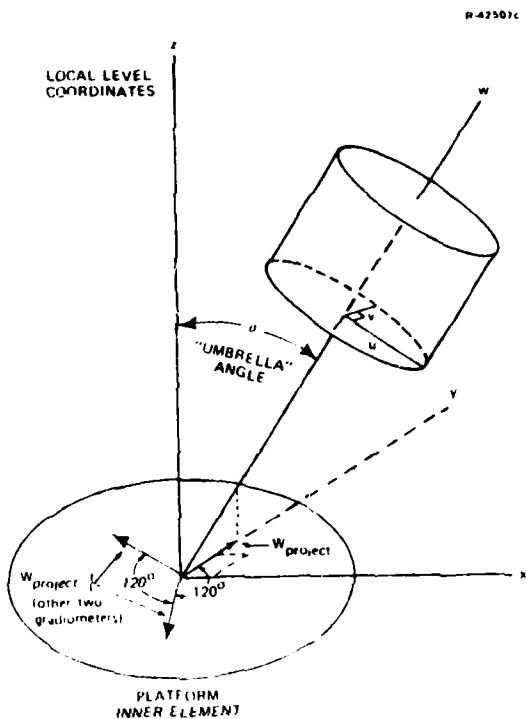
Figure D.1-1   Gradiometer Triad Element

involved, descriptions. Compound mechanizations involving tum-
ble or rocking motion of the platform (in addition to carousel-
ling) are treated in Section D.4. Section D.5 concludes with
a description of step-indexing, a discrete form of carouselling.

D.2   OUTPUT EQUATIONS FOR A SINGLE CAROUSEL-
       MECHANIZED GRADIOMETER

   D.2.1 Coordinate Transformations

       Three orthogonal coordinate frames are of interest:

(1) The u, v, w gradiometer body axes of Fig. D.1-1.

(2) A frame (x_1, y_1, z) associated with the (vertical) carousel axis (distinct from the gradiometer's internal spin or weights axis). The (x_1, y_1, z) frame rotates synchronously at the carousel rate.

(3) The frames (u, v, w) and (x_1, y_1, z) are both rotating. Let (x, y, z) be the fixed local-level frame which corresponds to (x_1, y_1, z) at a specified time.

Relations among the coordinates are summarized as follows:

Transformation Between Gradiometer Body Frame
and Carousel Frame (See Figure D.2-1)

$$u = x, \text{ (out of paper)}$$

$$\begin{pmatrix} x_1 \\ y_1 \\ z \end{pmatrix} = C_1^0 \begin{pmatrix} u \\ v \\ w \end{pmatrix}$$
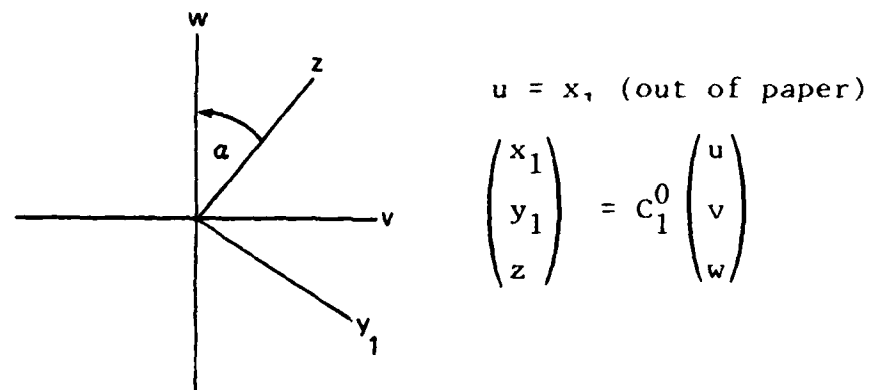
Figure D.2-1 Gradiometer Body Axes to Carousel Axes

The transformation C_1^0 is given by

$$C_1^0 = \begin{bmatrix} 1 & 0 & 0 \\ 0 & C\alpha & S\alpha \\ 0 & -S\alpha & C\alpha \end{bmatrix} \tag{D.2-1}$$

where the abbreviations C and S are used to indicate sine and cosine.

Transformation Between Carousel Frame and Fixed Frame

z is common (out of paper)

$B = \omega_p t$, ω_p = carousel rate

$$\begin{pmatrix} x \\ y \\ z \end{pmatrix} = C_2^1 \begin{pmatrix} x_1 \\ y_1 \\ z \end{pmatrix}$$
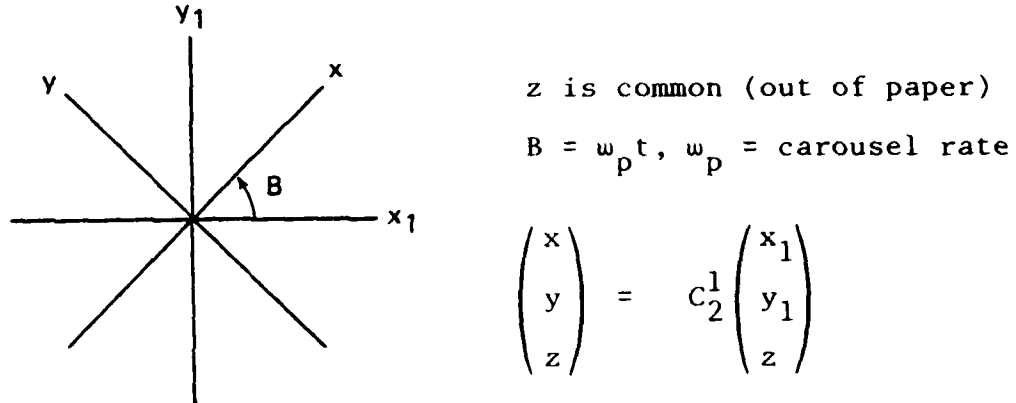
Figure D.2-2   Gradiometer Carousel Axes to Fixed Frame Axes

The transformation C_2^1 is

$$C_2^1 = \begin{bmatrix} CB & SB & 0 \\ -SB & CB & 0 \\ 0 & 0 & 1 \end{bmatrix} \qquad (D.2-2)$$

Combining Eqs. D.2-1 and D.2-2 the transformation C_2^0 is

$$C_2^0 = C_2^1 \, C_1^0 = \begin{bmatrix} CB & SBC\alpha & S\alpha SB \\ -SB & CBC\alpha & S\alpha CB \\ 0 & -S\alpha & C\alpha \end{bmatrix} \qquad (D.2-3)$$

The gradients in the fixed frame (x, y, z) are related to the gradients in the gradiometer's body frame (u, v, w) by

$$\Gamma_0 = C_0^2 \, \Gamma_2 \, C_2^0 \qquad (D.2-4)$$

142

where

$$c_0^2 = (c_2^0)^T \qquad\qquad (D.2-5)$$

and the gradient matrix is represented by

$$\Gamma_0 = \begin{bmatrix} \Gamma_{uu} & \Gamma_{uv} & \Gamma_{uw} \\ \Gamma_{vu} & \Gamma_{vv} & \Gamma_{vw} \\ \Gamma_{wu} & \Gamma_{wv} & \Gamma_{ww} \end{bmatrix} \qquad\qquad (D.2-6)$$

The superscript T indicates matrix transpose.

D.2.2 Bell Gradiometer

A single rotating accelerometer gradiometer provides the two measurements[*]

$$m_{1B} = \Gamma_{uu} - \Gamma_{vv} \qquad\qquad (D.2-7)$$

$$M_{2B} = \Gamma_{uv} \qquad\qquad (D.2-8)$$

When the expression indicated in (D.2-4) is evaluated and substituted into (D.2-7) and (D.2-8), the following output equations of a single gradiometer are obtained after taking advantage of several trigonometric identities.

$$m_{1B} = (C^2B - C^2\alpha\, S^2B)\Gamma_{xx} + (S^2B - C^2\alpha C^2B)\Gamma_{yy} - S^2\alpha\Gamma_{zz}$$

$$- (1+C^2\alpha)\, S2B\Gamma_{xy} + S2\alpha SB\Gamma_{xz} + S2\alpha CB\Gamma_{yz} \qquad (D.2-9)$$

---

[*]In practice, the gradiometer outputs are modulated by the instrument block's spin frequency (~1/4 Hz). In this development the gradient-signal and carousel-carrier frequencies being considered are much lower than the gradiometer spin rate. Hence, it is appropriate to avoid the additional complexity of the extra spin frequency terms.

$$m_{2B} = \frac{1}{2} C\alpha S2B\Gamma_{xx} - \frac{1}{2} C\alpha S2B\Gamma_{yy} + C\alpha C2B\Gamma_{xy} - S\alpha CB\Gamma_{xz} + S\alpha SB\Gamma_{yz}$$

(D.2-10)

It is useful to express the two measurements in terms of their components at zero frequency and quadrature components at ω_p and $2\omega_p$.

$$m_{1B} = m_0^{1B} + m_{C1}^{1B} + m_{S1}^{1B} + m_{C2}^{1B} + m_{S2}^{1B}$$

(D.2-11)

$$m_{2B} = m_0^{2B} + m_{C1}^{2B} + m_{S1}^{2B} + m_{C2}^{2B} + m_{S2}^{2B}$$

(D.2-12)

Each frequency component is given by

$$m_0^{1B} = -\frac{3}{2} \Gamma_{zz} \sin^2 \alpha$$

(D.2-13)

$$m_{C1}^{1B} = \Gamma_{yz} \sin 2\alpha \cos \omega_p t$$

(D.2-14)

$$m_{S1}^{1B} = \Gamma_{xz} \sin 2\alpha \sin \omega_p t$$

(D.2-15)

$$m_{C2}^{1B} = \frac{1}{2}(\Gamma_{xx} - \Gamma_{yy})(1 + \cos^2 \alpha)\cos 2\omega_p t$$

(D.2-16)

$$m_{S2}^{1B} = -\Gamma_{xy}(1 + \cos^2 \alpha) \sin 2\omega_p t$$

(D.2-17)

$$m_0^{2B} = 0$$

(D.2-18)

$$m_{C1}^{2B} = -\Gamma_{xz} \sin \alpha \cos \omega_p t$$

(D.2-19)

$$m_{S1}^{2B} = \Gamma_{yz} \sin \alpha \sin \omega_p t$$

(D.2-20)

$$m_{C2}^{2B} = \Gamma_{xy} \cos \alpha \cos 2\omega_p t$$

(D.2-21)

$$m_{S2}^{2B} = \frac{1}{2}(\Gamma_{xx} - \Gamma_{yy}) \cos \alpha \sin 2\omega_p t$$

(D.2-22)

where Laplace's equation

$$\Gamma_{xx} + \Gamma_{yy} + \Gamma_{zz} = 0 \qquad (D.2\text{-}23)$$

has been used to simplify (D.2-13).

D.2.3 Draper Gradiometer

A single floated gradiometer provides the two measurements

$$m_{1D} = \Gamma_{vw} \qquad (D.2\text{-}24)$$

$$m_{2D} = \Gamma_{uw} \qquad (D.2\text{-}25)$$

Following the same procedure as in the previous section

$$m_{1D} = S\alpha C\alpha S^2 B\Gamma_{xx} + S\alpha C\alpha SBCB\Gamma_{xy} - S^2\alpha SB\Gamma_{zx} + S\alpha C\alpha SBCB\Gamma_{xy}$$

$$+ S\alpha C\alpha C^2 B\Gamma_{yy} - S^2\alpha CB\Gamma_{yz} + C^2\alpha SB\Gamma_{xz} + C^2\alpha CB\Gamma_{yz}$$

$$- S\alpha C\alpha \Gamma_{zz} \qquad (D.2\text{-}26)$$

$$m_{2D} = S\alpha SBCB\Gamma_{xx} - S\alpha S^2 B\Gamma_{yx} + S\alpha C^2 B\Gamma_{xy} - S\alpha SBCB\Gamma_{yy}$$

$$+ C\alpha CB\Gamma_{xz} - C\alpha SB\Gamma_{yz} \qquad (D.2\text{-}27)$$

The individual frequency components, defined in the same fashion as (D.2-11) and (D.2-12), are

$$m_0^{1D} = - \frac{3}{4} \Gamma_{zz} \sin 2\alpha \qquad (D.2\text{-}28)$$

$$m_{C1}^{1D} = \Gamma_{yz} \cos 2\alpha \cos \omega_p t \qquad (D.2\text{-}29)$$

$$m_{S1}^{1D} = \Gamma_{xz} \cos 2\alpha \sin \omega_p t \qquad (D.2\text{-}30)$$

$$m_{C2}^{1D} = - \frac{1}{4}(\Gamma_{xx} - \Gamma_{yy}) \sin 2\alpha \cos 2\omega_p t \qquad (D.2\text{-}31)$$

145

$$m_{S2}^{1D} = \frac{1}{2} \Gamma_{xy} \sin 2\alpha \sin 2\omega_p t \qquad \text{(D.2-32)}$$

$$M_0^{2D} = 0 \qquad \text{(D.2-33)}$$

$$m_{C1}^{2D} = \Gamma_{xz} \cos \alpha \cos \omega_p t \qquad \text{(D.2-34)}$$

$$m_{S1}^{2D} = -\Gamma_{yz} \cos \alpha \sin \omega_p t \qquad \text{(D.2-35)}$$

$$m_{C2}^{2D} = \Gamma_{xy} \sin \alpha \cos 2\omega_p t \qquad \text{(D.2-36)}$$

$$m_{S2}^{2D} = \frac{1}{2}(\Gamma_{xx} - \Gamma_{zz}) \sin \alpha \sin 2\omega_p t \qquad \text{(D.2-37)}$$

Again the Laplace relation (D.2-23) has been used in obtaining (D.2-28).

D.3   DISCUSSION

D.3.1 Signal Recovery

From equations (D.2-13) through (D.2-17) it is evident that the gradiometer's inline channel (m_1) provides independent amplitude-modulated outputs containing all of the information required to specify the gravity gradient tensor. The gradiometer's cross channel provides only four independent elements of tensor information; they are (with the exception of Γ_{zz}) the same as provided by the inline channel. However, the cross channel outputs have a different scale factor dependency on the umbrella angle, α. As a result, for certain values of α, the cross channel measurements cease to be completely redundant with the inline measurements. Such a situation is discussed in Section D.3.2. A similar case holds for the two outputs of the Draper gradiometer. Note that the output equation terms for a carouseled Bell gradiometer [(D.2-13)

146

through (D.2-22)| provide the same information as those for a
carouseled Draper gradiometer |(D.2-28) through (D.2-32)|.
Only the scale factors differ.

It is interesting to note the effects of orienting a
carousel axis in a direction other than vertical. Although
the equations associated with the additional angular degree of
freedom are not reproduced here, the following findings are
st? ed.

- The zero-frequency (i.e., unmodulated)
  element is the gravity gradient defined
  by the carousel axis

- Sufficient information is available from
  a single gradiometer instrument to specify
  the complete gradient tensor in any coor-
  dinate frame (subject to the demodulation
  constraints discussed in Section D.3.4)

- Simultaneous carouselling of three gradi-
  ometers on a common platform poses no
  theoretical difficulty. Each gradiometer
  provides a set of independent outputs of
  the form D.2-9 and D.2-10 or D.2-26 and
  D.2-27.

D.3.2 Number of Gradiometers Required for Tensor Recovery

If the carousel frequency, ω_p, is sufficiently high,[*]
then the gradient signals of Eqs. (D.2-9) and (D.2-10) or (D.2-26)
and (D.2-27) can be recovered by conventional demodulation tech-
niques. The five independently recoverable signals provided
by a carouselled gradiometer, together with Laplace's equation,
completely specify the gravity gradient tensor. Thus, in prin-
ciple, only a single instrument (instead of a triad) is required
to provide a full set of gradient measurements.

----

[*]Criteria for selection of ω_p are discussed at further length
in Section D.3.4.

It is interesting to observe the simplified form which the demodulated output equations of a Bell gradiometer take when the umbrella angle is horizontal ($\alpha = 90°$).[*] They are summarized below.

$$m_0^{1B} \to \Gamma_{zz} \qquad\qquad m_0^{2B} \to 0$$

$$m_{C1}^{1B} \to \Gamma_{yz} \qquad\qquad m_{C1}^{2B} \to \Gamma_{xz}$$

$$m_{S1}^{1B} \to \Gamma_{xz} \qquad\qquad m_{S1}^{2B} \to \Gamma_{yz}$$

$$m_{C2}^{1B} \to \Gamma_{xx} - \Gamma_{yy} \qquad\qquad m_{C2}^{2B} \to 0$$

$$m_{S2}^{1B} \to \Gamma_{xy} \qquad\qquad m_{S2}^{2B} \to 0$$

The scale factors of the output terms also simplify and only two redundant terms remain in the cross channel signal. Such a configuration could ultimately be attractive in a carousel-mechanized system.

D.3.3 Noise Reduction

The frequency content of gradiometer self-noise is treated extensively in the main section of this report. For missions requiring gradient recovery at frequencies below about 0.1 mHz the instrument noise at low frequencies (red noise) can impose significant performance limitations. The potential advantage of carouseling in reducing low-frequency noise can be seen if the carousel rate, ω_p, is selected to lie above the red-noise frequency range of the gradiometer's error spectrum,

---

[*] A similar degenerate form occurs for the Draper gradiometer equations. However, the carousel orientation having the axis of weights horizontal is of less interest for the Draper instrument because the Γ_{zz} term becomes unobservable.

(e.g., $\omega_p > 0.6$ mrad/s). When the signal is lowpass demodulated, the only gradiometer errors which remain in the output are those originally within a narrow band[*] about ω_p. Thus, from the carouselled gradiometer output equations,[†] it is apparent that the red noise can be suppressed in all of the gradient elements except Γ_{zz}.

No direct improvement in Γ_{zz} occurs because it is unmodulated by the carousel action. Note that, while low-frequency gradiometer errors are not eliminated from Γ_{zz}, some improvement occurs by virtue of the improvement in the $(\Gamma_{xx} - \Gamma_{yy})$ term. This results because $(\Gamma_{xx} - \Gamma_{yy})$, in combination with Laplace's equation, is used to recover Γ_{zz}. However, the inability of carouselling to eliminate the majority of the red noise from Γ_{zz} (and, as a result, from the other two inline gradients) is a deficiency. Extensions which allow the Γ_{zz} term to be modulated also are discussed in Section D.4.

Note that these comments still apply if more than one gradiometer is carouselled on the same platform. Regardless of the orientation of any additional gradiometers, there is still no motion of any instruments in the z direction (carousel axis). Thus there is no basis for modulation of Γ_{zz}. Of course, the addition of instruments is always advantageous due to the reduction of noise inherent with the averaging of separate instrument outputs.

---

*This conceptual discussion omits important gradiometer signal bandwidth considerations. These are taken up in the next section.

†Equations D.2-13 through D.2-22 (Bell) and D.2-28 through D.2-32 (Draper).

D.3.4 Carousel Speed and Output Bandwidth Considerations

Two benefits from carouselling a gradiometer have been identified, namely the capability to recover the gravity gradient tensor with a single gradiometer instrument (instead of a triad) and low-frequency noise reduction. This section examines some of the different carousel-speed and operating-bandwidth constraints associated with each.

To utilize a single gradiometer for recovery of all of the tensor elements, the carousel frequency, w_p, must be somewhat larger than the highest frequency contained in the gradient signal, w_{co}. Otherwise information loss results. This is illustrated in Fig. D.3-1 for the case where the band-width of the gradient is slightly less than w_p. Note that Fig. D.3-1 depicts the process of amplitude modulation and demodulation with w_p as the carrier. The low-frequency noise suppression inherent in this process is also illustrated. Note also that if the carousel frequency is less than w_{co}, the distinct lobes shown in Fig. D.3-1 overlap. In this situation, if the lowpass filter were set to pass all frequencies up to w_{co}, error would result from the sideband overlap. On the other hand, if the filter bandwidth were reduced to omit the overlap region from the output, the high-frequency portion of the signal w   l be lost.

The value of w_{co} depends on the nature (e.g., rough or smooth) of the local gravity field and the speed of the gradiometer's host vehicle. A rule of thumb is to consider the cutoff wavelength of the earth's field to be 10 km. Then, the minimum carousel frequency which meets the criterion that w_p w_{co} is given by

$$w_p \, > \, \frac{\pi v}{5}$$

(D.3-1)

TIME SIGNAL	FREQUENCY SIGNAL
a. GRADIENT ELEMENT $\Gamma(t)$	
b. MODULATING SIGNAL $m(t) = \cos \omega_p t$	
c. MODULATED GRADIENT SIGNAL $\Gamma(t) \cos \omega_p t$	
d. DEMODULATION $\cos \omega_p t \, [\Gamma(t) \cos \omega_p t]$	
e. LOW PASS FILTER CHARACTERISTIC $f(t)$	
f. RECOVERED GRADIENT $f(t) \cdot \{\cos \omega_p t \, [\Gamma(t)\cos \omega_p t]\}$	
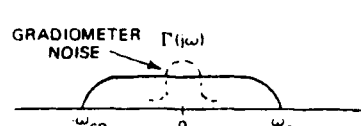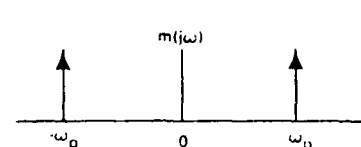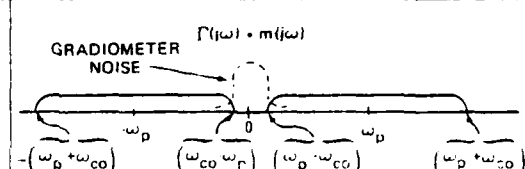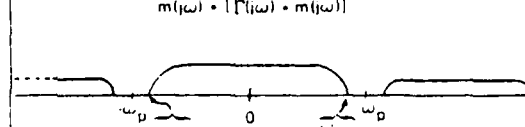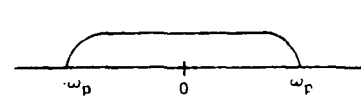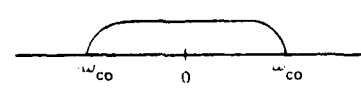
· DENOTES CONVOLUTION

Figure D.3-1   Illustration of Lowest Carousel Rate Which Avoids Signal Loss

151

where ω_p is given in rad/s and v is in km/s. For a slow-speed vehicle such as an ocean vessel moving at 2 m/s (3.9 kts), the minimum carousel frequency evaluates to 0.72 cycle per hour.

For a rapidly moving vehicle such as an aircraft traveling at 150 m/s (291 kts), the minimum value of the carousel rate works out to 0.9 cycles per minute.[*] As seen later this value is significantly beyond practical limits.

If multiple gradiometers (e.g., a triad) are carouseled, the value of ω_p required to effect low frequency noise reduction is much lower. This can be illustrated by considering a single quadrature component of the output of one carouselled gradiometer, e.g.,

$$S_1(t) = \Gamma(t) \cos \omega_p t \qquad (D.3-2)$$

where $\Gamma(t)$ is the gradient element measured by that component. The output of a neighboring gradiometer, aligned at an angle ϕ with respect to the first is given by

$$S_2(t) = \Gamma(t) \cos (\omega_p t + \phi) \qquad (D.3-3)$$

With both $S_1(t)$ and $S_2(t)$ available, the following process illustrates the recovery of $\Gamma(t)$ at frequencies well beyond ω_p.

If the first signal (Eq. D.3-2) is divided by $\cos \omega_p t$ at points other than the zeros of the cosine function, the piecewise function

---

[*] In practice, for an aircraft flying at high altitude, a lower value of ω_p would be permissible, since the upward continued gradient field would cut off at a longer wavelength than 10 km.

$$S_1^D (t) = \frac{S_1(t)}{\cos \omega_p t} \qquad \omega_p t \neq n\pi, \ n=0,1,2 \ldots \qquad (D.3\text{-}4)$$

results. A similar division is carried out for the second
signal (Eq. D.3-3).

$$S_2^D (t) = \frac{S_2(t)}{\cos(\omega_p t + \phi)} \qquad (\omega_p t + \phi) \neq n\pi, \ n=0,1,2 \ldots \qquad (D.3\text{-}5)$$

Of course, in an actual implementation, the gaps would be of
finite width due to noise, quantization, etc. The multiple
gradiometer demodulation process is shown in Fig. D.3-2 where
the gap width is, for illustration purposes, indicated as 90°.
Also, for simplicity, the figure illustrates the case where
the phase angle, ϕ, is also 90 degrees. In practice, the right-
angle gradiometer arrangement would be adverse to demodulation
of the $2\omega_p$ signals. It is use here only for illustrative con-
venience. In fact a gradiometer triad as illustrated in Fig.
D.1-1 is the appropriate geometry.

For purposes of examining the frequency effects of the
demodulating process described in the previous paragraph, it
is useful to generalize Eqs. D.3-4 and D.3-5 as finite pulse-
width samplings of the modulated signal. Analysis, not pro-
vided here, shows that the piecewise demodulated signals are
subject to edge errors which degrade the recovered gradient
signal. This effect becomes severe only at signal frequencies
substantially beyond the carousel frequency and can be miti-
gated somewhat by the use of a tapered window to perform the
pulse sampling.

An alternative technique for demodulating $S_1(t)$ and
$S_2(t)$ is to formulate the demodulated signal as the output of
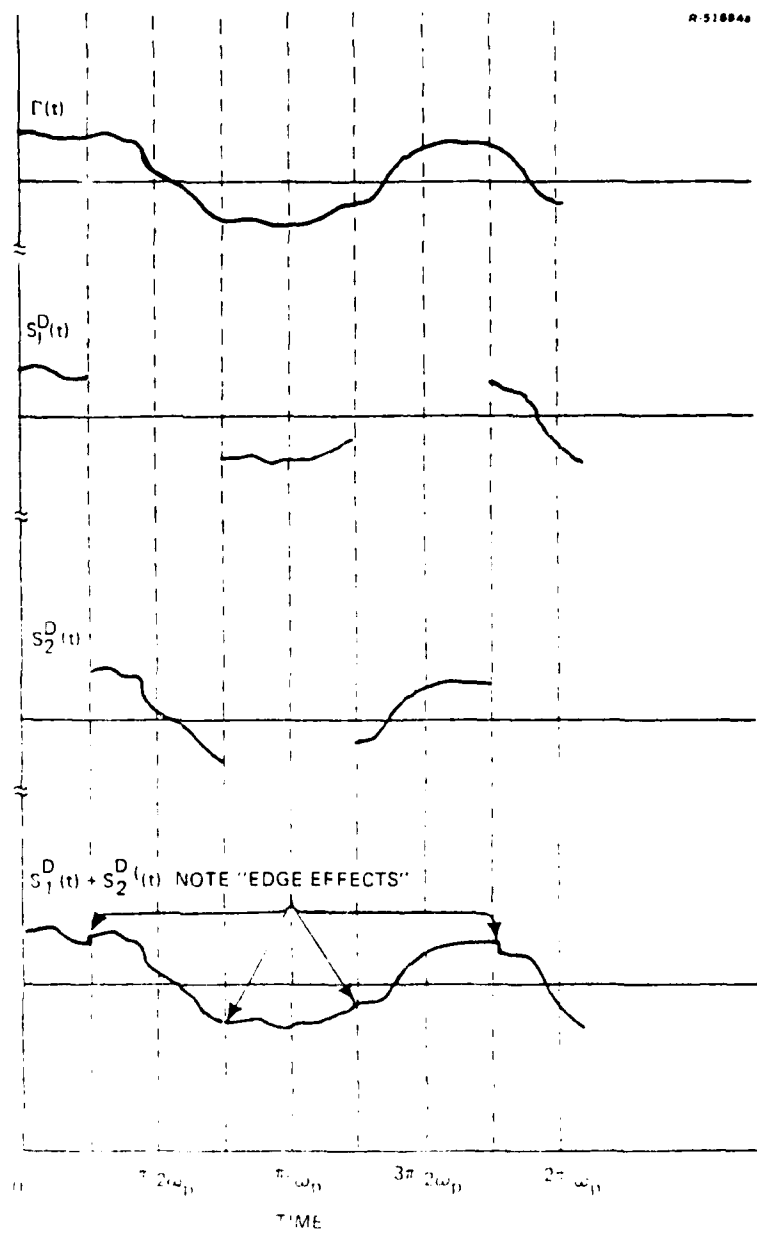
Figure D.3-2   Reconstruction of Gradient Signal

a Kalman filter estimator. In this case the observation equations (time varying) contain the modulation frequency and requisite statistical models for the gradient signal and gradiometer noise processes. As with the conventional filter technique, the Kalman approach has a high error sensitivity to signal content at frequencies which are considerably beyond the carousel frequency. This motivates as high a carousel rate as possible.

D.3.5 Error Sources Limiting Carousel Rates

The chief limitation[*] on carousel rates is the centrifugal gradient field which the carousel motion induces. The dynamic range of current gradiometer instruments is of the order of 10^4 E. The gradiometer bias induced by ω_p (measured in rad/s) is given by

$$\Gamma_\varepsilon = \omega_p^2 \times 10^9 \ E \qquad\qquad (D\text{-}3.6)$$

For the case of a bias offset of 2×10^4 E (i.e., twice the instrument's dynamic range), the corresponding carousel rate is 2.6 cycles/hour. To maintain a bias stability error of less than 1 E, the bias offset setting is required to be stable to 50 parts per million (ppm). Similarly, to maintain an inertial gradient field constant to 1 E, the carousel speed control is required to hold a constant rate within 25 ppm. These figures suggest that implementing continuous carousel speeds higher than about 3 cycles/hour would prove formidable.

If the 2.6 cycles/hour figure is considered to be a maximum feasible carousel rate, it is of interest to estimate

---

[*]An approach for removing this limitation is discussed in Section D.5.

155

the highest vehicle velocity consistent with single gradiometer (vs a triad) operation and recovery of the complete gradient tensor. Solving Eq. D.3-1 for v yields the value 7.1 m/s. This suggests that the use of a single carouselled gradiometer instead of a full triad on board an aircraft is well beyond the state of the art.

D.4   GENERALIZATIONS OF CAROUSEL MOTION

In Section D.3 it was observed that carouselling provides no modulation of the gradient tensor element defined by the carousel axis. As a result low-frequency gradiometer noise continues to be a major error source for inline gradients (for the gradient tensor expressed in the reference frame of the carousel motion). For obliquely defined frames, all of the gradient elements can contain significant amounts of the gradiometer's red noise. The techniques discussed in this section are directed toward implementing intentional platform motion which provides a suitable modulating signal on the carousel-axis gradient.

D.4.1 Tumble Motion

If, in addition to carouselling, constant-rate rotation of the gradiometer platform is implemented about an axis orthogonal to the carousel axis, the desired additional modulation is effected. The generalization of the carousel rate output equations of Section D.2 to include the effects of tumble motion proceeds similarly to the derivation of that section. For the umbrella angle, α, given by

$$\alpha = \omega_t t \qquad\qquad (D.4-1)$$

where ω_t is the tumble rate, the outputs equations for the inline channel of a carousel and tumble mechanized Bell gradiometer are

$$m_{DC}^{1B} = -\frac{3}{4}\, \Gamma_{zz} \tag{D.4-2}$$

$$m_{C2\omega_t}^{1B} = \frac{3}{4}\, \Gamma_{zz}\, \cos 2\omega_t t \tag{D.4-3}$$

$$m_{C2\omega_p}^{1B} = \frac{3}{4}\, (\Gamma_{xx} - \Gamma_{yz})\, \cos 2\omega_p t \tag{D.4-4}$$

$$m_{S2\omega_p}^{1B} = -\frac{3}{2}\, \Gamma_{xy}\, \sin 2\omega_p t \tag{D.4-5}$$

$$m_{C(2\omega_t + \omega_p)}^{1B} = -\frac{1}{2}\, \Gamma_{xz}\, \cos (2\omega_t + \omega_p) t \tag{D.4-6}$$

$$m_{S(2\omega_t + \omega_p)}^{1B} = \frac{1}{2}\, \Gamma_{yz}\, \sin (2\omega_t + \omega_p) t \tag{D.4-7}$$

$$m_{C(2\omega_t - \omega_p)}^{1B} = \frac{1}{2}\, \Gamma_{xz}\, \cos (2\omega_t - \omega_p) t \tag{D.4-8}$$

$$m_{S(2\omega_t - \omega_p)}^{1B} = -\frac{1}{2}\, \Gamma_{yz}\, \sin (2\omega_t - \omega_p) t \tag{D.4-9}$$

$$m_{C2(\omega_t + \omega_p)}^{1B} = \frac{1}{8}\, (\Gamma_{xx} - \Gamma_{yy})\, \cos 2(\omega_t + \omega_p) t \tag{D.4-10}$$

$$m_{S2(\omega_t + \omega_p)}^{1B} = -\frac{1}{4}\, \Gamma_{xy}\, \sin 2(\omega_t + \omega_p) t \tag{D.4-11}$$

$$m_{C2(\omega_t - \omega_p)}^{1B} = \frac{1}{8}\, (\Gamma_{xx} - \Gamma_{yy})\, \cos 2(\omega_t - \omega_p) t \tag{D.4-12}$$

$$m_{S2(\omega_t - \omega_p)}^{1B} = \frac{1}{4}\, \Gamma_{xy}\, \sin 2(\omega_t - \omega_p) t \tag{D.4-13}$$

where the quadrature terms for each frequency sum to provide the total inline output in the same fashion as Eq. D.2-11. As before the m superscript 1 identifies the inline channel output and B designates that the measurement is associated with the

157

Bell gradiometer. The subscripts indicate the specific quadrature component involved.

For the cross channel a different set of frequency components is obtained.

$$m^{2B}_{C(\omega_t+\omega_p)} = -\frac{\Gamma_{yz}}{2} \cos (\omega_t+\omega_p)t \qquad (D.4\text{-}14)$$

$$m^{2B}_{S(\omega_t+\omega_p)} = -\frac{\Gamma_{yz}}{2} \sin (\omega_t+\omega_p)t \qquad (D.4\text{-}15)$$

$$m^{2B}_{C(\omega_t-\omega_p)} = \frac{\Gamma_{yz}}{2} \cos (\omega_t-\omega_p)t \qquad (D.4\text{-}16)$$

$$m^{2B}_{S(\omega_t-\omega_p)} = \frac{\Gamma_{xz}}{2} \sin (\omega_t-\omega_p)t \qquad (D.4\text{-}17)$$

$$m^{2B}_{C(\omega_t+2\omega_p)} = \frac{\Gamma_{xy}}{2} \cos (\omega_t-\omega_p)t \qquad (D.4\text{-}18)$$

$$m^{2B}_{S(\omega_t+2\omega_p)} = \frac{1}{4} (\Gamma_{xx}-\Gamma_{yy}) \sin (\omega_t+2\omega_p)t \qquad (D.4\text{-}19)$$

$$m^{2B}_{C(\omega_t-2\omega_p)} = \frac{\Gamma_{xy}}{2} \cos (\omega_t-2\omega_p)t \qquad (D.4\text{-}20)$$

$$m^{2B}_{S(\omega_t-2\omega_p)} = \frac{1}{4} (\Gamma_{xx}-\Gamma_{yy}) \sin (\omega_t-2\omega_p)t \qquad (D.4\text{-}21)$$

Note that while the inline-channel outputs alone are sufficient to completely specify the entire gradient tensor if ω_t and ω_p are not harmonically related, the cross-channel terms are not. This is not surprising since it also occurs for carousel motion alone. However all of the distinct frequency signals yield a richness of redundant information which provides, in addition to the desired modulation of Γ_{zz}, the extra capability for noise reduction by averaging.

Unfortunately the tumble mechanization is not practical for current gradiometer instruments because of the time varying stresses induced by the earth's gravity field. However, key elements of it are retained in the platform rock mechanization discussed in the next section.

D.4.2 Platform Rock Motion

To reduce the adverse gravity-induced effects associated with tumbling the gradiometer, consider low-amplitude platform rocking about the nominal umbrella angle, α_o. The motion is given by

$$\alpha(t) = \alpha_o + \alpha_r \sin \omega_r t \qquad (D.4-22)$$

where α_r is the rocking amplitude and ω_r is the rocking rate. The rocking motion introduces frequency modulation of the gradiometer outputs as a result of terms of the form $\sin(\alpha_r \sin \omega_r t)$. Expansion of the inline-channel equations for the Bell gradiometer and the use of suitable trigonometric identities provides the following frequency and phase-separable terms. The notation is defined in the same fashion as earlier.

$$m_{DC}^{1B} = \frac{\Gamma_{zz}}{2}$$

$$m_{C2n\omega_r}^{1B} = -\Gamma_{zz} \cos 2\alpha_o \left[J_o(2\alpha_r) + 2 \sum_{n=1}^{\infty} J_{2n}(2\alpha_r) \cos 2n\omega_r t \right]$$
$$(D.4-23)$$

$$m_{S(2n+1)\omega_r}^{1B} = 2\Gamma_{zz} \sin 2\alpha_o \sum_{n=o}^{\infty} J_{2n+1}(2\alpha_r) \sin(2n+1)\omega_r t$$
$$(D.4-24)$$

$$m_{C(\omega_p \pm 2n\omega_r)}^{1B} = \Gamma_{xz} \sin 2\alpha_o \left\{ J_o(2\alpha_r) \cos \omega_p t \right.$$

$$+ \sum_{n=1}^{\infty} J_{2n}(2\alpha_r) [\cos (\omega_p + 2n\omega_r)t$$

$$\left. + \cos (\omega_p - 2n\omega_r)t] \right\} \tag{D.4-25}$$

$$m_{S[\omega_p \pm (2n+1)\omega_r]}^{1B} = \Gamma_{xz} \cos 2\alpha_o \left\{ \sum_{n=0}^{\infty} J_{2n+1}(2\alpha_r) [\sin(\omega_p + (2n+1)\omega_r)t \right.$$

$$\left. - \sin (\omega_p - (2n+1)\omega_r)t] \right\} \tag{D.4-26}$$

$$m_{C[\omega_p \pm (2n+1)\omega_r]}^{1B} = \Gamma_{yz} \cos 2\alpha_o \sum_{n=0}^{\infty} J_{2n+1}(2\alpha_r) [\cos(\omega_p + (2n+1)\delta_r)t$$

$$- \cos (\omega_p - (2n+1)\omega_r)t] \tag{D.4-27}$$

$$m_{S(\omega_p \pm 2n\omega_r)}^{1B} = \Gamma_{yz} \sin 2\alpha_o \left\{ J_o(2\alpha_r) \sin \omega_p t \right.$$

$$+ \sum_{n=1}^{\infty} J_{2n}(2\alpha_r) [\sin (\omega_p + 2n\omega_r)t + \sin (\omega_p - 2n\omega_r)t] \right\} \tag{D.4-28}$$

$$m_{C(2\omega_p \pm 2n\omega_r)}^{1B} = \frac{1}{4} (\Gamma_{xx} - \Gamma_{yy}) \left\{ (1 + J_o(2\alpha_r) \cos 2\alpha_o) \cos 2\omega_p t \right.$$

$$+ \sum_{n=1}^{\infty} J_{2n}(2\alpha_r) [\cos 2(\omega_p + n\omega_r)t$$

$$\left. + \cos 2(\omega_p - n\omega_r)t] \right\} \tag{D.4-29}$$

$$m_{S[2\omega_p \pm (2n+1)\omega_r]}^{1B} = \frac{1}{4} (\Gamma_{xx} - \Gamma_{yy}) \left\{ \sin 2\alpha_o \sum_{n=0}^{\infty} J_{2n+1}(2\alpha_r) \right.$$

$$\left. [\sin(2\omega_p + (2n+1)\omega_r)t - \sin (2\omega_p - (2n+1)\omega_r)t] \right\} \tag{D.4-30}$$

$$m_{C[2\omega_p \pm (2n+1)\omega_r]}^{1B} = -\frac{1}{2}\Gamma_{xy}\left\{\sin 2\alpha_o \sum_{n=0}^{\infty} J_{2n+1}(2\alpha_r)\right.$$

$$\left[\cos\,(2\omega_p + (2n+1)\omega_r)t - \cos\,(2\omega_p - (2n+1)\omega_r)t]\right\}$$

(D.4-31)

$$m_{S(2\omega_p \pm 2n\omega_r)}^{1B} = -\frac{1}{2}\Gamma_{xy}\left\{(1 + J_o(2\alpha_r)\cos 2\alpha_o)\sin 2\omega_p t\right.$$

$$\left. + \sum_{n=1}^{\infty} J_{2n}(2\alpha_r)[\sin 2(\omega_p + n\omega_r)t + \sin 2(\omega_p - n\omega_r)t]\right\}$$

(D.4-32)

where $J_n(2\alpha_r)$ is the Bessel function of the first kind, order n. A similar set of equations occurs when the Draper gradiometer is rock mechanized.

Note that there is sufficient information, separated in frequency,[*] to recover all elements of the gradient tensor with the low frequency noise suppressed. Note, too, that because the rock amplitude α_r is small the coefficient of each harmonic term (i.e., the scale factor) is also small. This motivates

- As large a rock amplitude as possible, consistent with minimizing g-induced gradiometer errors

- Retention of as many sideband terms as possible in the demodulation process.

---

[*]As with the tumbling mechanization, ω_p and ω_r must not be harmonically related.

D.5 STEP INDEXING MECHANIZATION

It has already been observed that one disadvantage of the carousel mechanization is the effective rate limitation imposed by the associated centrifugal gradient field. A suppression technique is to alternately rotate and stop the gradiometer. During the rotation, while the instrument is slewed through a portion of a revolution, it's output is disregarded. Once the slew motion is completed, the gradiometer remains at rest until the transients resulting from the slew have settled. The instrument output is then sampled, after which another slew cycle begins. This mode of operation is illustrated in Fig. D.5-1 for the case of 45 degree slew steps and equal length dwell periods. In the figure the last portion of the dwell cycle is used for sampling.
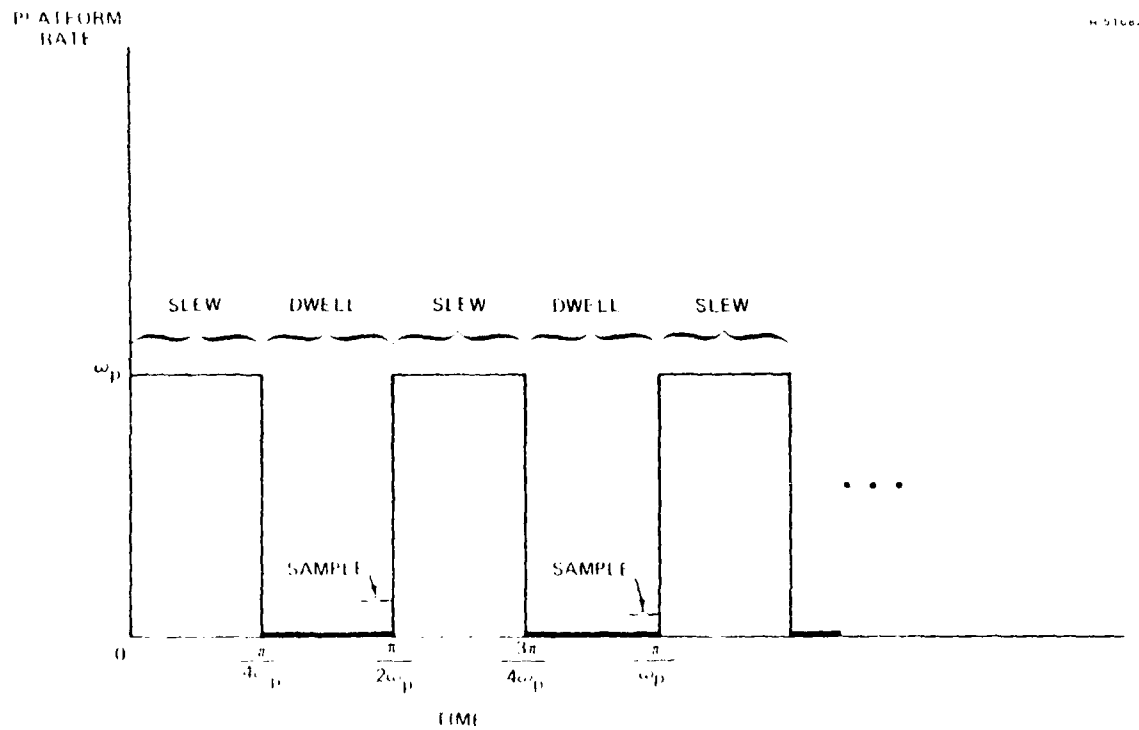

Figure D.5-1   Gradiometer Platform Motion in Step Indexing Mechanization

162

Because the sampling occurs only when the gradiometer is motionless, no biases are introduced to the gradiometer in the course of the step indexing motion. Similarly, there is no accuracy requirement for w_p. (However, the sampling period must be maintained and known accurately.)

The upper limitation on the effective carousel rate of this mechanization is dictated by the settling time required for a given slew speed. Preliminary tests have been made by Bell which indicate good gradiometer performance with 45-deg slew steps, a slew rate of 11 deg/s, and a dwell time of 5 minutes. During the dwell period approximately 15 seconds is required for transients to settle; the remaining 4-3/4 minutes are used for sampling. The effective carousel rate of this motion is approximately 1.5 cycles per hour. Further Bell tests indicate that, during the dwell interval, transient effects seem to pass after about 15 seconds. If another 15 seconds were allowed for sampling, an equivalent carousel frequency of 0.25 cycles per minute is obtained. Because of these promising indications it is likely that the first implementations of carousel motion for gradiometers will be in the step indexing mode.

REFERENCES

1. "GGI Reaction Time, Output Stability, and Error Spectrum," Bell Aerospace Textron, Report No. 6441-928013, September 1978.

2. "Vibration Flight Test," General Dynamics, Report 599FW0028 (F29601-71-C-0064), September 1971

3. "Gravity Gradiometer Instrument (GGI) and the Gravity Gradiometer System (GGS) Definition Studies Program GGI Analyses and Studies Report," Bell Aerospace Textron, Report No. 6441-927014, May 1979.

4. "Bell GGI Test Procedure No. TP1, Reaction Time, Output Stabilities, and Output Signal Error Spectrum," Bell Aerospace Textron, Report No. 6441-928001, Issue B, October 1977.

5. "Bell GGI Test Procedure No. TP2, Vibration Sensitivity," Bell Aerospace Textron, Report No. 6441-928002, Issue D, February 1978.

6. "Bell GGI Test Procedure No. TP3, Scale Factor and Linearity Response to Step Input," Bell Aerospace Textron, Report No. 6441-928003, Issue C, May 1978.

7. "Bell GGI Test Procedure No. TP4, Bias, Output Repeatability Following Application and Removal of Acceleration, Static Acceleration and Acceleration Squared Sensitivity," Bell Aerospace Textron, Report No. 6441-928004, Issue B, October 1977.

8. "Bell GGI Test Procedure No. TP7, Angular Vibration Sensitivity," Bell Aerospace Textron, Report No. 6441-928008, Issue B, February 1978.

9. "Bell GGI Test Procedure No. TP8, Linear Vibration Sensitivity of the GGI Operating in Non-Orthogonal Shake Fixture," Bell Aerospace Textron, Report No. 6441-928019, February 1979.

10. "Data Design Package, Special Test Equipment, GGI Demonstration Tests, Data Acquisition, Processing, and Recording System," Bell Aerospace Textron, Report No. 6441-927001, Issue A, March 1977.

REFERENCES (Continued)

11. "Moving Base Gravity Gradiometer Review," Bell Aerospace
    Textron, Air Force Academy Report No. 6441-927018, Feb-
    ruary 20-22, 1979.

12. "Bell GGI Test Procedure No. TP5, Temperature Sensitivity,"
    Bell Aerospace Textron, Report No. 6441-928005, Issue
    C, February 1978.

13. "Bell GGI Test Procedure No. TP6, Magnetic Sensitivity,"
    Bell Aerospace Textron, Report No. 6441-928006, Issue
    B, October 1977.

14. Kaiser, J.F., "Nonrecursive Digital Filter Design Using
    the I_o-sinh Window Function," IEEE Int. Symp. on Circuits
    and Syst., April 22-25, 1974, pp. 123-126.

15. Jones, R.H., "Multivariate Maximum Entropy Spectral
    Analysis," Applied Time Series Analysis symposium,
    Tulsa, Oklahoma, May 14-15, 1976.

16. Jones, R.H., "Multivariate Autoregression Estimation
    Using Residuals," Applied Time Series Analysis, D.F.
    Findley (Editor), Academic Press, New York, 1978, pp.
    139-162.

17. Nuttall, A.H., "Spectral Analysis of a Univariate Process
    with Bad Data Points, Via Maximum Entropy, and Linear
    Predictive Techniques," Naval Underwater Systems Center,
    New London Laboratory, NUSC Technical Report 5305, 26
    March 1976.

18. Akaike, H., "A New Look at the Statistical Model Iden-
    tification," IEEE Trans. Automat. Contr., Vol. AC-19,
    No. 6, December 1974, pp. 716-723.

19. Akaike, H., "Canonical Correlation Analysis of Time
    Series and the Use of an Information Criterion," System
    Identification: Advances and Case Studies, R.K. Mehra
    and D.G. Lainiotis (Editors), Academic Press, New York,
    1976, pp. 27-96.

20. Akaike, H., "A Bayesian Extension of the Minimum AIC
    Procedure of Autoregressive Model Fitting," Biometrica,
    Vol. 66, No. 2, 1979, pp. 237-242.

REFERENCES (Continued)

21. Trageser, M.B., "Floated Gravity Gradiometer Platform Jitter Filter," Charles Stark Draper Laboratory, Report R-1242, March 1979, pp. 4-7.

22. Harlan, R.B., "Gravity Gradiometer Instrument Environmental Sensitivities and Error-Source Analysis," Charles Stark Draper Laboratory, Report R-1221, November 1978, pp. 19-21.

23. Heller, W.G., "Gradiometer-Aided Inertial Navigation, The Analytic Sciences Corporation, Report TR-312-5, Auguest 1976.

24. Heller, W.G., "Error Models for Prototype Moving-Base Gravity Gradiometers," The Analytic Sciences Corporation, Report TR-823-1, April 1977, pp. A-1 to C-4.

25. Goldstein, J.D., "Analysis and Simulation of Multisensor Gravity Surveys and Associated ICBM Impact Errors," The Analytic Sciences Corporation, Report No. TR-868-3 (In Preparation).

26. Metzger, E.H., "Overview Rotating Accelerometer Gradiometer for Correcting Inertial Navigation Systems for the Deflection of the Vertical," Bell Aerospace Textron, Report 9500-920314, January 1974.

27. Metzger, E.H. and Affleck, C.A., "GGI Angular Vibration Sensitivity," Bell Aerospace Textron, Report No. 6441-928021, March 1979.

28. Heller, W.G. and Jordan, S.K., "Attenuated White Noise Statistical Gravity Model," J. Geophys. Research, Vol. 84, No. B9, August 1979, pp. 4680-4688.

29. Papoulis, A., Probability, Random Variables and Stochasitic Processes, McGraw Hill, New York, 1965.

30. Huddle, J.R., "Navigation to Surveying Accuracy with an Inertial System," Proc. of the Bicentennial National Aerospace Symposium (ION), Warminster, PA, April 1976.

31. Helstrom, C.W., Statistical Theory of Signal Detection, Pergamon Press, New York, 1968.

REFERENCES (Continued)

32.   Heller, W.G., K.S. Tait, and S.W. Thomas, "GEOFAST - A
        Fast Gravimetric Estimation Algorithm," The Analytic
        Sciences Corporation, Report No. TR-1007-1-1, August
        1977.

33.   Tait, K.S., "A Fast Estimation Algorithm for Two-Dimen-
        sional Gravity Data (GEOFAST)," The Analytic Sciences
        Corporation, Report No. TR-868-1-1 (In Preparation).